Explosion mechanism and neutrino reactions in the neutrino driven core-collapse supernovae

ニュートリノ駆動超新星爆発における爆発メカニズムとニュートリノ反応

October, 2022

Kenichi SUGIURA
杉浦　健一

Explosion mechanism and neutrino reactions in the neutrino driven core-collapse supernovae

ニュートリノ駆動超新星爆発における爆発メカニズムとニュートリノ反応

October, 2022

Waseda University Graduate School of Advanced Science and Engineering

Department of Pure and Applied Physics, Research on Theoretical Astrophysics

Kenichi SUGIURA
杉浦　健一

Contents

Chapter 1

Introduction

Core-collapse supernovae (CCSNe) are explosions in the final stage of massive star evolutions. Since their peak luminosities reach as much as that of galaxy consisting of more than 10^{10} stars (absolute magnitude $M \sim -19$), many CCSNe have long been observed, and its physical mechanism also has been studied for a long time. Comprehension of the CCSNe mechanism is important not only for its own sake but also for understanding the formation of neutron stars or black holes as well as the synthesis of heavy elements. Although a remarkable progress has been made over the years, the mechanism has not yet been fully understood.

The main cause of difficulties comes from most of the explosion energy of CCSN is released in the form of neutrinos which interacts with matters only thorough weak interactions. In fact, there was observation of supernova neutrino only from the supernova event SN1987A in the Kamiokande-II Hirata et al. (1987), IMB Bionta et al. (1987) and BAKSAN Alexeyev et al. (1988). For example in Kamiokande-II, 11 neutrinos were detected during $\sim 10\,\mathrm{s}$. However, multi-messenger astronomy has been remarkably advanced in recent years, and the development of neutrino detectors are also progressing. If a Galactic CCSN occur in the near future, we will more than 10^5 neutrinos from the CCSN over a minute at facilities that are currently or will be soon operational such as Super-Kamiokande (Abe et al., 2016; Suwa et al., 2019) and Hyper-Kamiokande (Abe et al., 2018) , IceCube (Abbasi et al., 2011), NOνa (Acero et al., 2020), DUNE (Abi et al., 2020) and JUNO (An et al., 2016) (for other detectors, see Scholberg (2012)).

Since the neutrino interaction is weak, SN neutrino directly comes from the central hot and dense region where we cannot observe by any frequency of electromagnetic waves. Hence we can "see" the interior of the CCSN by the neutrino observation. Understanding explosion mechanism of CCSNe and its neutrino signals are important not only for astronomical interest but for understanding the particle physics and nuclear physics under extreme condition of high temperature and density because the thermal evolution of CCSN is controlled by weakly interacting particles and the core structure is strongly affected by the equation of state (EoS) of the nuclear matter. Hence, CCSN is a unique laboratory of natural science.

In this thesis, I tackle to reveal the multidimensional effects which leads the successful CCSN explosion and the neutrino signature form the CCSN especially by improving the neutrino weak reaction rates which are indispensable to treat the neutrino transport. This chapter is organized as follows. First, I introduce briefly the evolution scenario of neutrino driven CCSN and subsequent formation of proto-neutron stars (PNS). Multidimensional effects which can be lead the successful explosion are summarized in the next section. Understanding neutrino interactions in hot dense matter is indispensable not only to the

investigation of the explosion mechanism of CCSNe but also to the quantitative prediction of neutrino signals from newly born PNS. I briefly summarize the neutrino interaction in the final section in this chapter.

1.1 Evolution form core-collapse to formation of neutron star

Chemical evolution and fate of massive stars are different depending on its mass, $M_{\rm ZAMS}$. There are two types of progenitors that are supposed to produce CCSNe; they are called "iron core collapse supernova (FeCCSN)" and "electron capture supernova (ECSN)". Majority of CCSNe are FeCCSN and their progenitor masses are $10M_\odot \lesssim M_{\rm ZAMS} \lesssim 100M_\odot$. These progenitors have the iron core and temperature of the core is increased due to Si-shell burning. When the temperature T_c exceeds $10^{10}\,$K, photo-dissociations of iron nuclei

$$^{56}{\rm Fe} \rightarrow 13\,^4{\rm He} + 4{\rm n}, \tag{1.1}$$

$$^4{\rm He} \rightarrow 2{\rm p} + 2{\rm n}, \tag{1.2}$$

are triggered to minimize the free energy. These endothermic reactions makes the core unstable and induce the dynamical collapse of the core.

ECSNe occupy almost 5% of CCSNe (Doherty et al. (2017)) of which the progenitor mass is $8M_\odot \lesssim M_{\rm ZAMS} \lesssim 10M_\odot$. For these lighter progenitors, oxygen-neon-magnesium (ONeMg) core is produced and its mass increases due to C-burning. If the central density reaches the threshold for electron capture (EC) on ^{24}Mg ($\rho_c = 10^{9.88}\,{\rm g/cm^3}$), then the core begins to contract due to the decreasing of the electron pressure through the EC. This leads the O- and Ne-deflagration and results in core collapse. The resultant SN explosion its explosion energy is supposed to be weaker with the explosion energy $L_\nu \sim 10^{50}\,$erg than FeCCSN $\sim 10^{51}\,$erg (Kitaura et al. (2006)). For example, the Crab pulsar (or SN1054) is considered as one of electron capture supernova.

In this section, I explain the evolutions of FeCCSN, which is main focus of this thesis, from the core-collapse to the formation of neutron stars. Unless otherwise noted, CCSN means the FeCCSN hereafter in this thesis.

Core-collapse and neutrino trapping

Collapse of the Fe core is the beginning of the CCSN. The central density is rapidly rapidly rose by the collapse and the collapse suddenly stops when the density of the collapsing core becomes close to the saturation density ($\rho_s \sim 2.3 \times 10^{14}\,{\rm gcm^{-3}}$) because it is stiffen by the nuclear force. This is the core of the PNS.

Due to the compression of matter, electron becomes strongly degenerate and becomes the high Fermi energy. Then the electron capture reaction, $e^- + p \rightarrow n + \nu_e$, occur easily and the number of neutron increases, called "neutronization". A copious number of electron-type neutrino are also emitted by electron capture reaction. Typical cross section of weak interaction is estimated from the reaction rate of neutrino capture as

$$\sigma_w \sim G_F^2 \epsilon_\nu^2 \sim 10^{-42}\,{\rm cm^2} \left(\frac{\epsilon_\nu}{10\,{\rm MeV}}\right)^2, \tag{1.3}$$

with the Fermi coupling constant $G_F = 1.164364 \times 10^{-11}{\rm MeV}^{-2}$ and the neutrino energy ϵ_ν. The mean free path of neutrino in the collapsed matter is roughly estimated from the

above cross section as

$$l_{\rm mfp} \sim \frac{1}{n_n \sigma_w} \sim 10^5\,{\rm cm} \left(\frac{\rho}{10^{14}\,{\rm g/cm^3}}\right)^{-1} \left(\frac{\sigma_w}{10^{-42}\,{\rm cm^2}}\right)^{-1}, \tag{1.4}$$

where n_n is the number density of neutron. Since $l_{\rm mfp}$ is much smaller than the typical size of PMS core ($\sim 10^6$ cm), electron-type neutrino is trapped in the Fe core, called "neutrino trapping". So, the PNS accumulate a large amount of neutrino from the moment it is born. Also due to the neutrino trapping, chemical equilibrium of the electron capture (called beta equilibrium) is realized and the chemical potentials satisfies

$$\mu_e + \mu_p = \mu_n + \mu_{\nu_e}. \tag{1.5}$$

Sudden stop of core collapse is called core bounce. Since the accreting matter has supersonic velocity whereas the PNS core contracts in subsonic velocity, shock wave is produced at the surface of the PNS core.

Shock stagnation and neutrino heating mechanism

After the core bounce the shock propagate outward by the thermal pressure of the shocked matter. If the shock successfully break through the collapsing Fe outer core, the shock easily propagate the outer envelope of the progenitor and become successful CCSN. It is well known, however, that the shock is stagnated inside the core because of energy losses via photodissociations of the nuclei. Simultaneously, when the shock front reaches the neutrino sphere, where the neutrino moves freely outside of this radius, the trapped ν_e released suddenly, resulted in the strong emission of neutrino, called "neutronization burst". The thermal energy of the shocked matter is also subtracted by the neutrino emission in the neutronization burst, hence stagnetion of the shock is reinforced.

Hence there must be some mechanisms to push the stalled shock wave outward again. Energy source of CCSNe is gravitational energy of the contracting core and it is roughly estimated as

$$\begin{aligned}
\Delta W &\sim \left(-G\frac{M_{\rm core}^2}{R_i}\right) - \left(-G\frac{M_{\rm core}^2}{R_f}\right) \\
&\sim \left(-10^{51}{\rm erg}\left(\frac{R_i}{10^8{\rm cm}}\right)^{-1}\right) - \left(-10^{53}{\rm erg}\left(\frac{R_f}{10^6{\rm cm}}\right)^{-1}\right) \\
&\sim 10^{53}{\rm erg},
\end{aligned} \tag{1.6}$$

where R_i and R_f are the typical radius of PNS core before and after collapse, respectively and we assume $M_{\rm core} \sim 1.4 M_\odot$. The typical energy of kinetic energy of CCSNe estimated from the optical observation is roughly 10^{51} erg, it is sufficient if 1% of ΔW is converted to the kinetic energy.

The most promising scenario at present is the neutrino-heating mechanism, in which matter passing the stalled shock wave acquires energy from neutrinos emitted from PNS and the shock revival obtains as a result. This scenario is natural because 99% of gravitational energy is released by radiation of neutrino. In fact, accreting matter heated mainly via reaction between electron type neutrinos and nucleons (proton and neutron):

$$\nu_e + n \to p + e^-, \tag{1.7}$$

$$\bar{\nu}_e + p \to n + e^+. \tag{1.8}$$

Heating rate of these reactions is approximately written as

$$\begin{aligned}\left(\frac{\mathrm{d}E}{\mathrm{d}t}\right)_{\mathrm{abs}} &\sim \frac{\sigma L_\nu}{4\pi r^2} \\ &\sim \frac{1}{4\pi r^2}\left(4\pi r_\nu^2 \sigma_{\mathrm{SB}} T_\nu^4\right)\left(A\varepsilon_\nu^2\right) \\ &\sim 9k_B^2 \sigma_{\mathrm{SB}} A T_\nu^6 \left(\frac{r_\nu}{r}\right)^2, \end{aligned} \tag{1.9}$$

where we assume $\sigma \simeq A\varepsilon_\nu^2$ and $\varepsilon_\nu \sim 3k_B T_\nu$. σ_{SB} and k_B are Stefan-Boltzmann constant and Boltzmann constant, respectively. Cooling also occurs due to inverse reactions of (1.7) and (1.8) and cooling rate is written as

$$\begin{aligned}\left(\frac{\mathrm{d}E}{\mathrm{d}t}\right)_{\mathrm{em}} &= -\sigma v_{e^\pm} n_{e^\pm} \langle \varepsilon_\nu \rangle \\ &\sim 36 k_B^2 \sigma_{\mathrm{SB}} A T_m^6, \end{aligned} \tag{1.10}$$

where electron-positron dominance is assumed and also $n_e \sim a/3k_B T_m^3$ and $\langle \varepsilon_\nu \rangle \sim 3k_b T_m$. As a result, net heating rate is approximately given by

$$\begin{aligned}\left(\frac{\mathrm{d}E}{\mathrm{d}t}\right)_{\mathrm{net}} &= \left(\frac{\mathrm{d}E}{\mathrm{d}t}\right)_{\mathrm{abs}} + \left(\frac{\mathrm{d}E}{\mathrm{d}t}\right)_{\mathrm{em}} \\ &\sim \left(\frac{\mathrm{d}E}{\mathrm{d}t}\right)_{\mathrm{abs}} \left\{1 - \left(\frac{2r}{r_\nu}\right)^2 \left(\frac{T_m}{T_\nu}\right)\right\}. \end{aligned} \tag{1.11}$$

In general, since T_m^6 decreases more rapidly than r^2 as radius gets larger, net heating of the accreting matter becomes positive above a certain radius called gain radius. Region between gain and shock radii is called gain region and there is a possibility to explode successfully by this heating.

This "delayed explosion mechanism" was found first by Bethe and Wilson (1985) in which the stalled shock moves outward again by the neutrino heating for sufficiently long time in their spherically symmetric simulation (1D simulation). It is common agreement, however, that crude estimation in their study exaggerated the heating and 1D simulation does not reproduce the successful explosion even though including detail neutrino transport and general relativistic effects.

Figure 1.1 shows the evolution of mass element in the core of $15M_\odot$ progenitors after the core bounce Sumiyoshi et al. (2005)). The thick dashed line denotes the radius of the shock wave. As can be seen, the shock propagation stops at the post bounce time $t_{\mathrm{pb}} \sim 100\,\mathrm{ms}$ and turned to shrink.

To overcome this stagnation of the shock, many researcher try to investigate multidimensional SN explosion with numerical simulation. Recently, some successful simulation have reported (for recent review see Müller (2020)) and the non-spherical motion of matter, such as convection and a standing accretion shock instability (SASI), extend the timescale of matter fall to gain the neutrino heating. There are also alternative multi-D effects supporting the successful explosionn such as acoustic mechanism, LESA and so on. I introduce these multi-D effects in section 1.2.

1.1.1 PNS cooling

Let us focus on the evolution of remaining compact object after the successful CCSN, i.e. PNS because most of the gravitational binding energy of PNS is released in the form of

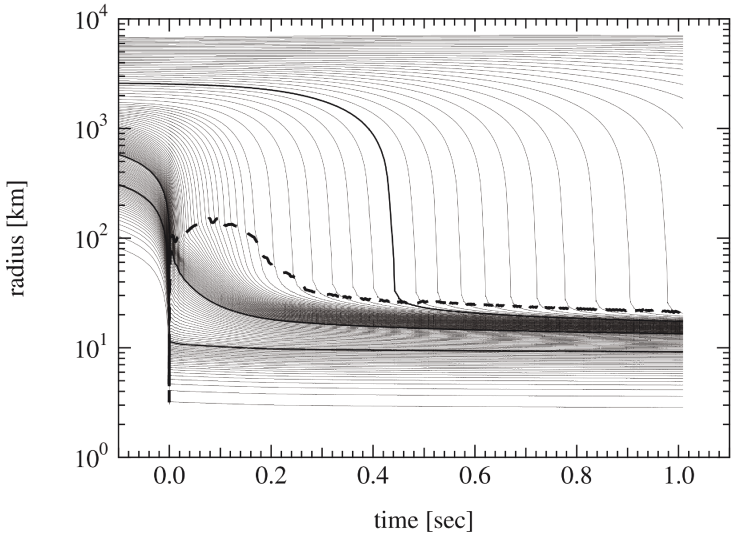

Figure 1.1: The evolution of mass elements in the core of $15M_\odot$ progenitors after the core bounce. The thick dashed line denotes the radius of the shock wave.

neutrinos, with roughly a half of them being emitted in the explosion phase of CCSN and the remaining half being radiated in the newly born PNS.

PNS cooling is roughly divided in three phases, I will explain these phases one by one, using the standard PNS cooling simulation. Figure 1.2 shows a 1D PNS cooling calculation under spherical symmetry The simulation was done as follows: core-collapse of a 15 $M_\odot$ progenitor Woosley and Weaver (1995) was first computed with the general relativistic neutrino-radiation hydrodynamics code Sumiyoshi et al. (2005) until $t = 0.3\,\mathrm{s}$ after core bounce when the shock wave is stalled. Knowing that this model does not explode in 1D (see Figure 1.1) but expecting that it will explode in multi-dimensions, I extracted the region inside the shock wave (up to mass coordinate of $\sim 1.47M_\odot$) from the result of the first simulation and use it as an initial condition of the second simulation of PNS cooling. In this second simulation, the quasi-static evolution of the PNS is computed by solving the Tolman-Oppenheimer-Volkov equation together with the neutrino transfer equation, the latter of which was solved with the multi-group flux limited diffusion scheme for neutrino transfer Suzuki (1994); the Shen EoS Shen et al. (2011) was adopted.

Accretion phase of the shocked matter

Just after the successful explosion, PNS core formed during the core-collapse is surrounded by the shocked matter of which radius is $\sim 100\,\mathrm{km}$. During the first a few s, the shocked matter accrete onto the PNS core as the pressure of the matter decreases due to the energy loss of neutrino emission. This phase is called accretion phase or mantle contraction phase. The radius of the PNS becomes a few tens km after the accretion phase which is comparable with that of the cold neutron star.

Accretion phase of the PNS cooling can be seen in the evolution from the red line to the yellow line in Figure 1.2. As can be seen from the upper left panel that the radius of the mass shell $m \gtrsim 0.7M_\odot$ shrinks rapidly and density increase. Although these compression of matter makes the temperature of mass shell higher, the temperature increase is gradually due to the energy extraction due to the neutrino emission.

Deleptonization phase

After the accretion phase, the PNS is settled to a quasi-hydrostatic configuration and its subsequent evolution is driven by diffusive neutrino emissions Burrows and Lattimer (1986); Pons et al. (1999); Fischer et al. (2010); Hüdepohl et al. (2010); Roberts (2012); Nakazato et al. (2013); Roberts and Reddy (2017b). This neutrino flux transfer the thermal energy from the off-center region to the central of the PNS as well as the lepton number (see the evolution from the yellow line to the blue line in Figure 1.2).

This phase is called the deleptonization phase or the cooling phase because the lepton number in the PNS is carried away by the neutrino flux due to the positive flux of the electron neutrino throughout the PNS. Deleptonization cooling phase occurs on the Kelvin-Helmholtz (KH) timescale given as

$$\tau_{\rm KH} = \frac{E_b}{4\pi R_\nu^2 F_\nu} \sim O(10)\,{\rm s}, \tag{1.12}$$

where E_b, R_ν and F_ν are the binding energy of PNS, the radius of neutrino sphere and the neutrino energy flux, respectively (Nakazato and Suzuki (2020)). μ_{ν_e}/T decrease and eventually the entire PNS the state with $\mu_{\nu_e}/T \sim 0$.

Thermal cooling phase

Once $\mu_{\nu_e}/T \sim 0$ throughout the star, the PNS slowly cooling as teh energy leaks from the entire star through the thermal neutrino emission:

$$e^- + e^+ \to \nu + \bar{\nu}, \tag{1.13}$$

$$N + N \to N + N + \nu + \bar{\nu}, \tag{1.14}$$

where N denote the nucleon (i.e. neutron or proton). This phase is shown as the evolution after the purple line and the PNS gradually decrease its temperature to become a cold NS.

1.2 Multidimensional effects

It is now a consensus of the supernova society that multidimensional effects are crucial for the success of the delayed neutrino-driven explosion scenario except for the low-mass end of massive stars (Kitaura et al. (2006)).

Multidimensional effects are interesting in not only theoretical but also observational point of view. Recently, LIGO (Aasi et al. (2015)) and VIRGO (Acernese et al. (2015)) group observed gravitational waves (GWs) from binary BHs and NSs (see e.g. Abbott et al. (2016, 2017); The LIGO Scientific Collaboration et al. (2020)) and gravitational astronomy is now evolving. Recent numerical simulations have revealed that there are violent non-spherical motions of matter and vibration of core of proto-neutron star (PNS) in the interior of CCSNe, and hence the GWs from CCSNe are the most promising candidates of the next-generation GW observations such as KAGRA (Akutsu et al. (2021)). CCSNe are now one of the hottest topic in the multi-messenger astronomy.

In this section, I summarize the multidimensional effects recently investigated as supports of neutrino-driven explosion.

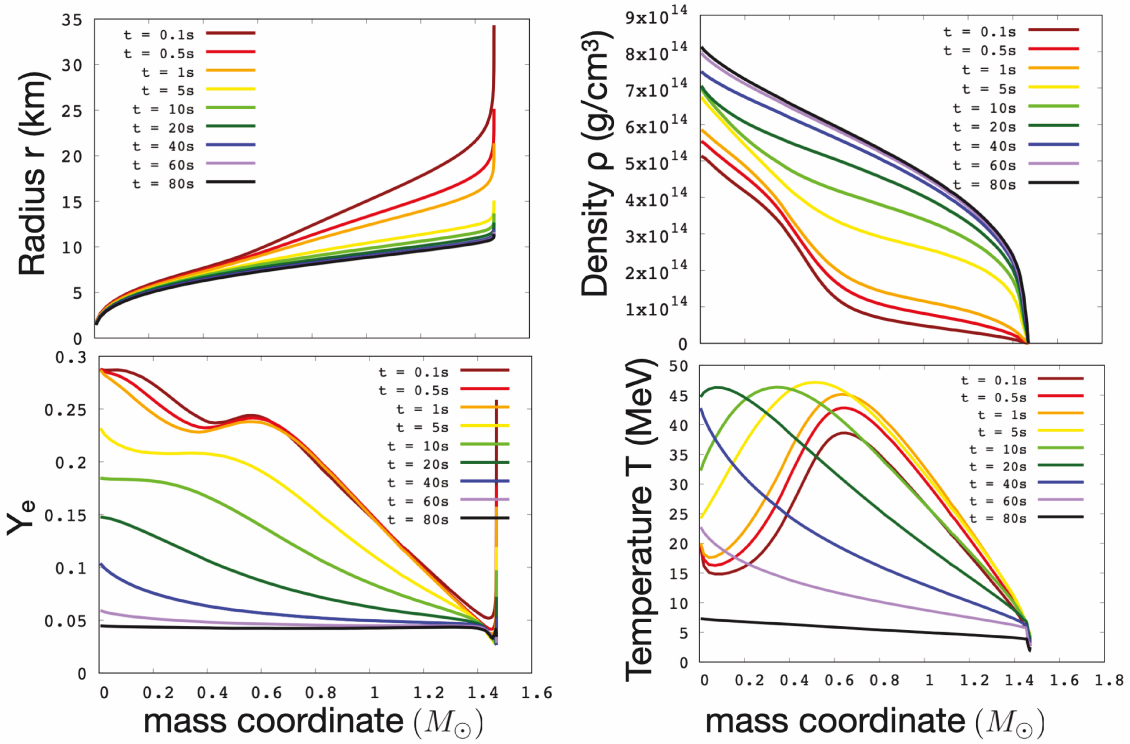

Figure 1.2: 1D simulation of the PNS cooling. This simulation start with $t_{\rm pb} = 0.3\,{\rm s}$. Upper left panel shows the radius of mass shells. Density, electron fraction Y_e and temperature are shown in upper right, bottom left and bottom right panels, respectively.

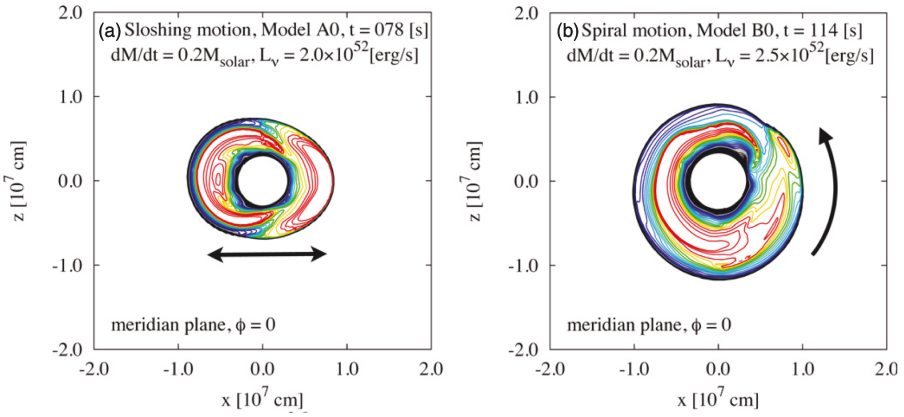

Figure 1.3: Snapshots of the entropy contour map in the meridian plane for sloshing mode (left panel) and spiral mode (right panel). The entropy S is in units of Boltzmann ' s constant k_b per nucleon. The contour levels are equally spaced in the range of $4 \leq S \leq 20$ with the increment of $\Delta S = 0.4$. The contour lines of higher values are drawn in reddish colors, and those of lower ones are done in bluish colors. The inner- and outermost contour lines agree with the surfaces of the proto-neutron star and the shock wave, respectively. The arrows mean the global oscillation of the shock wave in the indicated direction. Iwakami et al. (2014)

1.2.1 Standing Accretion Shock Instability

It is believed that CCSNe are not spherically symmetric in general, being subject to hydrodynamical instabilities (see Burrows (2013); Janka et al. (2016) for recent reviews) such as convection (Bethe (1990); Herant et al. (1994)) and standing accretion shock instability (SASI) (Blondin et al. (2003); Iwakami et al. (2014)).

SASI in CCSNe was first discovered in axisymmetric 2D numerical simulations (Blondin et al. (2003)). They found that deformations of the shock front with low l modes of spherical harmonics grow exponentially. These instabilities induce turbulent motions and then extra pressure provided by the turbulence pushes the shock wave outward. As a result, the gain region is broadened and the neutrino heating is enhanced (Murphy et al. (2013); Couch and Ott (2015)). In fact, SASI can decrease critical luminosity for the shock revival in 2D simulation (Ohnishi et al. (2006)). By the critical neutrino luminosity, we mean here the minimum neutrino luminosity at which expansion of the shock continuously occurs in their simulation which will eventually lead to successful explosion.

SASI shows the roughly two types of shock deformation. One is "sloshing mode" (left panel of Figure 1.3) in which the axisymmetric sloshing motion is induced. In linear deformation phase, the sloshing mode corresponds to the $(l, m) = (1, 0)$ or $(2, 0)$ mode where l and m denote the polar and azimuth index of the spherical harmonics expansion $Y_{l,m}$. The other is called "spiral mode" (right panel of Figure 1.3) in which the non-axisymmetric deformation around the axis is induced and also rotate around the axis. This mode is found in the 3D numerical simulation of CCSN (Hanke et al. (2013); Fernández (2015)) The spiral mode corresponds to the $(l, m) = (1, 1), (1, -1)$ modes or higher l modes with $m \neq 0$.

The physical mechanism of SASI is supposed to be explained by the advective-acoustic cycle (AAC) or purely acoustic cycle (PAC). In the AAC scenario, the entropy and vorticity perturbations advect toward PNS generate a sound wave at the location of the largest velocity gradient of the stationary flow. The sound wave propagates toward the shock wave and distorts its configuration, depending on the non-radial distribution of the pres-

sure fluctuation. The deformed shock wave induces further amplification of the entropy and vorticity perturbations (Foglizzo (2009)). For the PAC scenario, the standing pressure wave propagates in the circumferential direction in the region between the spherical accretion shock wave and PNS. When the postshock pres- sure is slightly higher than unperturbed pressure, it pushes the shock wave outward. The outward displacement of the shock wave leads to an increase of postshock pressure in the inner region, while the postshock pressure immediately behind the shock wave decreases. Thus, the amplitude of the pressure fluctuation increases further Blondin and Mezzacappa (2006).

The understanding of SASI is also important for analysis of neutrino and GW signals. Since the source of neutrino radiation is the gravitational energy of the accreting matter, the radiated neutrino luminosity depends on mass accretion rate of the PNS. As a natural consequence, the fluctuations of accretion induced by SASI motion leads modulations of the neutrino luminosity. This is really detectable by IceCube and Hyper-Kamiokande for a galactic SN (Takiwaki and Kotake (2018)). Similarly, GW signals reflects the information of mass motion in the post-shock layer. Violent mass motion due to SASI-activity resulted in modulations of the mass-quadrupole moment and therefore GW radiation. It is believed that this modulation can be detected by using next generation GW detection instruments for galactic SN (Kawahara et al. (2018)).

1.2.2 Acoustic Mechanism

Multidimensional effects discussed nowadays are not only fluid instability. Acoustic mechanism are recently proposed by Burrows et al. (2006, 2007a,b). Basic scenario of this is as follows: impulsive forces from anisotropic accretion downflows excite gravity-mode (g-mode) oscillations of the PNS. And then, generated acoustic waves become steepened as they propagate because of the negative gradient of the density, deposit energies to postshock matter. Finally, the deformation of the shock front is induced in the same inisotropies. If we assume acoustic power is generated by periodic core oscillation due to hit of a nonspherical, steady accretion stream, one can estimate the acoustic power:

$$\begin{aligned}\dot{E}_{\rm ac} &\simeq \frac{\pi\rho}{2}\left(g_{\rm PNS}R_0\right)^{3/2} H_0^2 \\ &\sim 0.5\times 10^{51}{\rm erg/s}\left(\frac{\rho}{10^{11}\ {\rm g/cm^3}}\right)\left(\frac{g_{\rm PNS}}{10^{13}\ {\rm cm/s^2}}\right)^{3/2}\left(\frac{R_0}{10\ {\rm km}}\right)^{3/2}\left(\frac{H_0}{3\ {\rm km}}\right), \quad (1.15)\end{aligned}$$

where ρ, $g_{\rm PNS}$, R_0, H_0 are the average density at the surface of the PNS, the average acceleration at the PNS surface, accretion stream radius and wave height, respectively (Burrows et al. (2007b); Janka (2012) and Burrows et al. (2006)). Of course, there is a large uncertainty in the value of H_0, the depositing energy is compatible with the explosion energy of CCSNe, assuming that the acoustic power injected for a long time $\gtrsim$ 1s.

One of the advantages of acoustic mechanism is that acoustic wave does not go through the shock because of the supersonic accretion in the outer shock region and deposits all energies inside the shock. Hence, the acoustic mechanism acts as high efficient transducer from gravitational energy to energy of postshock matter. Unfortunately, successful explosion driven by acoustic power have not been reproduced by other numerical simulation groups (e.g., Marek and Janka (2009)), however, acoustic mechanism is still hot issue in CCSNe mechanism and have been tested, for example, in phenomenological way (Yoshida et al. (2007); Harada et al. (2017)). Note that this mechanism is intrinsically multidimensional since g-mode oscillation are no spherical motions.

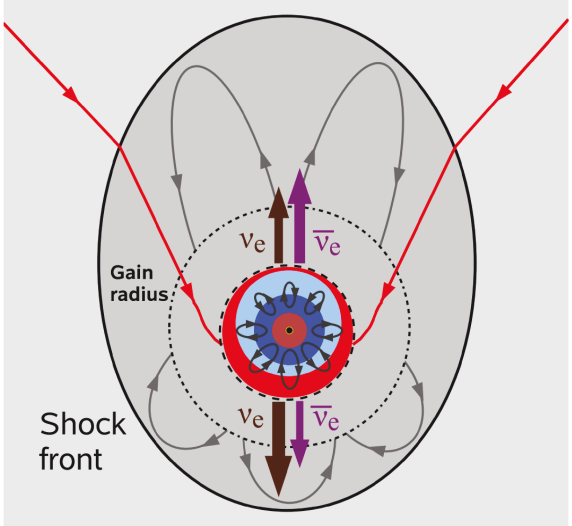

Figure 1.4: Schematic picture of LESA (Tamborra et al. (2014a)). The black line shows the deformed shock front and the red lines denote the accretion inflow to the PNS. The dashed line is the PNS surface and red and light-blue regions denote the lepton-rich and leptin-poor region, respectively. The brown and purple arrows means ν_e and $\bar{\nu}_e$ fluxes, respectively. $\bar{\nu}_e$ and ν_e fluxes are stronger in the top and bottom hemisphere, respectively. The dotted line indicates the gain radius.

1.2.3 Lepton-number Self-sustained Asymmetry

Recent years, it is proposed that new types of neutrino-hydrodynamical instability called Lepton-number Emission Self-sustained Asymmetry (LESA) (Tamborra et al. (2014a,b)). In this instability, ν_e and $\bar{\nu}_e$ fluxes show a dipole pattern in the opposite direction and this non-spherical configuration was sustained for a long time. Simultaneously, neutrino luminosity also shows dipole pattern since mean energy of $\bar{\nu}_e$ is higher than that of ν_e. As a result, neutrino heating is stronger in side at which $\bar{\nu}_e$ flux is stronger. Tamborra et al. (2014a) shows numerically that these stronger neutrino heating enhances convective overturn and push the shock outward. It was argued that such stable configurations were the outcomes of the interplay between the deformation of the shock wave and the anisotropic emissions of neutrinos from the PNS surface.

Self-sustainability of LESA is supposed to be explained the following feedback loop. Figure 1.4 shows the schematic picture of interplay between deformation of shock and anisotropic neutrino emission. The black line shows the position of the shock which is deformed in the direction to upper side of the figure. The two red curves show the anisotropic accretion flow towards the PNS which is denoted by the dashed circular line. The radial accretion flow is deflected by the deformed shock because the tangential velocity is conserved whereas the perpendicular velocity is reduced by the shock jump condition (Rankin-Hugoniot condition) (see Eqs. (2.10) - (2.12)). The accretion flow becomes strong on the bottom hemisphere of the PNS and much more fresh lepton number is supplied in this hemisphere. As a results, the lepton rich matter in the bottom hemisphere produce the lepton rich neutrino flow which means electron neutrino is more abundant than the electron anti-neutrino. This makes the asymmetric neutrino emission as shown in Figure 1.4 (brown and purple arrows). Simultaneously, strong accretion in bottom hemisphere of the PNS instigate the turbulence and gravity wave inside the PNS in this side. This resulted in the strong dredging up electron from the central, lepton rich dense core (red region in Figure 1.4) and make more the strong lepton number flux in downward direction.

Since the neutrino heating is stronger in the side in which $\bar{\nu}_e$ flux is stronger as I mentioned, neutrino heating occur strongly in the upper hemisphere and shock front is pushed also in the same side. This deformation is the same side as initially considered, so this loop is expected to sustained for a long time.

Tamborra et al. (2014a) also reported that a shock deformation is related with an anisotropy in the number flux difference $F^n_{\nu_e} - F^n_{\bar{\nu}_e}$ of the electron-type neutrinos. On the other hand, Dolence et al. (2015) later reported that they found a dipolar asymmetry not in the difference but in the sum of the two fluxes $F_{\nu_e} + F_{\bar{\nu}_e}$ (and also the sum of number fluxes) is strongly correlated with the deformation of the shock front. In addition to this apparent discrepancy, there have been doubts that LESA is a numerical artifact because Ray-by-Ray+ code using in their neutrino transport calculation exaggerates directional dependence of the fluctuations. Recent studies by other groups suggest that LESA is really physical phenomena, but they observed various different characteristics with Tamborra et al. (2014a) such as much smaller deformation (Glas et al. (2018)), different pattern of deformation of the lepton number flux (Takiwaki and Kotake (2018)) and sustaining PNS convection which generate the lepton number flux deformation (not correlated with the shock deformation) (Powell and Müller (2019)). As stated above, there is no consensus about characteristics and physical nature of LESA and the researches are currently in progress.

1.3 Neutrino interaction in hot dense matter

Neutrino interaction with the supernova matter and its reaction rates play a fundamental role for understanding the CCSN physics. The major processes are the charged current absorption of ν_e and $\bar{\nu}_e$ absorption on nucleons, neutral-current scattering off the nucleons, neutrino-electron/positron scattering, neutrino-neutrino scattering and neutrino-antineutrino absorption. Reaction rate of the pure leptonic reaction such neutrino-electron scattering can be calculated in the framework of Weinberg-Salam theory in perturbative way.

However, neutrino nucleon interaction includes many uncertainty because of our ignorance of exact form of strong field. So numerical simulation of these neutrino nucleon interaction often employ the analytic expressions which are based on very crude approximation. For the precise prediction of the neutrino signals from CCSN and subsequent PNS cooling, we must improve these reactions carefully. In the next section I summarize the several corrections which have been added to the original analytic expression.

Recently, the muon existence in the early phase of CCSN . This open the new interaction channel through the weak interaction which is one of the main topic in chapter 3, so I briefly review.

1.3.1 Neutrino-nucleon interaction

The analytical expression of neutrino-nucleon reaction is often based on Bruenn (1985) in which the only dominant order in the matrix element squared of the invariant scattering amplitude and the momentum transfer of the lepton to the nucleon is neglected i.e. elastic limit (hereafter I call this limit as Bruenn limit). Several corrections have to be included in this simple rate.

Recoil of the nucleon

The elastic approximation have been justified because the mean energy of neutrino is at most the several tens MeV which is much smaller than the rest mass of nucleon. The recoil correction is important especially for heavy neutrinos (i.e. μ and τ type (anti-)neutrino) because the neutrino scattering on neutrino is the dominant opacity for them. The energy transfer from neutrino to nucleon modifies the neutrino spectra and if we take into account recoil for the scattering of neutrino, the difference of the average energy becomes smaller (Raffelt (2001)). These spectral modification is important also for comparison with theoretical prediction of neutrino signal of CCSN and future SN neutrino observation.

Weak magnetism of nucleon

Weak magnetism is a higher oder correction for the vector current of nucleon current which is originated from the anomalous magnetic moment in the electro magnetic interaction. This correction is proportional to q/M_N where the q is the magnitude of the momentum transfer to the nucleon and M_N is the mass of nucleon. Horowitz (2002) studied the correction for the Bruenn limit in the rest frame of the nucleon. They revealed that this correction reduces the opacity for neutrino and increases for anti-neutrino for both charged-current and neutral current reaction. The luminosity of ν_e enhances due to the opacity reduction and then enhances the neutrino heating in the gain region whereas the opposite happens for anti-neutrino. In fact, the magnitude of correction is higher for the neutrino than the anti-neutrino and it imply that the net neutrino heating can be enhanced the explodability.

Although this Horowitz correction factors can not apply directly to the numerical simulation of CCSNe which is usually done in the laboratory frame, not the rest frame, this correction is often applied crudely. In chapter 3, I show the correction of the weak magnetism correction including the full thermal distribution of nucleons.

Effect of mean field of nucleon

The dispersion relation of the nucleon is modified in hot dense matter encountered in CCSN. The charged-current reaction are sensitive the modifications because the they shift the thresholds in the reactions. For example in the electron capture on neutrino, $\nu_e + n \to e^- + p$, the capture is often suppressed due to the Fermi blocking of the highly degenerated electron which have large Fermi energy in dense region. Since the difference of the effective potential between neutron and proton satisfies $U_n - U_p > 0$, the outgoing electron gains the energy by this difference and the Fermi blocking can overcome easily. This results in the enhancement of the opacity of neutrino.

In this work, we take them into account at the mean-field level. Although it is well known that the vertex corrections need to be considered simultaneously at the level of the random phase approximation Burrows and Sawyer (1998); Reddy et al. (1999); Yamada and Toki (1999); Oertel et al. (2020), we will defer it to a later paper as it is a major undertaking and we think it is still meaningful to make comparisons with other works that also neglected the corrections Guo et al. (2020).

1.3.2 Muon-related neutrino interaction

In the past, only electrons and positrons were incorporated as the charged-lepton constituents in most of the quantitative simulations of both CCSN and PNS cooling. That

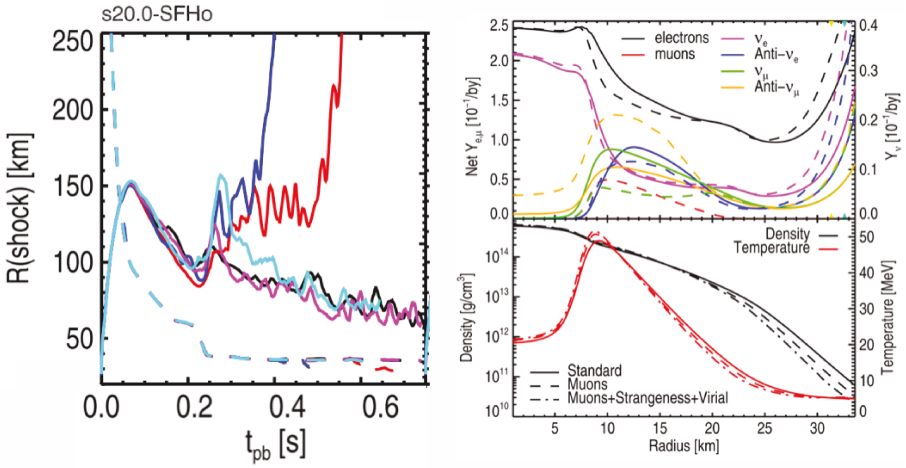

Figure 1.5: (Left panel) Angle-averaged shock radii (solid line) and mass-infall rates (at 400 km, dashed line) versus post bounce time in the axisymmetric CCSN simulation. (Right top panel) Radial profiles at 0.4 s after bounce of the net numbers of charged leptons (left-hand scale) and neutrinos (right-hand scale). (Right bottom panel) Radial profiles of density (black line) and temperature (red line) Bollig et al. (2017). The progenitor mass is $20M_{\odot}$ and SFHo EoS (Hempel et al. (2012)) is applied.

is because the muon and tauon have rest masses much larger than the typical temperature in the CCSN interior and their existence is supposed to be suppressed in the early explosion phase. Recently, the possible effects of the tiny population of muons on the supernova explosion as well as on the PNS cooling in the very early phase were investigated in supernova simulations under axisymmetry Bollig et al. (2017); Fischer et al. (2020).

They showed that muons start to emerge soon after core bounce through the thermal pair production of mu-type neutrinos and anti-neutrinos and their subsequent conversion into muons by the following charged-current (CC) reactions, $\nu_{\mu}+n \rightarrow \mu^{-}+p$ and $\bar{\nu}_{\mu}+p \rightarrow \mu^{+}+n$ (see right panel of Figure 1.5).

Figure 1.5 show the simulation results of 2D-simulation of CCSN which progenitor mass is is $20M_{\odot}$ and SFHo EoS (Hempel et al. (2012)) is applied. Left panel shows the angle-averaged shock radii (solid line) and mass-infall rates (at 400 km, dashed line) as functions of post bounce time. The black line shows simulation neglecting the muon and the red line shows that with muon. Radial profiles at 0.4 s after bounce of the net numbers of charged leptons (left-hand scale) and neutrinos (right-hand scale) are shown in right top panel. Right bottom panel denotes radial profiles of density (black line) and temperature (red line). As can be seen in the right top panel, muon is produced at the temperature becomes higher due to the accumulation of the shocked matter.

They also demonstrated that the formation of muon softens the EoS through the conversion of thermal energy to the rest mass energy, leading to a bit more rapid contraction of PNS and higher neutrino luminosities and hence the heating of matter behind the stalled shock wave; as a result, the muon formation facilitates the neutrino-driven explosion in their model Bollig et al. (2017). The difference of the shock between with and without muon are exhibit by the comparison between the red and blue lines in Figure 1.5. In fact the former success the explosion where as the latter fails.

Moreover, it was argued in Horowitz and Li (1998) that faster escapes from PNS of $\bar{\nu}_{\mu}$ than ν_{μ} because of its smaller cross section for the neutral-current scattering with nucleon due to the weak magnetism correction Horowitz (2002) will pile up the muon lepton number later in the PNS, which is essentially vanishing at the beginning. As a matter of

fact, the non-negligible population of muon in the neutron star has been known from the studies of nuclear EoS over the years Douchin and Haensel (2001); Shen (2002); Zhang and Li (2020). It is hence obvious that the muon existence is more important at later times in the PNS cooling, affecting the neutrino transport and, as a result, the cooling. Hence the neutrino interaction related with muon is expected to make an important role in the cooling phase of the PNS and this is main topic in chapter 3.

Chapter 2

Linear analysis of the shock dynamics

I already outlined several multidimensional effects that can be contribute to reviving the shock revival in the Introduction. It is true that normally these multidimensional instabilities become fully nonlinear and the induced motions are very complex, which are investigated mostly by simulations, but the linear stability analysis is still very useful: we can confirm that there are indeed unstable modes; the analysis of these modes and the corresponding growth rates and frequencies (if they are oscillatory) helps us unravel the mechanism of the instabilities (Guilet and Foglizzo (2012)).

The turbulence may be described as couplings of these modes. As a matter of fact, previous studies conducted such linear analysis based on the Fourier (Yamasaki and Yamada (2007)) or Laplace (Takahashi et al. (2016)) transform for the steady and spherically symmetric post-shock accretion flows, imposing the inner and outer boundary conditions at the neutrino sphere and the standing shock wave, respectively. Although these instabilities are intrinsic, i.e., they grow from an initial perturbation on their own without any further external supports, possible interactions with external perturbations are attracting much interest these days.

From the point of view of the linear analysis mentioned above, this may correspond to imposing time-dependent outer boundary condition. Using the Laplace transform in time, Takahashi et al. (2016) investigated the generation of various modes, particularly unstable ones, by the temporal fluctuations given at the outer boundary by the turbulent accreting matter. They demonstrated that some modes are induced more strongly than others. In this previous study, the inner boundary condition was left unchanged although we know that it should be also oscillatory. In fact as we mentioned, the PNS is not completely static but oscillating and wobbling owing to the exertion of impulsive forces by the matter accreting turbulently onto PNS and generates acoustic waves.

Even if the amplitudes of the acoustic waves are not so large as to produce secondary shock waves, they may still play an important role at the linear level. As a matter of fact, the inner boundary condition becomes time-dependent as already mentioned and, as a result, the linearly unstable modes are expected to be affected by their presence. This effect is what we study in this chapter in the context of linear stability analysis. We employ the inner boundary condition that varies sinusoidally in time. We investigate how the oscillation frequencies and growth rates of various unstable modes are changed by this modification of the inner boundary condition.

In this study, we take also into account perturbations of the neutrino luminosity, which should be expected if PNS is wobbling. In so doing we consider a possible correlation be-

tween the perturbations at the outer boundary, i.e., on the shock wave and those at the inner boundary, or on the PNS surface. Such correlations are indeed posited as a possible cause of LESA. Although the LESA is likely to be a phenomenon that manifests itself at nonlinear levels, it is still interesting to see what influence, if any, the correlations between the perturbations at the inner and outer boundaries may have on time-independent, linearly unstable modes.

This chapter is organized as follows. We give basic equations and explain the methods and models in the next section. In section 2.2 we present the results and discussions of linear analysis. We also show the results of steady solution of perturbation equations in section 2.3. We summarize our investigation in section 2.4.

2.1 Basic formalism

In this section, we describe concisely the method we employ in this thesis for linear analysis, which is based on the Laplace transform in time of the linearized hydrodynamical equations. The background flows are assumed to be steady and spherically symmetric. Spherical harmonics expansion is also utilized for perturbations.

2.1.1 Basic equations

The basic hydrodynamics equations employed to describe accretion flows in the supernovae core are given as follows:

$$\frac{\partial \rho}{\partial t} + \boldsymbol{\nabla} \cdot (\rho \boldsymbol{v}) = 0, \tag{2.1}$$

$$\frac{\partial}{\partial t}(\rho \boldsymbol{v}) + \boldsymbol{\nabla} \cdot (\rho \boldsymbol{v}\boldsymbol{v} + P\boldsymbol{I}) = -\rho \frac{GM_{\rm PNS}}{r^2}\frac{\boldsymbol{r}}{r}, \tag{2.2}$$

$$\frac{\mathrm{d}\varepsilon}{\mathrm{d}t} + P\frac{\mathrm{d}}{\mathrm{d}t}\left(\frac{1}{\rho}\right) = q, \tag{2.3}$$

$$\frac{\partial}{\partial t}(nY_e) + \boldsymbol{\nabla} \cdot (nY_e \boldsymbol{v}) = \lambda, \tag{2.4}$$

in addition to the EoS, for which we adopt Shen EoS (Shen et al. (2011)). In the above equations, ρ, P, n, Y_e, ε and $\boldsymbol{v}$ are the density, pressure, number density of baryon, electron fraction, specific internal energy and velocity, respectively; $M_{\rm PNS}$ is the mass of PNS, which is assumed to be constant, and G is the gravitational constant; the self-gravity of accreting matter is neglected; we incorporate only the reactions of the electron-type neutrinos and anti-neutrinos, which are symbolically denoted by q and λ and are given by Bruenn (1985) (concrete expressions are given in section 2.1.4).

The neutrino transfer calculation is replaced with the light-bulb approximation (Ohnishi et al. (2006); Scheck et al. (2006)): the luminosity is then constant in radius and is approximated as

$$L_{\nu_e} = \frac{7}{16} 4\pi r_{\nu_e}^2 \sigma T_{\nu_e}^4, \tag{2.5}$$

where σ is the Stefan-Boltzmann constant and r_{ν_e} and T_{ν_e} are the radius and temperature of the neutrino sphere for ν_e; $L_{\bar{\nu}_e}$ is treated in the same way. These neutrino luminosities (L_{ν_e} and $L_{\bar{\nu}_e}$) and temperatures (T_{ν_e} and $T_{\bar{\nu}_e}$) are model parameters. The radii of the neutrino sphere are determined from these parameters.

The unperturbed background flows are given as spherically symmetric steady solutions for appropriate boundary conditions. They satisfy the following equations:

$$\frac{1}{r^2}\frac{\mathrm{d}}{\mathrm{d}r}\left(\rho_0 v_{r0} r^2\right) = 0, \tag{2.6}$$

$$v_{r0}\frac{\mathrm{d}v_{r0}}{\mathrm{d}r} + \frac{1}{\rho_0}\frac{\mathrm{d}P_0}{\mathrm{d}r} = -\rho_0\frac{GM_{\rm PNS}}{r^2}, \tag{2.7}$$

$$v_{r0}\frac{\mathrm{d}\varepsilon_0}{\mathrm{d}r} - \frac{P_0 v_{r0}}{{\rho_0}^2}\frac{\mathrm{d}\rho_0}{\mathrm{d}r} = q_0, \tag{2.8}$$

$$\rho_0 v_{r0}\frac{\mathrm{d}Y_{e0}}{\mathrm{d}r} = \lambda_0 m_b, \tag{2.9}$$

where m_b is nucleonic mass and the subscript 0 means unperturbed quantities. At the shock front, which is assumed to be at rest in the background flow, the Rankine-Hugoniot relations should be satisfied:

$$\rho_0^{(u)} v_0^{(u)} = \rho_0^{(d)} v_0^{(d)}, \tag{2.10}$$

$$\rho_0^{(u)} {v_0^{(u)}}^2 + P_0^{(u)} v_0^{(u)} = \rho_0^{(d)} {v_0^{(d)}}^2 + P_0^{(d)} v_0^{(d)}, \tag{2.11}$$

$$\epsilon_0^{(u)} + \frac{1}{2}{v_0^{(u)}}^2 + \frac{P_0^{(u)}}{\rho_0^{(u)}} = \epsilon_0^{(d)} + \frac{1}{2}{v_0^{(d)}}^2 + \frac{P_0^{(d)}}{\rho_0^{(d)}}, \tag{2.12}$$

where the superscripts (u) and (d) mean variables in the upstream and downstream of the shock, respectively. We assume further that matter is freely falling with the radial velocity $v_r = \sqrt{2GM_{\rm PNS}/m_b r}$ outside the shock wave with the pressure being negligible. Once the mass accretion rate, another model parameter, is specified, the density is obtained as a function of radius. By solving these equations, radius of the stationary shock wave $r_{\rm sh,0}$ is determined by imposing the inner boundary condition that the density should be $10^{11}\,\mathrm{g/cm^3}$ at r_{ν_e}, an approximation to the real condition that the optical depth to r_{ν_e} from infinity should be 2/3.

Following Lai and Goldreich (2000) and Takahashi et al. (2016), perturbed quantities are expanded as

$$\delta X(\boldsymbol{r}, t) = \sum_{l,m} \delta X^{(l,m)}(r,t) Y_{l,m}(\theta,\phi), \tag{2.13}$$

where X denotes scalar variables and $Y_{l,m}(\theta,\phi)$ is the spherical harmonics with the polar and azimuth indices l and m. The velocity perturbation, on the other hand, is expanded with the vector spherical harmonics as follows:

$$\begin{aligned}\delta\boldsymbol{v}(\boldsymbol{r}, t) = & \sum_{l,m} \delta v_r^{(l,m)}(r,t) Y_{l,m}(\theta,\phi)\hat{\boldsymbol{r}} \\ & + \delta v_\perp^{(l,m)}(r,t)\left[\hat{\boldsymbol{\theta}}\frac{\partial Y_{lm}}{\partial\theta} + \frac{\hat{\boldsymbol{\phi}}}{\sin\theta}\frac{\partial Y_{lm}}{\partial\phi}\right] \\ & + \delta v_{rot}^{(l,m)}(r,t)\left[-\hat{\boldsymbol{\phi}}\frac{\partial Y_{lm}}{\partial\theta} + \frac{\hat{\boldsymbol{\theta}}}{\sin\theta}\frac{\partial Y_{lm}}{\partial\phi}\right],\end{aligned} \tag{2.14}$$

in which the unit vectors in the spherical coordinates are denoted by $\hat{\boldsymbol{r}}, \hat{\boldsymbol{\theta}}$, and $\hat{\boldsymbol{\phi}}$. The linearized equations of the hydrodynamics equations (Eqs. (2.1)-(2.4)) with different (l, m)

are decoupled from each other, since the background flow is assumed to be spherically symmetric, and are written symbolically as

$$\frac{\partial \boldsymbol{y}^{(l,m)}}{\partial r}(r,t) = A(r)\frac{\partial \boldsymbol{y}^{(l,m)}}{\partial t}(r,t) + B^{(l)}(r)\boldsymbol{y}^{(l,m)}(r,t), \tag{2.15}$$

where $\boldsymbol{y}^{(l,m)}(r,t)$ denotes the vector consisting of the (l,m) component of the perturbed quantities given as

$$\boldsymbol{y}(r,t) = \left(\frac{\delta\rho}{\rho_0}, \frac{\delta v_r}{v_{r0}}, \frac{\delta v_\perp}{v_{r0}}, \frac{\delta\varepsilon}{\varepsilon_0}, \frac{\delta Y_e}{Y_{e0}}, \frac{\delta v_{\rm rot}}{v_{r0}}\right)^T, \tag{2.16}$$

where $(\cdots)^T$ means transposition. Note that we take ρ, ε, Y_e as independent thermodynamic variables. The coefficient matrices, $A(r)$ and $B^{(l)}(r)$, are made of the unperturbed quantities alone (I will show these later) and are independent of m because of the spherical symmetry of the background. I solved the linearized equations (2.15) in the region between the standing shock ($r = r_{\rm sh,0}$) and the PNS surface ($r = r_{\nu_e}$) in the unperturbed state. Hereafter the subscripts 0 and (l,m) are omitted for notational simplicity.

The coefficient matrices, $A(r)$ and $B^{(l)}(r)$, are written as follows: the matrices in the basic equations in the form of

$$M\frac{\partial \boldsymbol{y}}{\partial t} + A'\frac{\partial \boldsymbol{y}}{\partial r} + B'^{(l)}\boldsymbol{y} = \boldsymbol{0}, \tag{2.17}$$

are given as

$$M(r) = \begin{pmatrix} 1 & 0 & 0 & 0 & 0 & 0 \\ 0 & 1 & 0 & 0 & 0 & 0 \\ 0 & 0 & 1 & 0 & 0 & 0 \\ -\dfrac{p}{\rho v_r^2} & 0 & 0 & \dfrac{\varepsilon}{v_r^2} & 0 & 0 \\ 0 & 0 & 0 & 0 & 1 & 0 \\ 0 & 0 & 0 & 0 & 0 & 1 \end{pmatrix}, \tag{2.18}$$

$$A'(r) = \begin{pmatrix} v_r & v_r & 0 & 0 & 0 & 0 \\ \dfrac{1}{v_r}\dfrac{\partial p}{\partial \rho} & v_r & 0 & \dfrac{\varepsilon}{\rho v_r}\dfrac{\partial p}{\partial \varepsilon} & \dfrac{Y_e}{\rho v_r}\dfrac{\partial p}{\partial Y_e} & 0 \\ 0 & 0 & v_r & 0 & 0 & 0 \\ -\dfrac{p}{\rho v_r} & 0 & 0 & \dfrac{\varepsilon}{v_r} & 0 & 0 \\ 0 & 0 & 0 & 0 & v_r & 0 \\ 0 & 0 & 0 & 0 & 0 & v_r \end{pmatrix}, \tag{2.19}$$

$$B'^{(l)}(r) = \begin{pmatrix} 0 & 0 & -v_r\dfrac{l(l+1)}{r} & 0 & 0 & 0 \\ B'_{11} & 2\dfrac{\mathrm{d}v_r}{\mathrm{d}r} & 0 & \dfrac{1}{\rho v_r}\dfrac{\mathrm{d}}{\mathrm{d}r}\left(\varepsilon\dfrac{\partial p}{\partial \varepsilon}\right) & \dfrac{1}{\rho v_r}\dfrac{\mathrm{d}}{\mathrm{d}r}\left(Y_e\dfrac{\partial p}{\partial Y_e}\right) & 0 \\ \dfrac{1}{r v_r}\dfrac{\partial p}{\partial \rho} & 0 & \dfrac{v_r}{r} + \dfrac{\mathrm{d}v_r}{\mathrm{d}r} & \dfrac{\varepsilon}{r\rho v_r}\dfrac{\partial p}{\partial \varepsilon} & \dfrac{Y_e}{r\rho v_r}\dfrac{\partial p}{\partial Y_e} & 0 \\ B'_{41} & \dfrac{1}{v_r}\left(\dfrac{\mathrm{d}\varepsilon}{\mathrm{d}r} - \dfrac{p}{\rho^2}\dfrac{\mathrm{d}\rho}{\mathrm{d}r}\right) & 0 & B'_{44} & B'_{45} & 0 \\ \dfrac{v_r}{Y_e}\dfrac{\mathrm{d}Y_e}{\mathrm{d}r} - \dfrac{m_b}{Y_e}\dfrac{\partial \lambda}{\partial \rho} & \dfrac{v_r}{Y_e}\dfrac{\mathrm{d}Y_e}{\mathrm{d}r} & 0 & -\dfrac{m_b\varepsilon}{\rho Y_e}\dfrac{\partial \lambda}{\partial \varepsilon} & \dfrac{v_r}{Y_e}\dfrac{\mathrm{d}Y_e}{\mathrm{d}r} - \dfrac{m_b}{\rho}\dfrac{\partial \lambda}{\partial Y_e} & 0 \\ 0 & 0 & 0 & 0 & 0 & \dfrac{v_r}{r} + \dfrac{\mathrm{d}v_r}{\mathrm{d}r} \end{pmatrix}, \tag{2.20}$$

with

$$B'_{11} = \frac{1}{\rho v_r}\frac{\mathrm{d}}{\mathrm{d}r}\left(\rho\frac{\partial p}{\partial \rho}\right) - \frac{1}{\rho v_r}\frac{\mathrm{d}p}{\mathrm{d}r}, \tag{2.21}$$

$$B'_{41} = \frac{1}{v_r}\left(\frac{p}{\rho^2}\frac{\mathrm{d}\rho}{\mathrm{d}r} - \frac{1}{\rho}\frac{\mathrm{d}\rho}{\mathrm{d}r}\frac{\partial p}{\partial \rho} - \frac{\rho}{v_r}\frac{\partial q}{\partial \rho}\right), \tag{2.22}$$

$$B'_{44} = \frac{1}{v_r}\left(\frac{\mathrm{d}\varepsilon}{\mathrm{d}r} - \frac{\varepsilon}{\rho^2}\frac{\mathrm{d}\rho}{\mathrm{d}r}\frac{\partial p}{\partial \varepsilon} - \frac{\varepsilon}{v_r}\frac{\partial q}{\partial \varepsilon}\right), \tag{2.23}$$

$$B'_{45} = -\frac{1}{v_r}\left(\frac{Y_e}{\rho^2}\frac{\mathrm{d}\rho}{\mathrm{d}r}\frac{\partial p}{\partial Y_e} + \frac{Y_e}{v_r}\frac{\partial q}{\partial Y_e}\right). \tag{2.24}$$

Note that in the above expression, the fixed variables in the partial derivatives are omitted for notational simplicity. The Eq. (2.15) is obtained by multiplying equation (2.17) by A^{-1} from the left and defining $A := -\left(A'\right)^{-1} M$ and $B^{(l)} := -\left(A'\right)^{-1} B'^{(l)}$.

2.1.2 Outer and inner boundary conditions and an initial condition

Outer boundary condition: Rankine-Hugoniot relations

The outer boundary condition imposed at the shock radius is given by the linearized Rankine-Hugoniot relation (RH relation).

Usual RH relation is derived as follows. In general, continuous equation with source term is expressed as

$$\frac{\partial U}{\partial t} + \boldsymbol{\nabla}\cdot\boldsymbol{F} = S, \tag{2.25}$$

where U, $\boldsymbol{F}$ and S are conservative quantity, its flux and source, respectively. We consider volume integration over the cylindrical region V that enclose the shock front $d\sigma$ and furthermore the bottom surfaces and the shock front move with the velocity $\boldsymbol{q}$:

$$\frac{\mathrm{d}}{\mathrm{d}t}\int_V U dV = \int_{\partial V}(U\boldsymbol{q} - \boldsymbol{F})\cdot d\boldsymbol{S} + \int_V S dV. \tag{2.26}$$

By approaching both bottom surfaces to the shock front infinitesimally, the rests are surface integral on bottom surfaces and we obtain

$$[(U\boldsymbol{q} - \boldsymbol{F})\cdot\boldsymbol{n}] = 0, \tag{2.27}$$

where $\boldsymbol{n}$ is the normal vector the spherical shock surface and the bracketed symbol, $[X] := X^{(\mathrm{d})} - X^{(\mathrm{u})}$, is a jump of a quantity X across the shock.. This is called RH relation and Eqs (2.10), (2.11) and (2.12) are in fact given by applying Eq. 2.27 to hydrodynamics equations (2.1), (2.2) and (2.3), respectively, assuming the spherical symmetry and steady state. Note in passing that RH relation for equation (2.4) gives

$$[Y_e] = 0. \tag{2.28}$$

Let us consider a linearized equation for

$$[f_0]_{\boldsymbol{r}_0} = 0, \tag{2.29}$$

where $\boldsymbol{r}_0$ is the position of the shock and f_0 is a arbitrary function of physical variables. If we add perturbations to the shock position and the variables, i.e.,

$$f(\boldsymbol{r}) = f_0(\boldsymbol{r}) + \delta f(\boldsymbol{r}), \quad \boldsymbol{r} = \boldsymbol{r}_0 + \delta\boldsymbol{r}, \tag{2.30}$$

then we get

$$[f_0 + \delta f]_{\boldsymbol{r}_0+\delta\boldsymbol{r}} = [f_0]_{\boldsymbol{r}_0} + [\delta f]_{\boldsymbol{r}_0} + [\nabla f]_{\boldsymbol{r}_0} \cdot \delta\boldsymbol{r}. \tag{2.31}$$

Combining with $[f_0]_{\boldsymbol{r}_0} = 0$ and $[f_0 + \delta f]_{\boldsymbol{r}_0+\delta\boldsymbol{r}} = 0$, we obtain

$$[\delta f]_{\boldsymbol{r}_0} + [\nabla f]_{\boldsymbol{r}_0} \cdot \delta\boldsymbol{r} = 0. \tag{2.32}$$

We apply (2.32) to the case with $f = (U\boldsymbol{q} - \boldsymbol{F}) \cdot \boldsymbol{n}$. If we express the radius of the shock front as $r_{\rm sh} := h(\theta, \phi, t)$ and define a new function $\psi(r_{\rm sh}, \theta, \phi, t) = r_{\rm sh} - h(\theta, \phi, t))$, then the components of $\boldsymbol{n}$ and $\boldsymbol{q}$ in the spherical coordinate are expressed as

$$\boldsymbol{n} = \frac{\nabla\psi}{|\nabla\psi|} = \frac{1}{|\nabla\psi|}\left(1, -\frac{1}{r_{\rm sh}}\frac{\partial h}{\partial\theta}, -\frac{1}{r_{\rm sh}\sin\theta}\frac{\partial h}{\partial\phi}\right)^T, \tag{2.33}$$

$$\boldsymbol{q} = \frac{\partial \boldsymbol{r}_{\rm sh}}{\partial t} = \left(\frac{\partial h}{\partial t}, 0, 0\right)^T. \tag{2.34}$$

Inner products $\boldsymbol{q} \cdot \boldsymbol{n}$ and $\boldsymbol{v} \cdot \boldsymbol{n}$ are expressed as

$$\boldsymbol{q} \cdot \boldsymbol{n} = \frac{1}{|\nabla\psi|}\frac{\partial h}{\partial t}, \tag{2.35}$$

$$\boldsymbol{v} \cdot \boldsymbol{n} = \frac{1}{|\nabla\psi|}\left(v_r - \frac{v_\theta}{r_{\rm sh}}\frac{\partial h}{\partial\theta} - \frac{v_\phi}{r_{\rm sh}\sin\theta}\frac{\partial h}{\partial\phi}\right), \tag{2.36}$$

and Eq. (2.27) is reduced to

$$\left[U\frac{\partial h}{\partial t} - \boldsymbol{F}\cdot\boldsymbol{n}\right]_{\rm r} = 0. \tag{2.37}$$

By using Eqs. (2.37), (2.32) and hydrodynamics equations (2.1), (2.2), (2.3) and (2.4) the linearized Rankine-Hugoniot relations with the perturbation to spherically symmetric steady background are schematically given by

$$P^{(d)}\boldsymbol{y}(r_{\rm sh}, t) = P^{(u)}\boldsymbol{z}(t) + \frac{\partial}{\partial t}\frac{\delta r_{\rm sh}}{r_{\rm sh}}\boldsymbol{c}' + \frac{\delta r_{\rm sh}}{r_{\rm sh}}\boldsymbol{d}', \tag{2.38}$$

where $\delta r_{\rm sh}(t)$ is the time-dependent perturbation to the shock radius; P is a matrix and $\boldsymbol{c}$ and $\boldsymbol{d}$ are vectors, which depend only on the background quantities and they are written as

$$P = \begin{pmatrix} 1 & 1 & 0 & 0 & 0 & 0 \\ v_r + \dfrac{1}{v_r}\dfrac{\partial p}{\partial\rho} & 2v_r & 0 & \dfrac{\varepsilon}{j}\dfrac{\partial p}{\partial\varepsilon} & \dfrac{Y_e}{j}\dfrac{\partial p}{\partial Y_e} & 0 \\ 0 & 0 & v_r & 0 & 0 & 0 \\ \dfrac{E}{\rho} + \dfrac{\partial p}{\partial\rho} & \dfrac{E + p + \rho v_r^2}{\rho} & 0 & \varepsilon + \dfrac{\varepsilon}{\rho}\dfrac{\partial p}{\partial\varepsilon} & \dfrac{Y_e}{\rho}\dfrac{\partial p}{\partial Y_e} & 0 \\ 1 & 1 & 0 & 0 & 1 & 0 \\ 0 & 0 & 0 & 0 & 0 & v_r \end{pmatrix}, \tag{2.39}$$

$$\boldsymbol{c}' = \left(\frac{r_{\rm sh}\,[\rho]}{j},\ 0,\ 0,\ \frac{r_{\rm sh}\,[E]}{j},\ \frac{r_{\rm sh}\,[\rho]}{j},\ 0\right)^T, \tag{2.40}$$

$$\boldsymbol{d}' = \left(0,\ 2\,[v_r] + \frac{GM\,[\rho]}{r_{\rm sh} j},\ \frac{[p]}{j},\ -\frac{r_{\rm sh}\,[\rho q]}{j},\ -\frac{r_{\rm sh} m_b\,[\lambda]}{j Y_e},\ 0\right)^T. \tag{2.41}$$

In the above expression, $j := \rho_0^{(\mathrm{u})} v_{r0}^{(\mathrm{u})} = \rho_0^{(\mathrm{d})} v_{r0}^{(\mathrm{d})}$ is the mass flux. $\boldsymbol{z}$ is the perturbation in the upstream flow which is originated from turbulence in the outer envelope and is approximately written as (Takahashi et al. (2016))

$$\frac{\delta\rho}{\rho_0} = \sin(\omega_{\mathrm{up}} t + \varphi), \tag{2.42}$$

$$\frac{\delta v_r}{v_{r0}} = -0.5 \sin(\omega_{\mathrm{up}} t + \varphi), \tag{2.43}$$

$$\frac{\delta\varepsilon}{\varepsilon_0} = \sin(\omega_{\mathrm{up}} t + \varphi). \tag{2.44}$$

The oscillation frequency ω_{up} is another free parameter and we set $\omega_{\mathrm{up}} = 100\,\mathrm{Hz}$.

As a result, by multiplying Eq. 2.38 by $\left(P^{(\mathrm{d})}\right)^{-1}$ from the left and defining $R := \left(P^{(\mathrm{d})}\right)^{-1} P^{(\mathrm{u})}$, $\boldsymbol{c} := \left(P^{(\mathrm{d})}\right)^{-1} \boldsymbol{c}'$ and $\boldsymbol{d} := \left(P^{(\mathrm{d})}\right)^{-1} \boldsymbol{d}'$, the outer boundary condition at the shock is written as

$$\boldsymbol{y}(r_{\mathrm{sh}}, t) = R\boldsymbol{z}(t) + \frac{\partial}{\partial t}\frac{\delta r_{\mathrm{sh}}(t)}{r_{\mathrm{sh}}}\boldsymbol{c} + \frac{\delta r_{\mathrm{sh}}(t)}{r_{\mathrm{sh}}}\boldsymbol{d}. \tag{2.45}$$

Inner boundary condition and initial condition

The inner boundary is set at the PNS surface. Since the perturbation of the shock radius is the only variable remaining after imposing the outer boundary condition, we can give only one condition at the inner boundary. It is symbolically written as

$$f(\boldsymbol{y}(r_{\nu_e}, t), t) = 0. \tag{2.46}$$

Detailed forms of the function f are depend on the model and shown later in sections 2.2 and 2.3 (see equations (2.106) and (2.121))

In principle, we can set any initial condition to the perturbation:

$$\boldsymbol{y}(r, t = 0) = \boldsymbol{y}_0(r) \quad (r_{\nu_e} < r < r_{\mathrm{sh}}). \tag{2.47}$$

In this thesis, however, we set $\boldsymbol{y}_0(r) = 0$ for simplicity. We are hence concerned only with the perturbations generated at the boundaries.

To summarize this subsection, the problem is now reduced to solving equations (2.15), (2.45), (2.46) and (2.47) to obtain the time evolution of the perturbation of the shock radius, $\delta r_{\mathrm{sh}}/r_{\mathrm{sh}}(t)$, as an initial-boundary-value problem.

2.1.3 Laplace transformation of linearized system

To solve this initial-boundary-value problem, we use the Laplace transform with respect to time defined as

$$f^*(s) := \int_0^\infty f(t)\mathrm{e}^{-st}\mathrm{d}t, \tag{2.48}$$

where s is a complex variable. Hereafter, the superscript "$*$" means Laplace-transformed functions, which are complex in general. Eqs. (2.15), (2.45) and (2.46) are Laplace-transformed into the following forms:

$$\frac{\mathrm{d}\boldsymbol{y}^*}{\mathrm{d}r}(r, s) = (sA + B)\boldsymbol{y}^*(r, s) - A\boldsymbol{y}_0(r), \tag{2.49}$$

$$\boldsymbol{y}^*(r_{\mathrm{sh}}, s) = (s\boldsymbol{c} + \boldsymbol{d})\frac{\delta r_{\mathrm{sh}}^*(s)}{r_{\mathrm{sh}}} + R\boldsymbol{z}^*(s), \tag{2.50}$$

$$f^*(\boldsymbol{y}^*(r_{\nu_e}, s), s) = 0. \tag{2.51}$$

In linear analysis, the inner boundary condition is generally written as

$$f^*(\boldsymbol{y}^*(r_{\nu_e}, s), s) = \boldsymbol{a}^*(s) \cdot \boldsymbol{y}^*(r_{\nu_e}, s) + b^*(s) = 0, \tag{2.52}$$

where $\boldsymbol{a}^*$ and b^* are some functions of s. Eq. (2.49) is a system of ordinary differential equations and can be easily integrated. Combined with Eqs. (2.50) and (2.51), they determine $\delta r^*_{\rm sh}/r_{\rm sh}(s)$.

Following the common practice, we assume that $\delta r_{\rm sh}/r_{\rm sh}(t)$ is written as a superposition of eigenmodes as

$$\frac{\delta r_{\rm sh}}{r_{\rm sh}}(t) = \sum_j a_j \mathrm{e}^{\Omega_j t} \mathrm{e}^{i(\omega_j t + \phi_j)}, \tag{2.53}$$

where Ω_j and ω_j are the growth or damping rate and the oscillation frequency of the j-th mode ($j = 1, 2, 3, \cdots$), respectively, and a_j is the amplitude of the same mode, which is assumed to be independent of t. We can assume $\omega_j \geq 0$ and $-\pi/2 \leq \phi_j < \pi/2$ for all j without loss of generality. Then the Laplace transformation of $\delta r_{\rm sh}/r_{\rm sh}(t)$ is written as

$$\frac{\delta r^*_{\rm sh}}{r_{\rm sh}}(s) = \sum_j a_j \frac{\mathrm{e}^{i\phi_j}}{(s - \Omega_j) - i\omega_j}, \tag{2.54}$$

which has poles at $\Omega_j + i\omega_j$ ($j = 1, 2, 3, \cdots$). The stability or instability of the standing shock can be judged from the sign of Ω_j.

2.1.4 Model parameters and the treatment of neutrino heating and cooling in the unperturbed flows

We assume $L_\nu := L_{\nu_e} = L_{\bar{\nu}_e}$ for simplicity and change its value as a free parameter. The values of the other parameters that specify the unperturbed background flow are set as follows: the mass of PNS is $M_{\rm PNS} = 1.4 M_\odot$; the mass accretion rate and neutrino temperatures are fixed to $\dot{M} = 0.6$ M$_\odot$ s^{-1} and $T_{\nu_e} = T_{\bar{\nu}_e} = 4.5$ MeV, respectively; the entropy and Y_e just ahead of the shock wave are set as $S = 3k_B$ and $Y_e = 0.5$, respectively, where k_B is the Boltzmann constant; matter is assumed to free-fall from infinity onto the shock. We employ Shen EoS (Shen et al. (2011)), which takes into account the contributions from nucleons, nuclei, α particles, photons, electrons and positrons.

The neutrino heating and cooling functions, q and λ, are evaluated under the light bulb approximation as follows:

$$q = -\sum_\alpha \frac{1}{\rho} \frac{4\pi c}{(2\pi\hbar c)^3} \int_0^\infty \mathrm{d}\epsilon\, \epsilon^3 \left[j_\alpha(\epsilon) - (j_\alpha(\epsilon) + \kappa_\alpha(\epsilon)) f_\alpha(\boldsymbol{x}, \epsilon) \right], \tag{2.55}$$

$$\lambda = -\sum_\alpha i_\alpha \frac{m_b}{\rho} \frac{4\pi c}{(2\pi\hbar c)^3} \int_0^\infty \mathrm{d}\epsilon\, \epsilon^2 \left[j_\alpha(\epsilon) - (j_\alpha(\epsilon) + \kappa_\alpha(\epsilon)) f_\alpha(\boldsymbol{x}, \epsilon) \right], \tag{2.56}$$

where α specifies the neutrino species and i_α is defined as

$$i_\alpha = \begin{cases} 1 & \text{for } \nu_e \\ -1 & \text{for } \bar{\nu}_e. \end{cases} \tag{2.57}$$

ϵ denotes the neutrino energy and κ_α and j_α are the absorptivity and emissivity of each neutrino species, for which we employed the Bruenn's rates (Bruenn (1985)). The distribution function of neutrinos is denoted by f_α and is approximated by the scaled Fermi-Dirac distribution with a vanishing chemical potential:

$$f_\alpha(\boldsymbol{x}, \epsilon) = \frac{1}{1 + \exp(\epsilon / k_B T_\alpha)} g(r), \tag{2.58}$$

Table 2.1: Background flow models considered. r_ν, $\omega_{\rm acc}$, $\omega_{\rm pac}$, $r_{\rm gain}$ and $\bar{\omega}_{BV}$ are the neutrino sphere radius, the frequency of the advective-acoustic cycle, the frequency of purely acoustic cycle, the gain radius and the Brunt-Väisälä frequency, respectively. χ parameter is defined in the text (see Eq. (2.62)).

Model	L_ν [10^{52} erg s^{-1}]	$r_{\rm sh}$ [10^6 cm]	r_ν [10^6 cm]	$\omega_{\rm aac}$ [ms^{-1}]	$\omega_{\rm pac}$ [ms^{-1}]	$r_{\rm gain}$ [10^6 cm]	$\bar{\omega}_{BV}$ [ms^{-1}]	χ
M06L20	2.0	4.75	2.94	1.56	5.90	4.75	-	0
M06L25	2.5	5.79	3.28	0.973	3.99	5.79	-	0
M06L30	3.0	6.93	3.60	0.644	2.84	6.45	0.270	0.143
M06L35	3.5	8.22	3.89	0.444	2.07	6.80	0.320	0.603
M06L40	4.0	9.78	4.15	0.313	1.52	7.18	0.340	1.41
M06L45	4.5	11.8	4.41	0.221	1.10	7.73	0.332	2.56
M06L50	5.0	14.6	4.64	0.152	0.754	8.44	0.302	4.31
M06L55	5.5	19.3	4.87	0.0974	0.470	9.42	0.238	6.77
M06L60	6.0	29.5	5.09	0.0510	0.232	10.8	0.153	11.1

where $g(r)$ is the so-called geometrical factor defined as

$$g(r) = \frac{1 - \sqrt{1 - (r_\nu/r)^2}}{2}, \tag{2.59}$$

as a function of $r = |\boldsymbol{x}|$ in which the solid angle of the PNS from the point $\boldsymbol{x}$ is taken into account (see Ohnishi et al. (2006) for more details).

The models of unperturbed flow employed in this thesis are shown in Table 2.1. The radius of neutrino sphere, the characteristic frequencies of advective-acoustic and purely acoustic cycles and the gain radius for these background models are listed in it. Advective-acoustic cycle and purely acoustic cycle, $\omega_{\rm aac}$ and $\omega_{\rm pac}$ respectively, are given as

$$\omega_{\rm aac} = 2\pi \left[\int_{r_\nu}^{r_{\rm sh}} \left(\frac{1}{|v_r|} + \frac{1}{c_s - |v_r|} \right) {\rm d}r \right]^{-1}, \tag{2.60}$$

$$\omega_{\rm pac} = 2\pi \left[\int_{r_\nu}^{r_{\rm sh}} \left(\frac{1}{c_s + |v_r|} + \frac{1}{c_s - |v_r|} \right) {\rm d}r \right]^{-1}, \tag{2.61}$$

where c_s is the sound speed. They are the cycles of perturbations between the shock front and PNS surface which are related to the frequencies of SASI (Foglizzo (2009)). χ-parameter is defined as

$$\chi = \int_{r_{\rm gain}}^{r_{\rm sh}} \left| \frac{\omega_{BW}}{v_r} \right| {\rm d}r, \tag{2.62}$$

where $r_{\rm gain}$ is the gain radius, i.e., the bottom boundary of the region with negative entropy gradients and ω_{BW} is the Brunt-Väisälä frequency:

$$\omega_{BV} \;=\; \sqrt{\frac{GM}{r^2} \left| \frac{1}{\Gamma_1 p} \frac{{\rm d}p}{{\rm d}r} - \frac{1}{\rho} \frac{{\rm d}\rho}{{\rm d}r} \right|}, \tag{2.63}$$

with

$$\Gamma_1 \;:=\; \left(\frac{\partial \ln p}{\partial \ln \rho} \right)_{S, Y_e}. \tag{2.64}$$

ω_{BV} represents the maximum growth rate of the convective instability and then the χ-parameter means the ratio between the growth rate and the timescale which the accretion matter dwells in the convectively unstable region. According to Foglizzo et al. (2006), $\chi \gtrsim 3$ is the empirical condition for the flow being convectively unstable. I also list the mean Brunt-Väisälä frequency for models with a non-vanishing gain region, which is defined by

$$\bar{\omega}_{BV} = \frac{1}{r_{\rm sh} - r_{\rm gain}} \int_{r_{\rm gain}}^{r_{\rm sh}} \omega_{BV} {\rm d}r. \tag{2.65}$$

2.1.5 Fluctuations of neutrino luminosity

To model the perturbation of neutrino luminosity, I introduce a new degree of freedom, i.e. the fluctuation of neutrino temperature δT_α, and expand it as usual:

$$\delta T_\alpha = \sum_{l,m} \delta T_\alpha^{(l,m)}(t) Y_{lm}(\theta, \phi), \tag{2.66}$$

which is consistent with the black body approximation employed for the neutrino luminosity (see Eq. (2.5)). We determine δT_α by an additional inner boundary condition generally written as

$$\left(\frac{\delta T_\alpha}{T_\alpha}\right)^* (s) = \boldsymbol{w}(s) \cdot \boldsymbol{y}^*(r_{\nu_e}, s). \tag{2.67}$$

The fluctuation of the neutrino temperature affects q and λ:

$$\delta q = \frac{\partial q}{\partial \rho}\delta\rho + \frac{\partial q}{\partial \varepsilon}\delta\varepsilon + \frac{\partial q}{\partial Y_e}\delta Y_e + \delta q_\nu, \tag{2.68}$$

$$\delta \lambda = \frac{\partial \lambda}{\partial \rho}\delta\rho + \frac{\partial \lambda}{\partial \varepsilon}\delta\varepsilon + \frac{\partial \lambda}{\partial Y_e}\delta Y_e + \delta \lambda_\nu, \tag{2.69}$$

where δq_ν and $\delta\lambda_\nu$ are the new terms compared with the case with no fluctuations of neutrino luminosity. They are written as

$$\delta q_\nu = \sum_\alpha \frac{1}{\rho} \frac{4\pi c}{(2\pi\hbar c)^3} \int_0^\infty {\rm d}\epsilon\, \epsilon^3 \left[(j_\alpha(\epsilon) + \kappa_\alpha(\epsilon))\, \delta f_\alpha(\boldsymbol{x}, \epsilon) \right], \tag{2.70}$$

$$\delta \lambda_\nu = \sum_\alpha i_\alpha \frac{m_b}{\rho} \frac{4\pi c}{(2\pi\hbar c)^3} \int_0^\infty {\rm d}\epsilon\, \epsilon^2 \left[(j_\alpha(\epsilon) + \kappa_\alpha(\epsilon))\, \delta f_\alpha(\boldsymbol{x}, \epsilon) \right], \tag{2.71}$$

where the perturbation to the neutrino distribution is given as

$$\delta f_\alpha(\boldsymbol{x}, \epsilon) = \frac{\beta_\alpha \epsilon {\rm e}^{\beta_\alpha \epsilon}}{\left(1 + {\rm e}^{\beta_\alpha \epsilon}\right)^2} g(|\boldsymbol{x}|) \frac{\delta T_\alpha}{T_\alpha}, \tag{2.72}$$

with $\beta_\alpha = 1/k_B T_\alpha$. Basic equation for the vector $\boldsymbol{y}$ is then modified as

$$M\frac{\partial \boldsymbol{y}}{\partial t} + A'\frac{\partial \boldsymbol{y}}{\partial r} + B'^{(l)}\boldsymbol{y} = \boldsymbol{u}', \tag{2.73}$$

where matrices $M(r)$, $A'(r)$ and $B'^{(l)}(r)$ are the same as those given in Eqs. (2.18), (2.19) and (2.20), respectively, and the new term $\boldsymbol{u}'$ is written as

$$\boldsymbol{u}' = \left(0, 0, 0, \frac{1}{v_r}\delta q_\nu, \frac{m_b}{\rho Y_e}\delta\lambda_\nu, 0\right)^T. \tag{2.74}$$

By defining $A := -A'^{-1}M$, $B^{(l)} := -A'^{-1}B'^{(l)}$ and

$$\boldsymbol{u}\frac{\delta T_\alpha}{T_\alpha} := A'^{-1}\boldsymbol{u}', \tag{2.75}$$

we obtain the Laplace-transformed linearized equation corresponding to Eq. (2.17):

$$\frac{\mathrm{d}\boldsymbol{y}^*}{\mathrm{d}r}(r,s) = (sA + B^{(l)})\boldsymbol{y}^*(r,s) - A\boldsymbol{y}_0(r) + \boldsymbol{u}\frac{\delta T_\alpha^*}{T_\alpha}. \tag{2.76}$$

In summary, I solve the linear equation (2.76) when the perturbation to the neutrino luminosity is taken into account. Then the remaining degrees of freedom are $\delta r_{\rm sh}^*$ and δT_α^* after imposing the Rankine-Hugoniot relations at the outer boundary, which are determined from the two conditions given in Eq. (2.52) and and an additional condition (see (2.109)).

2.1.6 The formal solution of linearized equations

I present here the formal solution of Eq. (2.76) written again as

$$\frac{\mathrm{d}\boldsymbol{y}^*}{\mathrm{d}r}(r,s) = (sA + B^{(l)})\boldsymbol{y}^*(r,s) - A\boldsymbol{y}_0(r) + \boldsymbol{u}\frac{\delta T_\alpha^*}{T_\alpha}. \tag{2.77}$$

This can be integrated formally as

$$\begin{aligned}
\boldsymbol{y}^*(r,s) &= \Lambda^*(r,s)\boldsymbol{y}^*(r_{\rm sh},s) - \Lambda^*(r,s)\int_{r_{\rm sh}}^{r}\mathrm{d}r'\Lambda^{*-1}(r',s)A(r')\boldsymbol{y}_0(r') \\
&\quad + \Lambda^*(r,s)\int_{r_{\rm sh}}^{r}\mathrm{d}r'\Lambda^{*-1}(r',s)\boldsymbol{u}\left(\frac{\delta T_\alpha}{T_\alpha}\right)^*, \\
&= \Lambda^*(r,s)\boldsymbol{y}^*(r_{\rm sh},s) - \boldsymbol{h}^*[\boldsymbol{y}_0](r,s) + \boldsymbol{L}^*(r,s)\left(\frac{\delta T_\alpha}{T_\alpha}\right)^*,
\end{aligned} \tag{2.78}$$

where the matrix Λ^* and vector $\boldsymbol{h}^*[\boldsymbol{y}_0]$ and $\boldsymbol{L}^*$ are defined as

$$\Lambda^*(r,s) := \mathcal{P}\left[\exp\left(\int_{r_{\rm sh}}^{r}\mathrm{d}r'(sA+B)\right)\right], \tag{2.79}$$

$$\boldsymbol{h}^*[\boldsymbol{y}_0](r,s) := \Lambda^*(r,s)\int_{r_{\rm sh}}^{r}\mathrm{d}r'\Lambda^{*-1}(r',s)A(r')\boldsymbol{y}_0(r'), \tag{2.80}$$

$$\boldsymbol{L}^*(r,s) := \Lambda^*(r,s)\int_{r_{\rm sh}}^{r}\mathrm{d}r'\Lambda^{*-1}(r',s)\boldsymbol{u}(r'). \tag{2.81}$$

In the above expressions, $\mathcal{P}$ stands for the path-ordering operator (Peskin (2018)). Inserting the linearized Rankine-Hugoniot relation (2.50), Eq. (2.78) is evaluated at the neutrino sphere as

$$\begin{aligned}
\boldsymbol{y}^*(r_{\nu_e},s) &= \Lambda^*(r_{\nu_e},s)\left[(s\boldsymbol{c}+\boldsymbol{d})\frac{\delta r_{\rm sh}^*(s)}{r_{\rm sh}} + R\boldsymbol{z}^*(s)\right] - \boldsymbol{h}^*[\boldsymbol{y}_0](r_{\nu_e},s) - \boldsymbol{L}^*(r_\nu,s)\frac{\delta T_\alpha}{T_\alpha}(s) \\
&=: \tilde{\Lambda}^*(s)\left[(s\boldsymbol{c}+\boldsymbol{d})\frac{\delta r_{\rm sh}^*(s)}{r_{\rm sh}} + R\boldsymbol{z}^*(s)\right] - \tilde{\boldsymbol{h}}^*[\boldsymbol{y}_0](s) + \tilde{\boldsymbol{L}}^*(s)\left(\frac{\delta T_\alpha}{T_\alpha}\right)^*(s),
\end{aligned} \tag{2.82}$$

in which $\tilde{\Lambda}^*(s)$, $\tilde{\boldsymbol{h}}^*[\boldsymbol{y}_0](s)$ and $\tilde{\boldsymbol{L}}^*(s)$ are the values of Λ^*, $\boldsymbol{h}^*[\boldsymbol{y}_0]$ and $\boldsymbol{L}$ evaluated at the neutrino sphere, which are introduced just for notational simplicity.

The boundary conditions imposed at r_{ν_e} are generally written as

$$\boldsymbol{a}^*(s)\cdot\boldsymbol{y}^*(r_{\nu_e},s)+b^*(s)=0, \tag{2.83}$$

$$\left(\frac{\delta T_\alpha}{T_\alpha}\right)^*(s)=\boldsymbol{w}(s)\cdot\boldsymbol{y}^*(r_{\nu_e},s). \tag{2.84}$$

Substituting the formal solution into these two equations, we obtain the following condition:

$$\begin{aligned}&\begin{pmatrix}\boldsymbol{a}^*\cdot\tilde{\Lambda}^*(s)(s\boldsymbol{c}+\boldsymbol{d}) & \boldsymbol{a}^*\cdot\tilde{\boldsymbol{L}}^*(s)\\ \boldsymbol{w}^*\cdot\tilde{\Lambda}^*(s)(s\boldsymbol{c}+\boldsymbol{d}) & \boldsymbol{w}^*\cdot\tilde{\boldsymbol{L}}^*(s)-1\end{pmatrix}\begin{pmatrix}\delta r^*_{\rm sh}/r_{\rm sh}\\ \delta T^*_\alpha/T_\alpha\end{pmatrix}\\ &+\begin{pmatrix}\boldsymbol{a}^*(s)\cdot\tilde{\Lambda}^*(s)R\boldsymbol{z}^*(s)+\boldsymbol{a}^*(s)\cdot\tilde{\boldsymbol{h}}^*[\boldsymbol{y}_0](s)-b^*(s)\\ \boldsymbol{w}^*(s)\cdot\tilde{\Lambda}^*(s)R\boldsymbol{z}^*(s)+\boldsymbol{w}^*(s)\cdot\tilde{\boldsymbol{h}}^*[\boldsymbol{y}_0](s)\end{pmatrix}\\ &=0.\end{aligned} \tag{2.85}$$

We find from these equations the positions of poles as the zeros of

$$\begin{vmatrix}\boldsymbol{a}^*\cdot\tilde{\Lambda}^*(s)(s\boldsymbol{c}+\boldsymbol{d}) & \boldsymbol{a}^*\cdot\tilde{\boldsymbol{L}}^*(s)\\ \boldsymbol{w}^*\cdot\tilde{\Lambda}^*(s)(s\boldsymbol{c}+\boldsymbol{d}) & \boldsymbol{w}^*\cdot\tilde{\boldsymbol{L}}^*(s)-1\end{vmatrix}=0. \tag{2.86}$$

Note that they are not affected by the upstream perturbation $\boldsymbol{z}^*(s)$ but are indeed influenced by the inner boundary conditions, i.e., $\boldsymbol{a}^*(s)$ and $\boldsymbol{w}^*(s)$.

2.1.7 The amplitude of the eigenmode

If the perturbed shock radius is written as superposition of eigenmodes as Eq. (2.53), the amplitude a_j is directly related with residue of $\delta r^*_{\rm sh}/r_{\rm sh}$ at the corresponding pole in the complex plane, i.e.

$$\operatorname*{Res}_{s=\Omega_k+i\omega_k}\frac{\delta r^*_{\rm sh}}{r_{\rm sh}}=\operatorname*{Res}_{s=\Omega_k+i\omega_k}\sum_j a_j\frac{{\rm e}^{i\phi_j}}{(s-\Omega_j)-i\omega_j}=a_k e^{i\phi_k}. \tag{2.87}$$

$$\tag{2.88}$$

On the other hand, by the Cauchy's theorem,

$$\operatorname*{Res}_{s=\Omega_k+i\omega_k}\frac{\delta r^*_{\rm sh}}{r_{\rm sh}}=\frac{1}{2\pi i}\oint_C\frac{\delta r^*_{\rm sh}}{r_{\rm sh}}{\rm d}z, \tag{2.89}$$

holds where C is any closed curve in the complex plane that includes only the k-th pole inside. The right integral can be numerically obtained if we know $\delta r^*_{\rm sh}/r_{\rm sh}$.

If we neglect the fluctuations of the neutrino luminosity as in section 2.1.7, that is, we assume $\tilde{\boldsymbol{L}}(s)=0$, $\boldsymbol{w}=0$ and $\delta T_\alpha=0$ in Eq. (2.85), then the Laplace-transformed shock perturbation is written as

$$\begin{aligned}\frac{\delta r^*_{\rm sh}}{r_{\rm sh}}&=\frac{\boldsymbol{a}^*(s)\cdot\tilde{\Lambda}^*(s)R\boldsymbol{z}^*(s)+\boldsymbol{a}^*(s)\cdot\tilde{\boldsymbol{h}}^*[\boldsymbol{y}_0](s)-b^*(s)}{\boldsymbol{a}^*\cdot\tilde{\Lambda}^*(s)(s\boldsymbol{c}+\boldsymbol{d})}\\ &=\left(\frac{\delta r^*_{\rm sh}}{r_{\rm sh}}\right)_{\rm ex}+\left(\frac{\delta r^*_{\rm sh}}{r_{\rm sh}}\right)_{\rm ini}+\left(\frac{\delta r^*_{\rm sh}}{r_{\rm sh}}\right)_{\rm IB},\end{aligned} \tag{2.90}$$

where I define

$$\left(\frac{\delta r^*_{\rm sh}}{r_{\rm sh}}\right)_{\rm ex} := \frac{\boldsymbol{a}^*(s)\cdot\tilde{\Lambda}^*(s)R\boldsymbol{z}^*(s)}{\boldsymbol{a}^*\cdot\tilde{\Lambda}^*(s)(s\boldsymbol{c}+\boldsymbol{d})}, \tag{2.91}$$

$$\left(\frac{\delta r^*_{\rm sh}}{r_{\rm sh}}\right)_{\rm ini} := \frac{\boldsymbol{a}^*(s)\cdot\tilde{\boldsymbol{h}}^*[\boldsymbol{y}_0](s)}{\boldsymbol{a}^*\cdot\tilde{\Lambda}^*(s)(s\boldsymbol{c}+\boldsymbol{d})}, \tag{2.92}$$

$$\left(\frac{\delta r^*_{\rm sh}}{r_{\rm sh}}\right)_{\rm IB} := \frac{-b^*(s)}{\boldsymbol{a}^*\cdot\tilde{\Lambda}^*(s)(s\boldsymbol{c}+\boldsymbol{d})}, \tag{2.93}$$

which represent the contributions from the perturbations imposed at the outer boundary, those set initially and those given at the inner boundary, respectively. The first term (i.e. Eq. (2.91)) can be further decomposed as

$$\left(\frac{\delta r_{\rm sh}}{r_{\rm sh}}\right)^*_{\rm ex} = -\frac{\boldsymbol{a}^*(s)\cdot\tilde{\Lambda}^*(s)R\boldsymbol{z}^*(s)}{\boldsymbol{a}^*(s)\cdot\tilde{\Lambda}^*(s)(s\boldsymbol{c}+\boldsymbol{d})}, \tag{2.94}$$

$$=: \mathcal{J}^*(z^*_1,\cdots,z^*_6,s), \tag{2.95}$$

$$= \sum_{k=1}^{6}\mathcal{J}^*_k z^*_k, \tag{2.96}$$

where z_i is the i-th component of $\boldsymbol{z}(s)$ and in the last equation we defined a set of functions,

$$\mathcal{J}^*_k(s) := \mathcal{J}^*(0,\cdots,0,1,0,\cdots,0,s)\ (k=1,\cdots,6), \tag{2.97}$$

where the arguments of $\mathcal{J}^*(\cdots)$ on the right hand side are set to be zero except for the k-th one, which is put to unity. Since $\mathcal{L}[\delta(t)]=1$, $\mathcal{J}_k(t)=\mathcal{L}^{-1}[\mathcal{J}^*_k]$ describes $\delta r_{\rm sh}/r_{\rm sh}$ for the impulsive perturbation of the unit strength, i.e., $\delta(t)$, added only to the k-th component of $\boldsymbol{z}(t)$. This implies that $\mathcal{J}_k(t)$ can be regarded as a Green's function. Eq. (2.93) is also written as

$$\left(\frac{\delta r^*_{\rm sh}}{r_{\rm sh}}\right)_{\rm IB} = \frac{-b^*(s)}{\boldsymbol{a}^*\cdot\tilde{\Lambda}^*(s)(s\boldsymbol{c}+\boldsymbol{d})} \tag{2.98}$$

$$=: \mathcal{S}^*(b^*,s)=\mathcal{S}^*(1,s)b^*(s). \tag{2.99}$$

Corresponding to the decomposition of $\delta r^*_{\rm sh}/r_{\rm sh}$, Eq. (2.90), its residue can be also divided into three parts:

$$|a_k| = \left|\sum_{j=1}^{6}\operatorname*{Res}_{s=\Omega_k+i\omega_k}[z^*_j(s)\mathcal{J}^*_j(s)] + \operatorname*{Res}_{s=\Omega_k+i\omega_k}\left[\left(\frac{\delta r_{\rm rm}}{r_{\rm sh}}\right)_{\rm ini}\right] + \operatorname*{Res}_{s=\Omega_k+i\omega_k}[\mathcal{S}^*(1,s)b^*(s)]\right|. \tag{2.100}$$

The first and third terms on the right hand side of the above equation are calculated as

$$\sum_{j=1}^{6}\operatorname*{Res}_{s=\Omega_k+i\omega_k}[z^*_j(s)\mathcal{J}^*_j(s)] = \sum_{j=1}^{6} z^*_j(\Omega_k+i\omega_k)\operatorname*{Res}_{s=\Omega_k+i\omega_k}\mathcal{J}^*_j(s), \tag{2.101}$$

$$\operatorname*{Res}_{s=\Omega_k+i\omega_k}[\mathcal{S}^*(1,s)b^*(s)] = b^*(\Omega_k+i\omega_k)\operatorname*{Res}_{s=\Omega_k+i\omega_k}[\mathcal{S}^*(1,s)], \tag{2.102}$$

here we assume $\boldsymbol{z}^*(s)$ and $b^*(s)$ do not have a pole at $s=\Omega_k+i\omega_k$. From the above expressions, the contribution from the upstream perturbations and inner boundary fluctuations can be obtained for any $\boldsymbol{z}(t)$ and $b(t)$ once we derive the residues of $\mathcal{J}^*_j(s)$ $(j=1,\cdots,6)$ and $\mathcal{S}(1,s)$.

2.2 Instabilities of the standing shock

2.2.1 Injection of acoustic waves and perturbations of neutrino luminosity

I analyze effects of the injection of acoustic waves from the inner boundary as well as of the fluctuations of the neutrino luminosity. I introduce the former as a time-dependent inner boundary condition. In considering the latter, on the other hand, I introduce the fluctuation of neutrino temperature as a new degree of freedom and impose an additional inner boundary condition.

In the following, I give the details of the numerical treatments of these two ingredients in turn. Table 2.2 is a concise summary of the three models considered in this section.

Injection of acoustic waves

According to the general solution of the linearized equations (see Eqs. (2.85) and (2.86) in section 2.1.6), the positions of poles in the complex plane are affected directly by the inner boundary condition through the coefficient $\boldsymbol{a}^*(s)$ in Eq. (2.52). This is in sharp contrast to the outer boundary condition, which has only an indirect leverage. It is hence important to give an appropriate condition at the inner boundary.

It should be noted that the acoustic mode has been already taken into account in the linearized equations. This is understood as follows. The propagation speeds of eigenmodes are the eigenvalues of the matrix V in the linearized equations written as

$$\frac{\partial \boldsymbol{y}}{\partial t} + V\frac{\partial \boldsymbol{y}}{\partial r} + A^{-1}B\boldsymbol{y} = 0. \tag{2.103}$$

They are actually v_r, $v_r - c_s$, $v_r + c_s$, where c_s is the sound speed. Whereas v_r is quadruply degenerate with the corresponding eigenmodes being $\delta v_\perp$, $\delta v_{\rm rot}$, δY_e, $P/(\rho)^2\delta\rho - \delta\varepsilon$, $v_r - c_s$ and $v_r + c_s$ correspond, respectively, to the ingoing and outgoing acoustic modes, which have the eigenvectors expressed as

$$\begin{aligned} y_{\rm in} &= \frac{1}{{c_s}^2}\left(\frac{\partial P}{\partial \rho}\right)\frac{\delta\rho}{\rho} - \frac{v_r}{c_s}\frac{\delta v_r}{v_r} + \frac{\varepsilon}{{c_s}^2\rho}\left(\frac{\partial P}{\partial \varepsilon}\right)\frac{\delta\varepsilon}{\varepsilon} + \frac{Y_e}{{c_s}^2\rho}\left(\frac{\partial P}{\partial Y_e}\right)\frac{\delta Y_e}{Y_e} \\ &= \frac{1}{{c_s}^2\rho}\delta P - \frac{v_r}{c_s}\frac{\delta v_r}{v_r}, \end{aligned} \tag{2.104}$$

$$y_{\rm out} = \frac{1}{{c_s}^2\rho}\delta P + \frac{v_r}{c_s}\frac{\delta v_r}{v_r}. \tag{2.105}$$

Based on this observation, I impose the following condition at the inner boundary to inject the acoustic waves, which may be produced by the g-mode oscillation of PNS:

$$y_{\rm out}(r_{\nu_e}, t) = \alpha \sin\left(\omega_{\rm PNS} t\right), \tag{2.106}$$

where the amplitude α is a free parameter, which I set to 1. Laplace-transformed, the right hand side of the above equation gives $b^*(s)$ in Eq. (2.52). As can be seen from the general solution (2.86) of the linearized equations, $b^*(s)$ does not affect the pole positions of $\delta r^*_{\rm sh}/r_{\rm sh}(s)$, or the stability of shock wave. As for $\omega_{\rm PNS}$ in Eq. (2.106), I employ the typical g-mode frequency of PNS:

$$\omega_{\rm PNS} = 2000 \times l \ {\rm s}^{-1} \tag{2.107}$$

(Burrows et al. (2006)). Note in passing that in no injection model, we imposed the following inner boundary condition:

$$\delta v_r = 0, \tag{2.108}$$

which is same as previous research (Takahashi et al. (2016)).

Table 2.2: Comparison of three models in this study

Models	Acoustic injection	Perturbations of neutrino luminosity	Basic equation	Outer boundary condition	Degree of freedom(s) after imposing outer boundary condition	Inner boundary condition(s)
A	no	no	(2.49)	(2.50)	$\delta r^*_{\rm sh}/r_{\rm sh}$	(2.108)
B	yes	no	(2.49)	(2.50)	$\delta r^*_{\rm sh}/r_{\rm sh}$	(2.106)
C	yes	yes	(2.76)	(2.50)	$\delta r^*_{\rm sh}/r_{\rm sh}$ and $\delta T^*_\alpha/T_\alpha$	(2.106) and (2.109)

Inner boundary condition for fluctuations of the neutrino luminosity

We assume that the fluctuations of neutrino temperature are related with the perturbation to Y_e in the vicinity of the neutrino sphere. Indeed for each (l, m) with $l > 1$, we impose the following relation:

$$\left(\frac{\partial P}{\partial Y_e}\right)_{\rho,T} \delta Y_e^{(l,m)}(r_{\nu_e}, t) + \left(\frac{\partial P}{\partial T}\right)_{\rho,Y_e} \delta T_\alpha^{(l,m)}(t) = 0. \tag{2.109}$$

This means that δT_α is equal to the perturbation to the matter temperature that could cancel the pressure fluctuation that the Y_e perturbation would induce which relation is found in numerical simulation (Janka et al. (2016)). We further assume that there is no spherically symmetric ($l = 0$) perturbation to the neutrino temperature.

2.2.2 Instabilities of the standing shock

I first present the growth rates as well as the oscillation frequencies of the dominant modes for models A, B and C as a function of the neutrino luminosity. They are read out from the positions of the corresponding poles of $\delta r^*_{\rm sh}/r_{\rm sh}(s)$. Note that there are several poles for a given luminosity in fact. Figure 2.1 shows the several poles (or growth rate and frequencies) for a given luminosity in model A. As can be seen, the higher overtones sometimes take over the position of the maximum-growth-rate mode (see figures of $l = 2,\ 3$).

In Figure 2.2 I plot the results for $l = 1$ for three models listed in Table 2.2. The black, red and blue lines correspond to models A, B and C, respectively. Figure 2.3 gives the same results as Figure 2.2 but for higher l modes.

We first look at the effect of the acoustic injection. From a comparison of the different models in Figure 2.2 (a), the growth rate of the dominant mode with $l = 1$ is enhanced by the acoustic power injection especially when the neutrino luminosity is low $L_\nu \lesssim 4.0 \times 10^{52}$ erg s^{-1}. This enhancement is accompanied by the lowering of the critical luminosity from $L_\nu \sim 2.8 \times 10^{52}$ erg s^{-1} to $L_\nu \sim 2.5 \times 10^{52}$ erg s^{-1}. By the critical luminosity I mean here the lowest luminosity, at which this particular mode becomes unstable. At high neutrino luminosities $L_\nu \gtrsim 4.5 \times 10^{52}$ erg s^{-1} the acoustic power does not affect the growth rates very much. Note that the oscillation frequency vanishes at $L_\nu \gtrsim 5.5 \times 10^{52}$ erg s^{-1}. This may be interpreted as the transition from the SASI regime to the convection regime. Then we may say that the acoustic injection does not play an important role in the convective instability in the linear order.

It is not the $l = 1$ mode but $l = 2$ and 3 modes that have the greatest growth rate at low neutrino luminosities. As we can see from Figure 2.3 (a) and (c), this is due to the strong enhancements of the growth rates in $l = 2$ mode at $L_\nu \lesssim 4.0 \times 10^{52}$ erg s^{-1}. The critical luminosities for these modes are also significantly reduced. These results indicate that quadrupole and octupole radiations of acoustic wave from PNS may strongly enhance the instability of the same anisotropies.

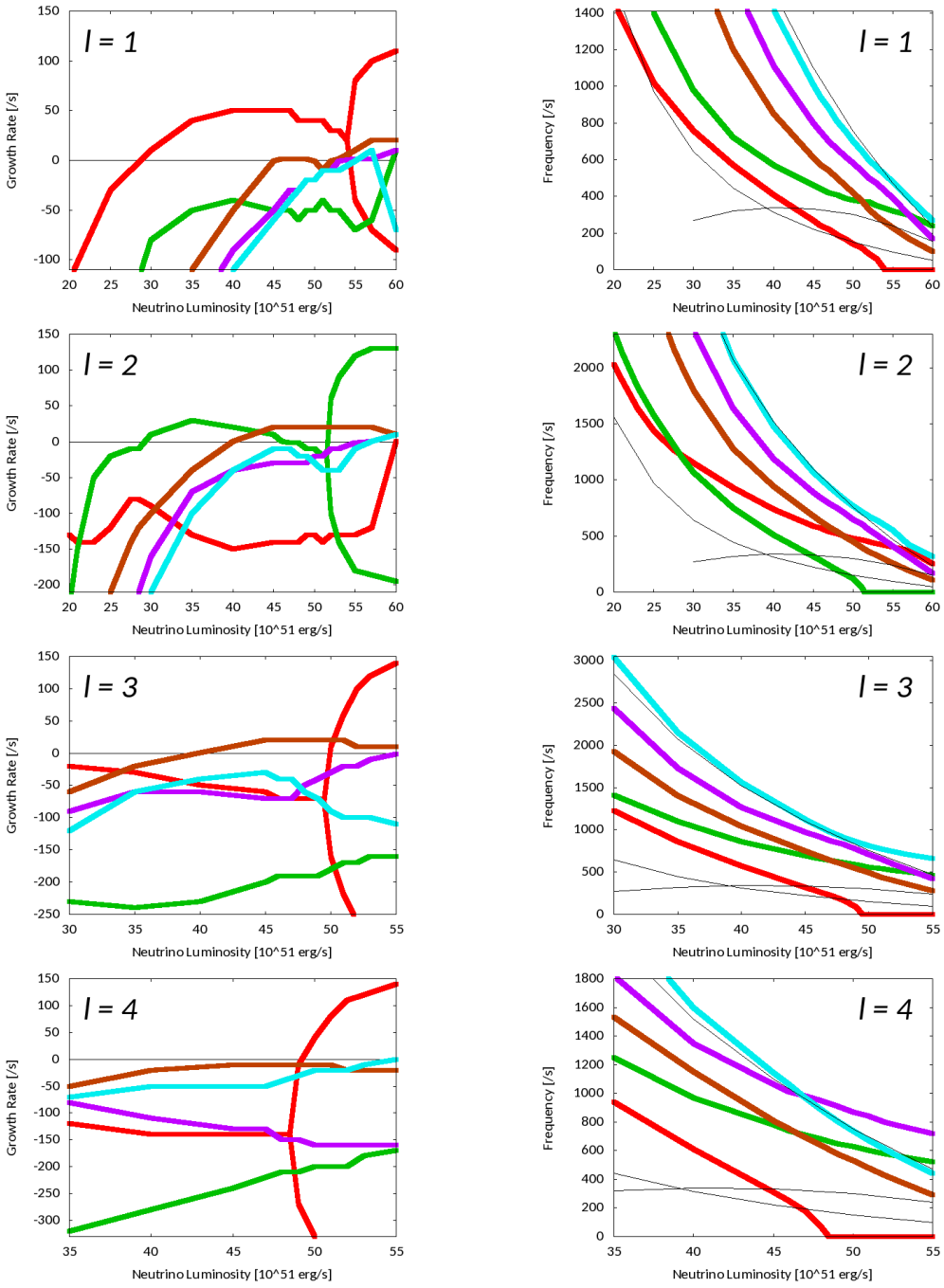

Figure 2.1: Plots of eigenmodes as functions of neutrino luminosity for $l = 1, 2, 3, 4$ in model A. Left: growth rate of the fundamental mode (red lines) and higher overtones (green, brown, purple, and light-blue for 1st, 2nd, 3rd and 4th overtones, respectively). Right: corresponding oscillation frequencies. Colors have the same meanings. (Figure citation from Takahashi et al. (2016) through the courtesy of Kazuya Takahashi)

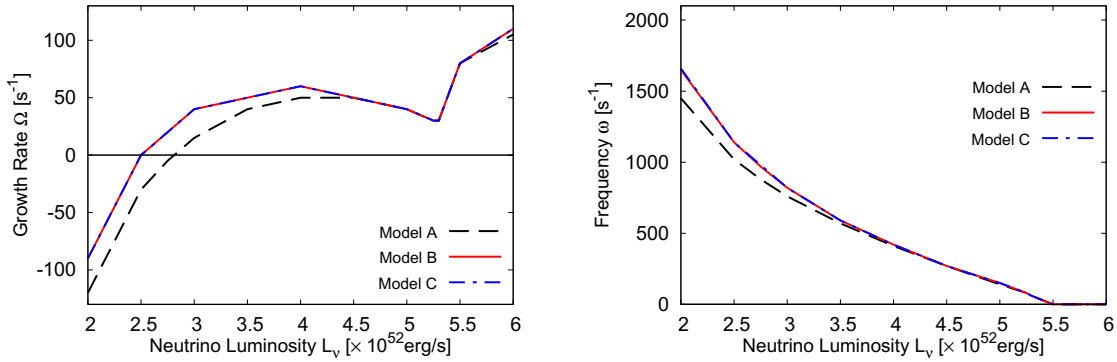

(a) Growth rates ($l = 1$)

(b) Frequencies ($l = 1$)

Figure 2.2: The growth rates (a) and oscillation frequencies (b) of the dominant eigenmodes for three models as a function of the neutrino luminosity L_ν. Black dashed, red solid and blue dash-dotted lines show the results of models A, B and C, respectively.

For $l \geq 4$ modes, the modifications of the inner boundary condition do not have much influence on the shock instability. As an example, the $l = 4$ case is shown in panels (e) and (f) of the same figure. The growth rates of the three eigenmodes decrease monotonically in a similar way as the neutrino luminosity gets smaller and the critical luminosity is not changed much either. This situation is common to other high l modes.

Compared with the growth rates, the oscillation frequencies are less affected by the modifications of the inner boundary conditions as is evident from the right panels in Figures 2.2 and 2.3. This may be because the eigenfrequency of the shock is simply determined by the global structure of the background flow below the shock wave.

There appear humps around $L_\nu \sim 4.0 - 4.5 \times 10^{52}$ erg s^{-1} in panels (b) and (d) in Figure 2.3. This happens because the second overtones take over the position of the maximum-growth-rate mode (see Figure 2.1 for such behavior).

Finally the comparison of models B and C in Figures 2.2 and 2.3 shows that the perturbation of neutrino luminosity changes neither the growth rates nor the oscillation frequencies appreciably. This is common to all the modes studied here and suggests that the fluctuations of neutrino luminosity may not be important for the shock instability in the linear order.

2.2.3 Instigations of various modes

Various modes, stable and unstable alike, are excited by the perturbations propagated from the inner boundary, at which we impose the time-dependent conditions. We hence need not set a non-vanishing perturbation initially. How strongly they are instigated is different from mode to mode and given by the amplitude a_j of Eq. (2.53), which can be obtained by calculating the residue of $\delta r^*_{\rm sh}/r_{\rm sh}(s)$ as explained in section 2.1.7.

Figure 2.4 shows the absolute values of the amplitudes for the dominant unstable eigenmodes with $l = 1, 2, 3$ and 4 in the spherical harmonics expansion. Dash-dotted lines and squares correspond to model A, solid lines and crosses mean model B and dashes lines and circles represent model C. Colors indicate the different neutrino luminosities.

Comparing the results for models A and B, one finds that the injection of the acoustic power magnifies the amplitudes in general and that the amplification is remarkable when the neutrino luminosity is low. In fact, the enhancement is as high as a few orders of

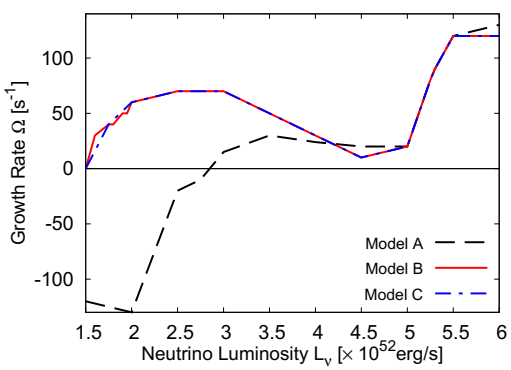

(a) Growth rates ($l = 2$)

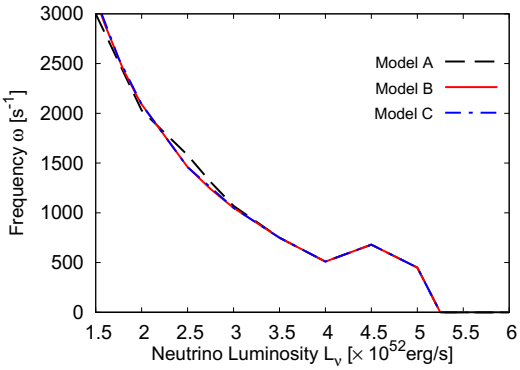

(b) Frequencies ($l = 2$)

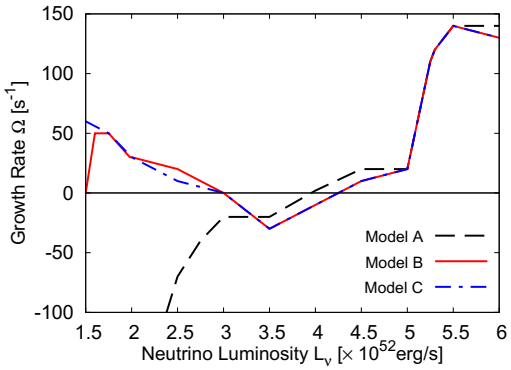

(c) Growth rates ($l = 3$)

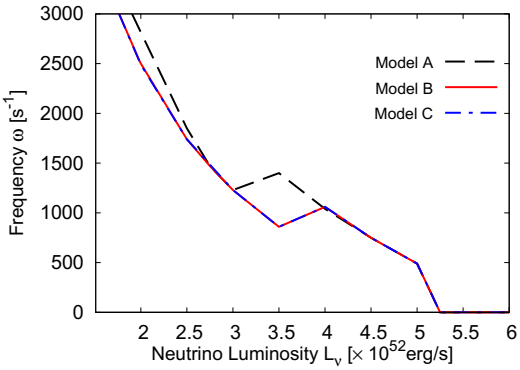

(d) Frequencies ($l = 3$)

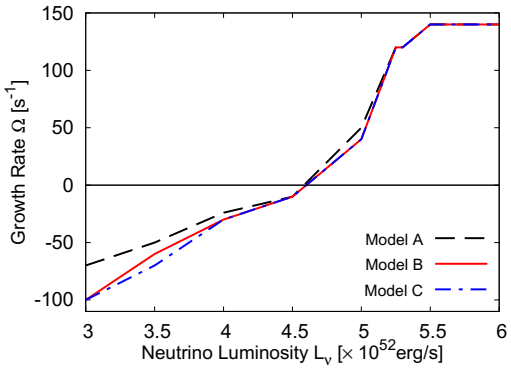

(e) Growth rates ($l = 4$)

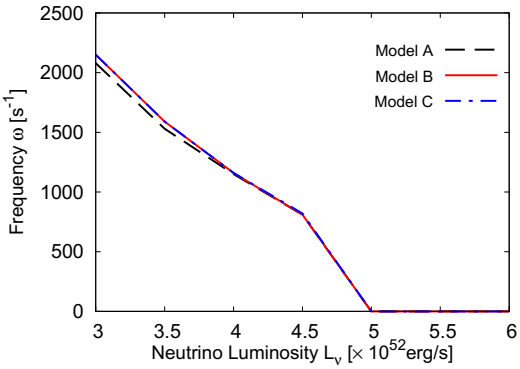

(f) Frequencies ($l = 4$)

Figure 2.3: Same figures as Figure 2.2 but for higher l modes

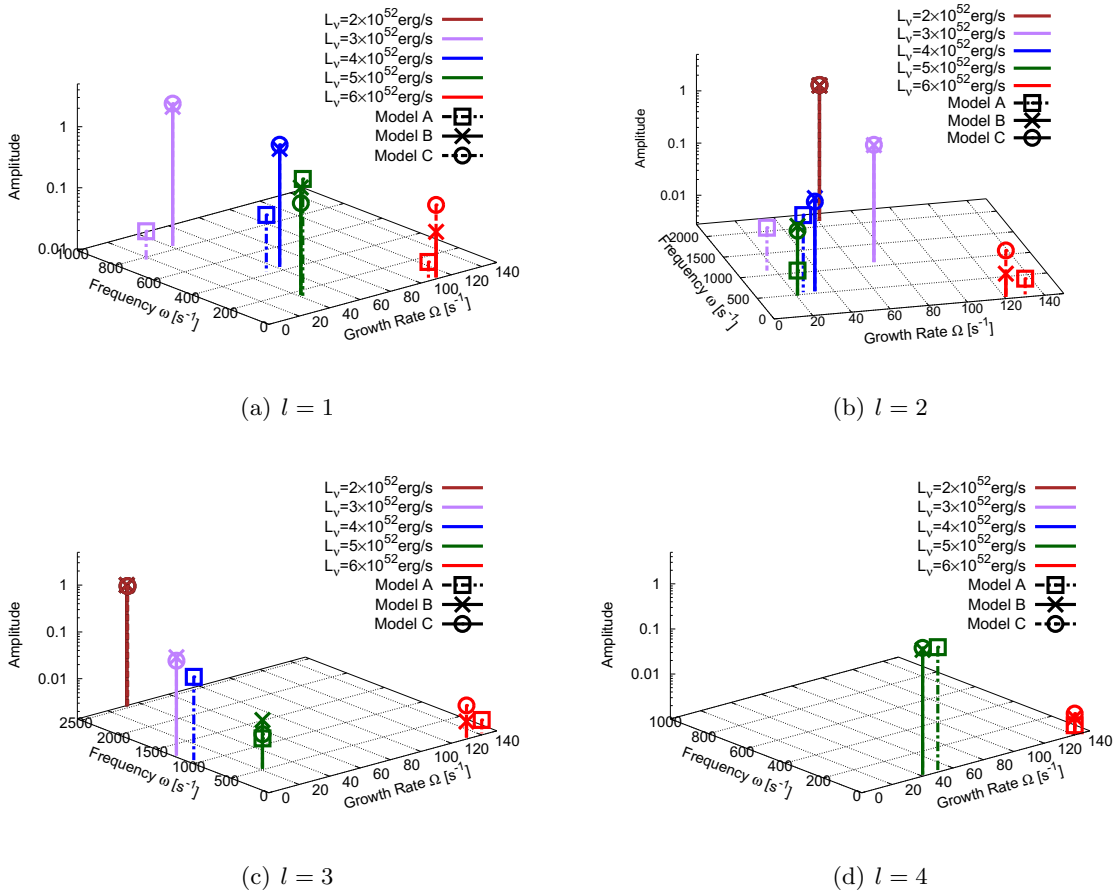

(a) $l = 1$ (b) $l = 2$

(c) $l = 3$ (d) $l = 4$

Figure 2.4: Amplitudes of unstable eigenmodes for different boundary conditions, luminosities and spherical harmonics modes. Dash-dotted lines and squares correspond to model A, solid lines and crosses mean model B and dashed lines and circles represent model C. Colors indicate the different neutrino luminosities.

magnitude at low luminosities whereas it is just a factor of a few at high luminosities. It is also evident that the enhancement is more remarkable for $l = 1$ and 2 modes. The suppression of the enhancement at high luminosities is due to the mismatch between the frequencies of g-modes in PNS and those of SASI and convection. This will be explained more in detail later.

The comparison of models B and C in Figure 2.4 shows, on the other hand, that the excitation of modes is little affected by the perturbation of neutrino luminosity. This is consistent with the previous findings on the growth rate and oscillation frequency and suggests that the temporal fluctuation of the neutrino luminosity is not very important for the shock instability at least in the linear order.

As we mentioned earlier, the amplification of the mode amplitudes by the acoustic power injection becomes more remarkable as the neutrino luminosity gets lower. We discuss this trend from the view point of the resonance between SASI and PNS g-modes. Let us omit the perturbation to the neutrino luminosity, that is, we assume $\tilde{\boldsymbol{L}}(s) = 0$, $\boldsymbol{w} = 0$ and $\delta T_\alpha = 0$ in equation (2.85) for simplicity. As I explained in section 2.1.7, the amplitude of the Laplace-transformed shock perturbation is expressed as Eq. 2.90 and the

contribution from the inner boundary to the amplitude is written as

$$\left(\frac{\delta r^*_{\rm sh}}{r_{\rm sh}}\right)_{\rm IB} := \frac{-b^*(s)}{\boldsymbol{a}^* \cdot \tilde{\Lambda}^*(s)(s\boldsymbol{c}+\boldsymbol{d})}. \tag{2.110}$$

The amplitude of an eigenmode is proportional to $b^*(s)$ at the pole corresponding to this mode. In the acoustic injection model considered here, $b(t)$ is assumed to be monochromatic and given as

$$b(t) = \sin\left(\omega_{\rm PNS} t\right), \tag{2.111}$$

(see Eq. (2.106)) and its Laplace transform is then obtained as

$$b^*(s) = \frac{\omega_{\rm PNS}}{s^2 + {\omega_{\rm PNS}}^2}. \tag{2.112}$$

The amplitude of eigenmode is hence proportional to

$$b^*(s = \Omega + i\omega) = \frac{\omega_{\rm PNS}}{(\Omega + i\omega)^2 + {\omega_{\rm PNS}}^2}, \tag{2.113}$$

and the maximum value of $|b^*|$ is given at $\omega = \sqrt{\omega^2_{\rm PNS} - \Omega^2}$ (see Figure 2.5). Considering the fact that $\Omega^2 \ll \omega^2_{\rm PNS}$ in the typical situation, in which $\omega_{\rm PNS} \gtrsim 1000$ s^{-1} (see, for example, Burrows et al. (2006)) and $\omega \sim 100$ s^{-1} (see Figure 2.2), this is essentially $\omega \sim \omega_{\rm PNS}$ which means that the oscillation of the unstable mode should be resonant with one of the g-mode oscillations. Such a situation is approached as the neutrino luminosity is lowered, since the shock radius is decreased and, as a result, the SASI frequency is increased (see Figure 2.5). This is essentially true irrespective of the value of l as can be seen in the right panels of Figure 2.3.

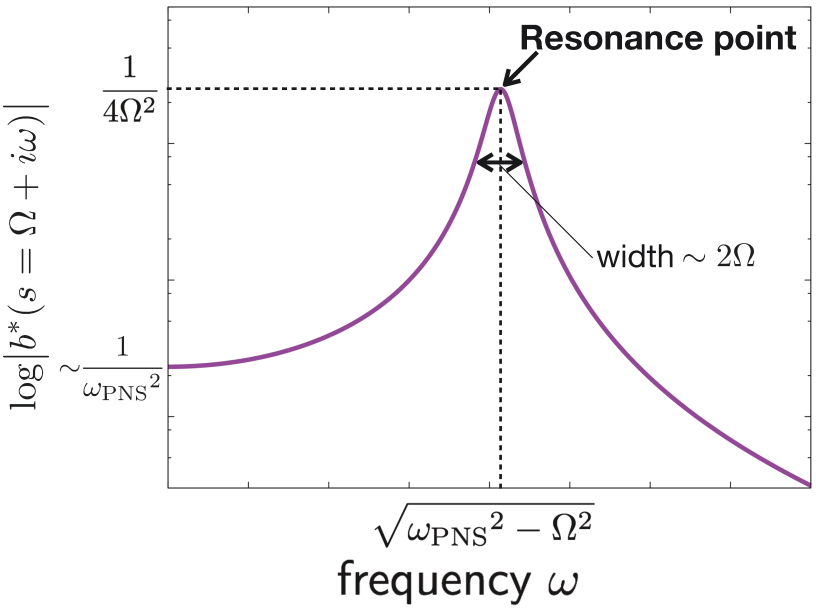

Figure 2.5: $\log|b^*(s = \Omega + i\omega)|$ as a function of ω. The maximum value of $|b^*|$ is obtained at $\omega = \sqrt{\omega^2_{\rm PNS} - \Omega^2}$ where the acoustic wave produced by the g-mode oscillation of the PNS becomes resonant with the SASI oscillation.

2.3 Steady perturbed state

We now shift our attention to time-independent solutions of the perturbation equations. This is motivated by the finding first reported by Tamborra et al. (2014a) that there occurs a shock deformation accompanied by an anisotropy in the number flux difference $F^n_{\nu_e} - F^n_{\bar{\nu}_e}$ of the electron-type neutrinos. The structure is robust, being sustained for a long time. They called it LESA (see section 1.2.3). Dolence et al. (2015) later reported that they found a dipolar asymmetry not in the difference but in the sum of the two fluxes $F_{\nu_e} + F_{\bar{\nu}_e}$ (and also the sum of number fluxes) is strongly correlated with the deformation of the shock front. Regardless of the apparent discrepancy, these structures are supposed to be sustained by the combination of the shock deformation and the asymmetric neutrino emissions and may be produced even at the linear level. This is what we are going to investigate in this section.

2.3.1 Steady perturbed equation and inner boundary conditions

I modify the basic equations as follows. First the expressions for the fluctuations in the neutrino luminosities is extended as

$$\frac{\delta L_{\nu_e}}{L_0} = 4\frac{\delta T_{\nu_e}}{T_{\nu_e 0}} + c_{Y_e}\frac{\delta Y_e}{Y_{e0}}, \tag{2.114}$$

$$\frac{\delta L_{\bar{\nu}_e}}{L_0} = 4\frac{\delta T_{\bar{\nu}_e}}{T_{\bar{\nu}_e 0}} - c_{Y_e}\frac{\delta Y_e}{Y_{e0}}, \tag{2.115}$$

where c_{Y_e} is a constant parameter that accounts for the possible correlation between the fluctuation in the neutrino luminosity and that in Y_e (Janka et al. (2016)). I investigated two cases with $c_{Y_e} = 0$ and $c_{Y_e} = 3.5$. The latter value is taken from the numerical simulation of core-collapse supernova in 2D by Nagakura et al. (2018) with Furusawa EoS (Furusawa et al. (2013)). Since in the light-bulb approximation the fluctuations of neutrino luminosities can be also expressed as (see Eq. 2.5)

$$\frac{\delta L_\alpha}{L_0} = 4\frac{\delta T_\alpha}{T_{\alpha 0}} + 2\frac{\delta r_\alpha}{r_{\alpha 0}}, \tag{2.116}$$

with $\alpha = \nu_e, \bar{\nu}_e$, we obtain the perturbations to the neutrino spheres as follows:

$$\frac{\delta r_{\nu_e}}{r_{\nu_e 0}} = +\frac{c_{Y_e}}{2}\frac{\delta Y_e}{Y_{e0}}, \tag{2.117}$$

$$\frac{\delta r_{\bar{\nu}_e}}{r_{\bar{\nu}_e 0}} = -\frac{c_{Y_e}}{2}\frac{\delta Y_e}{Y_{e0}}. \tag{2.118}$$

I use these expressions just for numerical convenience. Note also that we assume

$$\frac{\delta T_\alpha}{T_{\alpha 0}} = \frac{\delta T}{T_0}, \tag{2.119}$$

that is, the fluctuations of the neutrino temperatures are equal to that of matter temperature at the neutrino sphere.

This extension gives the new terms in neutrino reaction rate and heating rate. Instead of using the expression in Eq. (2.72), we have to include fluctuations of the radius of the neutrino sphere:

$$\begin{aligned}\delta f_\alpha(\boldsymbol{x}, \epsilon) &= \frac{\partial f_\alpha(\boldsymbol{x}, \epsilon)}{\partial T_\alpha}\delta T_\alpha + \frac{\partial f_\alpha(\boldsymbol{x}, \epsilon)}{\partial r_\alpha}\delta r_\alpha \\ &= \frac{\beta_\alpha \epsilon \mathrm{e}^{\beta_\alpha \epsilon}}{\left(1 + \mathrm{e}^{\beta_\alpha \epsilon}\right)^2} g(|\boldsymbol{x}|)\frac{\delta T_\alpha}{T_\alpha} + \frac{1}{2}\frac{1}{1 + \mathrm{e}^{\beta_\alpha \epsilon}}\frac{(r_\alpha/r)^2}{\sqrt{1 - (r_\alpha/r)^2}}\frac{\delta r_\alpha}{r_\alpha},\end{aligned} \tag{2.120}$$

where the second term in the last equation is new term in this section.

I impose the inner boundary conditions as follows. For simplicity, $\delta T_\alpha/T_{\alpha 0}$ is normalized as unity. Then, $\delta r_{\rm sh}/r_{\rm sh}$ and $\delta r_{\nu_e}/r_{\nu_e}$ are the remaining variables after imposing outer boundary condition, and are determined by

$$1 = \frac{\delta T_\alpha}{T_{\alpha 0}} = \frac{\delta T}{T_0} = \frac{1}{T}\left\{\frac{\partial T}{\partial \rho}\delta\rho + \frac{\partial T}{\partial Y_e}\delta Y_e + \frac{\partial T}{\partial \varepsilon}\delta\varepsilon\right\}, \tag{2.121}$$

$$\frac{\delta r_{\nu_e}}{r_{\nu_e}} = \frac{c_{Y_e}}{2}\left.\frac{\delta Y_e}{Y_e}\right|_{\rm PNS}, \tag{2.122}$$

where $\delta r_{\rm sh}/r_{\rm sh}$ is implicitly determined by Eq. (2.121).

Steady solution of perturbation equations satisfies

$$\frac{\partial \boldsymbol{y}}{\partial r} = B^{(l)}\boldsymbol{y} + \boldsymbol{u}\frac{\delta T_\alpha}{T_\alpha}. \tag{2.123}$$

It is important to recognize that steady solutions of the linearized equations in the temporal regime correspond to the nontrivial solution at $s = 0$ of the Laplace-transformed equations (2.76). Since in this section we neglect both the acoustic injection from the inner boundary and the perturbation ahead of the shock front, such solution represent self-sustained nonspherical configurations, something corresponding to LESA at the linear perturbation level. Note that the existence of such solutions is itself highly non-trivial.

2.3.2 Self-sustained steady configuration

It turns out that there are steady solutions indeed even for $c_{Y_e} = 0$. As a typical case, I give the results for the model with $L_\nu = 3.0 \times 10^{52}$ erg s^{-1} in the left half of Table 2.3 and also as dashed lines in Figure 2.6. I consider only $l = 1$ modes here. Since I set $c_{Y_e} = 0$, there is no difference in the fluctuation in the luminosity between ν_e and $\bar{\nu}_e$:

$$\delta L_{\nu_e} = \delta L_{\bar{\nu}_e}. \tag{2.124}$$

As represented in Table 2.3, the deformation of the shock front $\delta r_{\rm sh}/r_{\rm sh}$ is correlated with the temperature fluctuation at the neutrino sphere, having the same sign. This is consistent with the finding by Dolence et al. (2015) although we cannot say anything about LESA in this case as there is no asymmetry in δL_{ν_e} and $\delta L_{\bar{\nu}_e}$ by definition. It is noteworthy, however, that $\delta Y_e/Y_{e0}$ has the same signature as $\delta T/T_0$ on the PNS surface (see the purple and blue dashed lines in Figure 2.6).

Next we consider the case with $\delta L_{\nu_e} - \delta L_{\bar{\nu}_e} \neq 0$, employing the models with $c_{Y_e} = 3.5$. The results are given in the right half of Table 2.3 and also as solid lines in Figure 2.6. I obtain non-trivial solutions also in this case. The configurations are not much different from these for the $c_{Y_e} = 0$ case with $\delta r_{\rm sh}/r_{\rm sh}$ being positively correlated with the temperature fluctuation. On the other hand, the perturbation to the electron fraction, $\delta Y_e/Y_{e0}$, has the opposite sign as $\delta T/T_0$ on the PNS surface (see the purple and blue solid lines in Figure 2.6). As a consequence of the latter fact, the neutrino luminosity difference $\delta L_{\nu_e} - \delta L_{\bar{\nu}_e}$ becomes negatively correlated with the shock deformation. I show the distributions of the velocity and the lepton number fluctuation in the meridional section in Figure 2.7. They are consistent with the schematic picture drawn by hand in Tamborra et al. (2014a) (see Figure 1.4): the dipolar deformation of the shock front bends stream lines and induces the asymmetry in the lepton number near the PNS surface, which is anti-correlated with the shock deformation, i.e., more lepton-rich matter accretes on the hemisphere, in which the shock recedes, resulting in positive δY_e there (see the color map in Figure 2.7 for $\delta(\rho Y_e)$).

Note that in drawing the velocity field, we add to the unperturbed flow the perturbation scaled arbitrarily.

Looking into these configurations more closely, we find that $|v_r|$ decreases in the direction, in which the shock front expand (see the yellow lines in Figure 2.6). This results in longer heating in the gain region and the temperature gets higher on this side. This then leads to larger luminosities on the same side. We also find that Y_e becomes smaller at the original shock position (see the purple line in Figure 2.6), since the shock expansion leads to an earlier turn-on of the electron capture. As the matter flows downward, δY_e increase owing to the lager neutrino luminosities just mentioned, which enhances the absorption of both ν_e and $\bar{\nu}_e$ with the former being dominant. The behavior of δY_e near the PNS surface is qualitatively different between the models with and without the correlation of the perturbation of the neutrino luminosity and that of Y_e. As a matter of fact, if we take it into account, adopting $c_{Y_e} = 3.5$, δY_e decreases rapidly and changes its sign. It is also observed that δY_e is initially smaller in this case than in the previous case with $c_{Y_e} = 0$. This is because $F_{\bar{\nu}_e} > F_{\nu_e}$ is established in the direction of the deformation of the shock expansion, which in turn is produced by the asymmetry of Y_e on the PNS surface mentioned above: Y_e is depleted on the same side. The decrease in δY_e and hence Y_e itself there is induced by the enhances absorption of $\bar{\nu}_e$. These explanations are admittedly tautological because it is difficult to tell the cause from the result in the steady state and all we can say is that the configuration is self-consistent. Incidentally, δY_e converges to the same value at $r \sim 40$km irrespective of the value of c_{Y_e}. This is a well-known feedback effect: the initial decrease of δY_e via the enhanced absorption is canceled by the suppression of electron capture later because of the smaller value of Y_e. It should be also mentioned that the very rapid change of δY_e near the inner boundary in the case of $c_{Y_e} = 3.5$ is an artifact of the geometric factor I employ in this study. In fact, the perturbation to λ (see Eq. (2.69)) is written as

$$\delta\lambda_\nu = \left(\frac{\partial\lambda_\nu}{\partial T_\alpha}\right)\delta T_\alpha + \left(\frac{\partial\lambda_\nu}{\partial Y_e}\right)\delta Y_e|_{\rm PNS}. \tag{2.125}$$

The second term on the right hand side is rewritten as

$$\left(\frac{\partial\lambda_\nu}{\partial Y_e}\right)\delta Y_e|_{\rm PNS} = \left(\frac{\partial\lambda_\nu}{\partial r_\nu}\right)\delta r_\nu \propto \frac{\partial g(r)}{\partial r_\nu} = \frac{1}{2}\frac{(r_\nu/r)^2}{\sqrt{1-(r_\nu/r)^2}},$$

in which the rightmost expression is a contribution from the derivative of the geometrical factor and is divergent at $r = r_\nu$. In reality, $\delta\lambda$ and hence δY_e should change more gradually.

The fact that the self-sustained steady states are obtained irrespective of the value of c_{Y_e} seems to suggest that the asymmetry of the lepton number flux is not essential for the build-up of such configurations but rather a structure associated with them. Indeed our results appear to indicate that it is the temperature fluctuation and the resultant perturbation to the sum of the fluxes of ν_e and $\bar{\nu}_e$, $F_{\nu_e}+F_{\bar{\nu}_e}$ rather than their difference that is the most important ingredients for the production of the self-sustained configurations (Dolence et al. (2015)). It is also true, however, that the asymmetries in the lepton fluxes and in the Y_e distribution are also self-sustained and are consistent with what Tamborra et al. (2014a) observed in their simulations. In this sense, our results are consistent with both of them in fact.

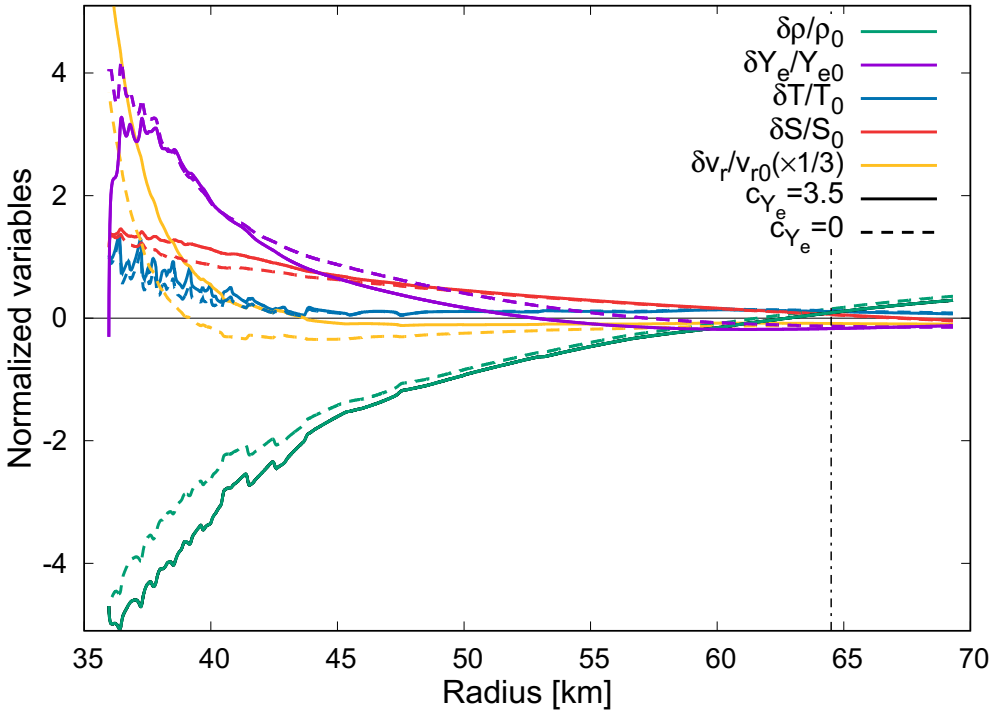

Figure 2.6: Radial distributions of various quantities in a steady perturbed solution. We set $L_\nu = 3.0 \times 10^{52}$ erg/s and $l = 1$ mode here. Dashed and solid lines correspond to the models for $c_{Y_e} = 0$ and 3.5, respectively. Vertical dash-dotted line indicates the gain radius.

Table 2.3: Steady perturbed solutions

Neutrino luminosity (erg s^{-1})	$c_{Y_e} = 0$			$c_{Y_e} = 3.5$		
	$\delta r_{\rm sh}/r_{\rm sh0}$	$\delta T_\nu/T_{\nu 0}$	$\delta r_{\nu_e}/r_{\nu_e 0}$	$\delta r_{\rm sh}/r_{\rm sh0}$	$\delta T_\nu/T_{\nu 0}$	$\delta r_{\nu_e}/r_{\nu_e 0}$
2×10^{52}	2.04×10^{-2}	1	0	7.66×10^{-3}	1	-0.650
3×10^{52}	1.86×10^{-1}	1	0	1.51×10^{-1}	1	-0.533
4×10^{52}	4.81×10^{-1}	1	0	4.43×10^{-1}	1	-0.421
5×10^{52}	1.63	1	0	1.60	1	-0.219

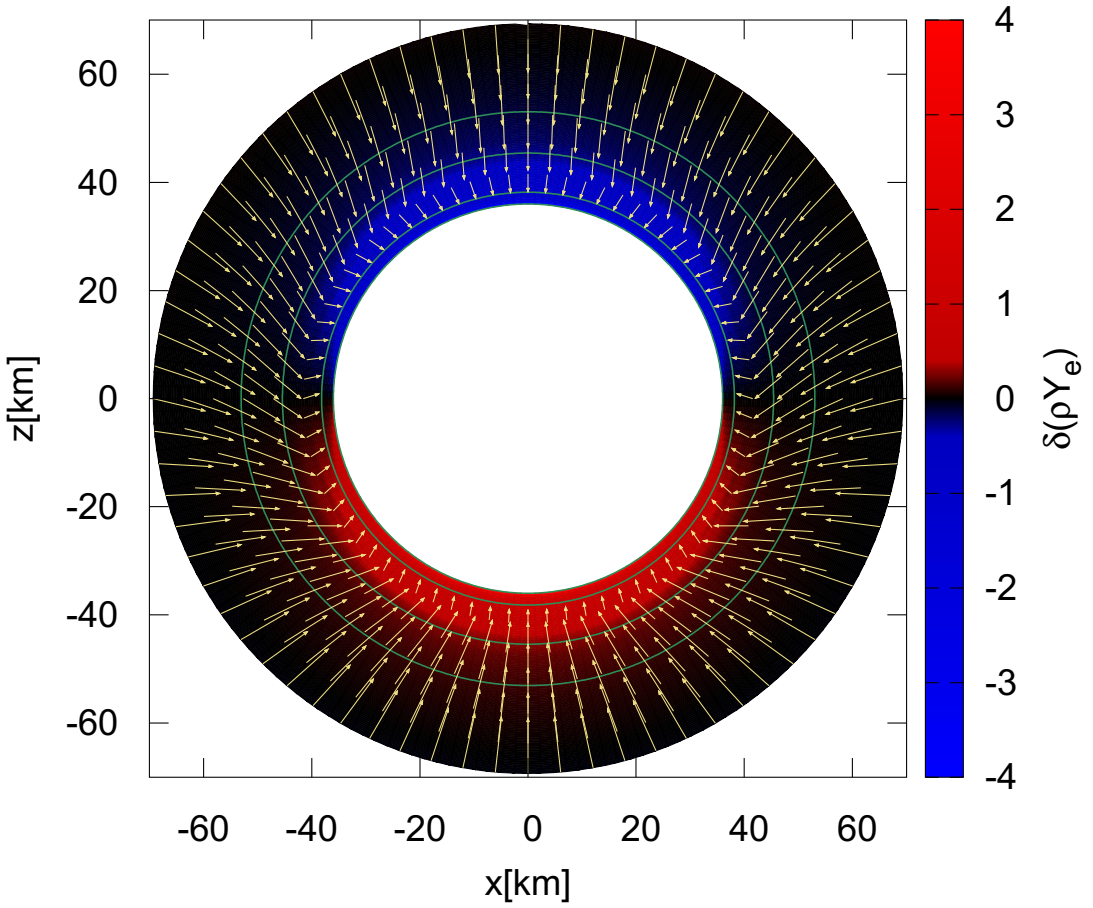

Figure 2.7: The distributions of velocity (arrows) and $\delta(\rho Y_e)$ (color map) in the meridional section for the model with $L_\nu = 3.0 \times 10^{52}$ erg/s. We set $l = 1$, $m = 0$ and $c_{Y_e} = 3.5$ here. The density contours are also shown for $\rho_0 = 0.5, 1, 5$ and 10×10^{10}g/cm^3. Note that the velocity perturbation is emphasized arbitrarily.

2.3.3 Effects of LESA on neutrino heating

As can be seen from the Table 2.3, the magnitudes of the shock deformation are smaller when the lepton number flux asymmetry exist. In both cases, the structures of perturbed states are similar except for $\delta Y_e/Y_e$ (see Figure 2.6); it rapidly decreases near the neutrino sphere in the case with $c_{Y_e} = 3.5$ and the neutrino emission reaction and cooling are enhanced. In fact, Figure 2.8 shows the fluctuations of net heating rate. Fluctuations of net heating rate is written as

$$\delta q = \delta q_{\rm th} + \delta q_\nu, \tag{2.126}$$

where

$$\begin{aligned}\delta q_{\rm th} &= \frac{\partial q}{\partial \rho}\delta\rho + \frac{\partial q}{\partial \varepsilon}\delta\varepsilon + \frac{\partial q}{\partial Y_e}\delta Y_e \\ &=: \delta q_\rho + \delta q_\varepsilon + \delta q_{Y_e}, \end{aligned} \tag{2.127}$$

$$\delta q_\nu = \frac{\partial q}{\partial T_\alpha}\delta T_\alpha + \frac{\partial q}{\partial r_\nu}\delta r_\nu. \tag{2.128}$$

Net heating rate q_0 of background steady flow is shown in Figure 2.8 (a), and fluctuations of net heating rate for $c_{Y_e} = 0$ and 3.5 are shown in Figure 2.8 (b). It is clear that cooling rate near the PNS surface is stronger for the case with $c_{Y_e} = 3.5$. Each term in equation (2.126) are also shown in Figure 2.8 (b) and both terms decrease because of lepton number flux asymmetry. The decrease of latter term δq_ν is simply because δr_ν is negative.

The variation of each term in equation (2.127) is shown in Figure 2.8 (c). By lepton number flux asymmetry, δq_ρ increases but δq_{Y_e} decreases. This is because $\partial q/\partial\rho$ and $\partial q/\partial\varepsilon$ are negative and δq decreases and $\delta\varepsilon$ increases. $\delta q_{\rm th}$ becomes negative as a result of taking total of these terms. In fact, in $e^\pm$ dominated case, net heating rate can be approximately written as

$$q \sim \frac{L_\nu \sigma}{4\pi r_\nu} - \sigma v_{e^\pm} n_{e^\pm} \langle \epsilon_\nu \rangle \tag{2.129}$$

$$\sim \frac{L_\nu \sigma}{4\pi r_\nu} - Ac(3k_B T)^3 n_{e^\pm}, \tag{2.130}$$

here we use cross section $\sigma \sim A\langle\epsilon_\nu\rangle^2$ (A is a constant) and $\langle\epsilon_\nu\rangle \sim 3k_BT$. Since $\rho \propto n_{e^\pm}$ and $\varepsilon \propto T$, $\partial q/\partial\rho$ and $\partial q/\partial\varepsilon$ become negative. Approximation of $e^\pm$ dominance is justified because $\mu_e/T \ll 1$ is satisfied around $r \sim 4 - 4.5 \times 10^6$km.

2.4 Summary

I have investigated the instability of the standing shock wave and the accretion flows downstream in the core of CCSNe by linear analysis. I have focused particularly on the influences of the fluctuations at the inner boundary. As possible sources of such fluctuations, we have considered the injection of acoustic powers and the perturbation of the neutrino luminosity. I have linearized hydrodynamics equations and solved them by Laplace transform, regarding them as an initial-boundary-value problem. As for the unperturbed state, we employ spherically symmetric, steady shocked accretion flows. In this formulation, the intrinsic eigenmodes such as SASI or convection are obtained as pole singularities of the Laplace-transformed equations and how strongly these modes are excited by the perturbations imposed at the boundaries is given as the residues at the poles.

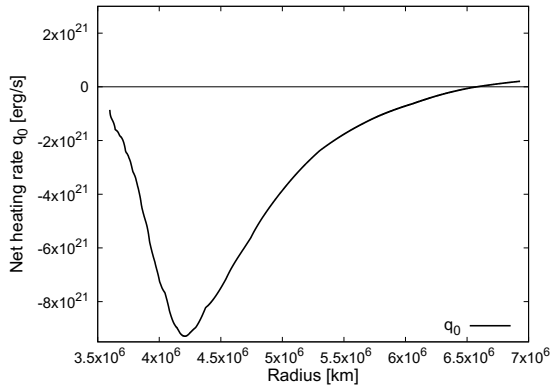

(a) Net heating rate of spherical background

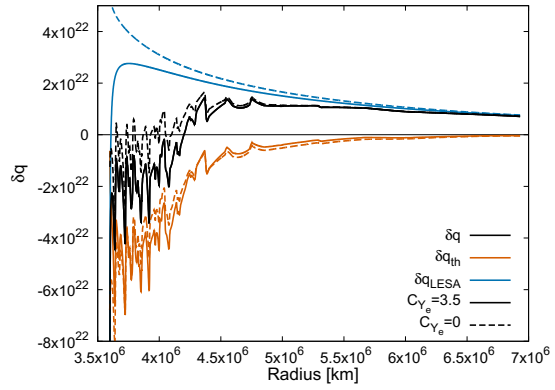

(b) Fluctuations of net heating rates $\delta q = \delta q_{\rm th} + \delta q_{\rm LESA}$

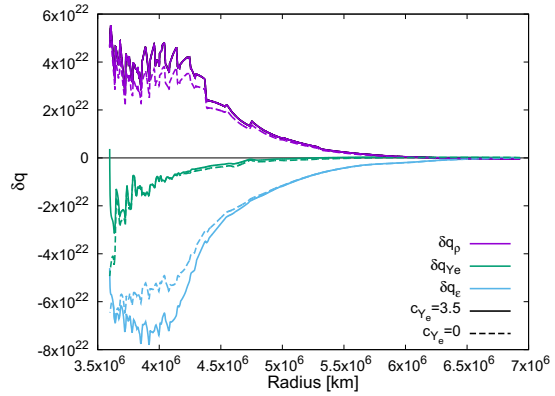

(c) Each component of $\delta q_{\rm th} = \delta q_\rho + \delta q_\varepsilon + \delta q_{Y_e}$

Figure 2.8: Net heating rates of spherical background (a) and fluctuations of the net heating rates (b) and (c). Model with neutrino luminosity $L_\nu = 3 \times 10^{53}$erg/s and $l = 1$ is plotted here.

I have first explored the influence of the injection of acoustic power from the PNS. Unlike the perturbation at the outer boundary, those at the inner boundary like this one change the growth rates and oscillation frequencies of eigenmodes directly. I have hence calculated them together with the excitation amplitudes for various neutrino luminosities. I have found that the acoustic power injection enhances the growth rates of the fluid instabilities in general and the critical luminosity, i.e., the lowest luminosity at which SASI occurs for some modes, is reduced. The enhancement is especially remarkable at low neutrino luminosities. This is because the mismatch between the g-mode oscillations of the PNS and the oscillations in the accretion flow is reduced. In fact, as the luminosity is lowered, the shock shrinks and, as a result, the latter frequency rises: since the g-mode frequency is normally higher than the frequency of the oscillations in the accretion flow, this means that the two frequencies get closer to each other. I have observed that the perturbation from the inner boundary excites some modes more preferentially than others as the perturbation from the outer boundary does but the excitation amplitudes are also enhanced by the injection of acoustic powers. On the other hand, the perturbations of the neutrino luminosities have been shown to have little effect on the growth rates and oscillation frequencies of eigenmodes as well as on their excitation amplitudes at least at the linear level.

I have then investigated steady perturbed solutions, being motivated by the LESA phenomenon (Tamborra et al. (2014a)). I have turned off the perturbations on the outer and inner boundaries except for those in the neutrino luminosities, which we assumed are induced by the fluctuation in temperature and/or Y_e, and studied if self-sustained configurations are obtained or not. I have found solutions indeed in both cases. It should be stressed that it is not a trivial thing. I have shown that the obtained structures are consistent with that proposed by Tamborra et al. (2014a). I also found that such self-sustained steady states are obtained without asymmetry between ν_e and $\bar{\nu}_e$ and it seems that it is the temperature fluctuation and the resultant perturbation to the sum of the fluxes of ν_e and $\bar{\nu}_e$, $F_{\nu_e} + F_{\bar{\nu}_e}$, rather than their difference that is the key to the production of these steady states. This seems consistent with the claim by Dolence et al. (2015). On the other hand, the asymmetries in the lepton emissions and in the Y_e distribution as Tamborra et al. (2014a) found them are also self-sustained although they may be a by-product. In this sense our results appear to be consistent also with their results.

Chapter 3

Muon-related neutrino interactions in PNS cooling phase

Understanding neutrino interactions in hot dense matter is indispensable not only to the investigation of the explosion mechanism of core-collapse supernovae (CCSNe), in which shock revival by neutrino heating is believed to be crucial, but also to the quantitative prediction of neutrino signals from newly born proto-neutron stars (PNS) formed by CCSNe. As a matter of fact, most of the gravitational binding energy of PNS is released in the form of neutrinos, with roughly a half of them being emitted in the explosion phase of CCSN and the remaining half being radiated in the cooling phase of PNS.

In the past, only electrons and positrons Ire incorporated as the charged-lepton constituents in most of the quantitative simulations of both CCSN and PNS cooling. That is because the muon and tauon have rest masses much larger than the typical temperature in the CCSN interior and their existence is supposed to be suppressed in the early explosion phase. Recently, the possible effects of the tiny population of muons on the supernova explosion as well as on the PNS cooling in the very early phase were investigated in supernova simulations as mentioned in chapter 1.

Observations of a long-term neutrino signal will provide us with invaluable information on the property of dense and hot nuclear matter (see Müller (2019) for a recent review). For example, the nuclear response to the weak current is modified at high densities via strong interactions among nucleons Sawyer (1995); Keil et al. (1995); Martínez-Pinedo et al. (2012). This is true not only for scatterings through the neutral current but also for emissions and absorptions of neutrinos via the charged-current. As a result, the cooling timescale is affected. The equation of state (EoS) of nuclear matter at very high densities is certainly another target for the observation of neutrinos into the late phase of the PNS cooling Sumiyoshi et al. (1995); Camelio et al. (2017); Nakazato and Suzuki (2019, 2020). In general, the softer the EoS is, the longer the cooling timescale becomes Nakazato and Suzuki (2019).

In this chapter, I calculate the rates of various muon-related neutrino reactions for some thermodynamical conditions that are typical at different times in the PNS cooling and evaluate its possible implications for the cooling timescale.

This chapter is organized as follows. I give the formulation for the rate calculations in the next section. In section 3.2, I exhibit the results, picking up a couple of specific thermodynamical conditions of relevance and discuss possible effects of the muon existence on the PNS cooling. I summarize our investigations in Section 3.3.

3.1 Weak interaction rates

I list the neutrino reactions considered in this thesis in Table 3.1, which are essentially the same as those in Bollig et al. (2017); Fischer et al. (2020). They are divided into two groups, i.e. the leptonic and semi-leptonic processes; in the latter nucleons are involved and the form factors are fully taken into account in their weak currents; small recoils of nucleons are also completely accounted for (see subsection 3.1.2 for more details). Having in mind the application to the collision term of the Boltzmann equation, which may be written as

$$\frac{1}{c}\left(\frac{df_\nu}{dt}\right)_{\rm coll} = -\frac{1}{\lambda_\nu} f_\nu + j_\nu(1-f_\nu), \tag{3.1}$$

where, λ_ν and j_ν are the mean free path and emissivity of neutrino, respectively, I will give their expressions for each reaction listed in Table 3.1 in turn. Details of the derivations will be presented in Appendices.

Table 3.1: Weak reactions considered in this paper.

Leptonic reactions	Semi-leptonic reactions
$\nu + l \to \nu + l$	$\nu_l + n \to l^- + p$
$\nu_e + \mu^- \leftrightarrows \nu_\mu + e^-$	$\bar{\nu}_l + p \to l^+ + n$
$\bar{\nu}_e + \mu^+ \leftrightarrows \bar{\nu}_\mu + e^+$	$\bar{\nu}_l + p + l^- \to n$
$\bar{\nu}_\mu + \mu^- \leftrightarrows \bar{\nu}_e + e^-$	$\nu + N \to \nu + N$
$\nu_\mu + \mu^+ \leftrightarrows \nu_e + e^+$	
$\mu^- \leftrightarrows e^- + \bar{\nu}_e + \nu_\mu$	
$\mu^+ \leftrightarrows e^+ + \nu_e + \bar{\nu}_\mu$	
$l^- + l^+ \leftrightarrows \nu + \bar{\nu}$	
$e^- + \mu^+ \leftrightarrows \nu_e + \bar{\nu}_\mu$	
$e^+ + \mu^- \leftrightarrows \bar{\nu}_e + \nu_\mu$	

3.1.1 Leptonic reactions

I first summarize the reaction rates of the leptonic reactions. I follow Guo et al. (2020); Yueh and Buchler (1976) for the derivation. Although the results are not original, I put them here for self-containedness of the paper and convenience for readers.

Scatterings: $\nu + l \leftrightarrows \nu + l$

For the scatterings of neutrino off a lepton, $\nu + l \leftrightarrows \nu + l$, ν can be any one of $\nu_e, \bar{\nu}_e, \nu_\mu, \bar{\nu}_\mu, \nu_\tau, \bar{\nu}_\tau$ and l is either $e^\pm$ or $\mu^\pm$. The 4-momenta of the incoming and outgoing neutrinos are denoted by q_1^α and q_2^α, respectively, while those of the incoming and outgoing leptons are expressed as p_1^α and p_2^α, respectively. The spin-averaged matrix element squared is expressed generally as Bruenn (1985)

$$\langle|\mathcal{M}|^2\rangle = 16 G_F^2 \left[\beta_1 (q_1\cdot p_1)(q_2\cdot p_2) + \beta_2 (q_1\cdot p_2)(q_2\cdot p_1) + \beta_3 m_l^2 (q_1\cdot q_2)\right], \tag{3.2}$$

where G_F is the Fermi coupling constant and the coefficients β_i are given in Table 3.2.

Table 3.2: Coefficients in the matrix element of lepton scatterings

Lepton scattering [1]	β_1 [2]	β_2	β_3
$\nu_l + l^- \leftrightarrows \nu_l + l^-$ or $\bar{\nu}_l + l^+ \leftrightarrows \bar{\nu}_l + l^+$	$[(C_V+1)+(C_A+1)]^2$	$[(C_V+1)-(C_A+1)]^2$	$(C_A+1)^2-(C_V+1)^2$
$\bar{\nu}_l + l^- \leftrightarrows \bar{\nu}_l + l^-$ or $\nu_l + l^+ \leftrightarrows \nu_l + l^+$	$[(C_V+1)-(C_A+1)]^2$	$[(C_V+1)+(C_A+1)]^2$	$(C_A+1)^2-(C_V+1)^2$
$\nu_{l_1} + l_2^- \leftrightarrows \nu_{l_1} + l_2^-$ or $\bar{\nu}_{l_1} + l_2^+ \leftrightarrows \bar{\nu}_{l_1} + l_2^+$	$(C_V+C_A)^2$	$(C_V-C_A)^2$	$C_A^2-C_V^2$
$\bar{\nu}_{l_1} + l_2^- \leftrightarrows \bar{\nu}_{l_1} + l_2^-$ or $\nu_{l_1} + l_2^+ \leftrightarrows \nu_{l_1} + l_2^+$	$(C_V-C_A)^2$	$(C_V+C_A)^2$	$C_A^2-C_V^2$

[a] $l \in \{e,\mu\}$, $l_1 \in \{e,\mu,\tau\}$, $l_2 \in \{e,\mu\}$ and $l_1 \neq l_2$
[b] $C_V = 2\sin^2\theta_W - 1/2$, $C_A = -1/2$ where θ_W is the Weinberg angle.

Then the inverse mean free path for neutrino can be written as

$$\begin{aligned}\frac{1}{\lambda_{\rm lsc}} &= \frac{1}{2E_1}\int \frac{d^3\boldsymbol{q}_2}{(2\pi)^3 2E_2}\frac{d^3\boldsymbol{p}_1}{(2\pi)^3 2p_1^0}\frac{d^3\boldsymbol{p}_2}{(2\pi)^3 2p_2^0} \\ &\quad\times 2f_l\left(p_1^0\right)\left[1-f_\nu\left(E_2\right)\right]\left[1-f_l\left(p_2^0\right)\right] \\ &\quad\times (2\pi)^4\,\delta^{(4)}\left(q_1^\alpha + p_1^\alpha - q_2^\alpha - p_2^\alpha\right)\left\langle|\mathcal{M}|^2\right\rangle \qquad (3.3)\\ &= \int dE_2 d\cos\theta\,\frac{q_2 E_2}{(2\pi)^2}\left[1-f_\nu\left(E_2\right)\right]R^{\rm in}\left(E_1,E_2,\cos\theta\right). \qquad (3.4)\end{aligned}$$

In the above equations, f's are the distribution functions in the phase space of individual particles involved and θ is the angle between $\boldsymbol{q}_1$ and $\boldsymbol{q}_2$; $E_1 = q_1^0$ and $E_2 = q_2^0$ are the energies of the incoming and outgoing neutrinos, respectively, and $q_2 = |\boldsymbol{q}_2|$. After evaluating some integrations in Eq. (3.3) analytically (see Appendix A.1 for details), we obtain the reaction kernel $R^{\rm in}$ as follows:

$$\begin{aligned}&R^{\rm in}(E_1,E_2,\cos\theta) \\ &= \frac{G_F^2}{(2\pi)^2 E_1 E_2}\left[\beta_1 I_1\left(E_1,E_2,\cos\theta\right)+\beta_2 I_2\left(E_1,E_2,\cos\theta\right)+\beta_3 I_3\left(E_1,E_2,\cos\theta\right)\right], \qquad (3.5)\end{aligned}$$

with

$$I_1\left(E_1,E_2,\cos\theta\right) = \frac{2\pi E_1^2 E_2^2}{\Delta^5}\left(1-\cos\theta\right)^2\left(A_1 J_2 + B_1 J_1 + C_1 J_0\right), \qquad (3.6)$$

$$I_2\left(E_1,E_2,\cos\theta\right) = I_1\left(-E_2,-E_1,\cos\theta\right), \qquad (3.7)$$

$$I_3\left(E_1,E_2,\cos\theta\right) = \frac{2\pi m_l^2 E_1 E_2}{\Delta}\left(1-\cos\theta\right)J_0, \qquad (3.8)$$

where the concrete expressions of $\Delta, A_1, B_1, C_1, J_0, J_1$ and J_2 are given in Appendix A.1. The Fermi-Dirac integrals included in J_i (see equations (A.13)–(A.15)) are numerically evaluated Aparicio (1998).

If the Boltzmann equation is employed as it is for the neutrino transport in PNS, the above expression is sufficient. In some approximate treatment, however, one may need to evaluate the integration over the outgoing neutrino momentum in Eq. (3.4) . I will do it in fact in the next section to compare the importance of the individual reactions quantitatively. In so doing, I assume that the neutrino distribution is given by the Fermi-Dirac distribution for β equilibrium and the double integrations with respect to E_2 and $\cos\theta$ are done numerically.

Table 3.3: Coefficients in the matrix element for the lepton flavor exchange/conversion reactions

Reactions	α_1	α_2
$\nu_e + \mu^- \leftrightarrows \nu_\mu + e^-$ or $\bar{\nu}_e + \mu^+ \leftrightarrows \bar{\nu}_\mu + e^+$	1	0
$\bar{\nu}_\mu + \mu^- \leftrightarrows \bar{\nu}_e + e^-$ or $\nu_\mu + \mu^+ \leftrightarrows \nu_e + e^+$	0	1

The emissivity of neutrino is given as

$$j_{\rm lsc} = \int dE_2\, d\cos\theta\, \frac{q_2 E_2}{(2\pi)^2} f_\nu\left(E_2\right) R^{\rm out}\left(E_1, E_2, \cos\theta\right), \tag{3.9}$$

where the notations are the same as in Eqs. (3.3) and (3.4) and the reaction kernel $R^{\rm out}$ is obtained from the detailed balance condition as follows:

$$R^{\rm out}\left(E_1, E_2, \cos\theta\right) = e^{-\beta(E_1 - E_2)} R^{\rm in}\left(E_1, E_2, \cos\theta\right). \tag{3.10}$$

Lepton flavor exchange/conversion reactions

The following 4 reactions

$$\nu_e + \mu^- \leftrightarrows \nu_\mu + e^- \tag{3.11}$$
$$\bar{\nu}_e + \mu^+ \leftrightarrows \bar{\nu}_\mu + e^+ \tag{3.12}$$
$$\bar{\nu}_\mu + \mu^- \leftrightarrows \bar{\nu}_e + e^- \tag{3.13}$$
$$\nu_\mu + \mu^+ \leftrightarrows \nu_e + e^+ \tag{3.14}$$

are collectively expressed as

$$\nu_1 + \mu \leftrightarrows \nu_2 + e, \tag{3.15}$$

and the 4-momenta of ν_1, ν_2, μ and e are denoted by q_1^α, q_2^α, p_μ^α and p_e^α, respectively. These reactions occur only through the leptonic CC and the spin-averaged matrix element squared is written in general as

$$\langle|\mathcal{M}|^2\rangle = 64 G_F^2 \left[\alpha_1 (q_1 \cdot p_e)(q_2 \cdot p_\mu) + \alpha_2 (q_1 \cdot p_\mu)(q_2 \cdot p_e)\right]. \tag{3.16}$$

The coefficients α_1 and α_2 are given in Table 3.3.

The absorptivity and emissivity for ν_1 are expressed, respectively, as

$$\frac{1}{\lambda_{\nu_1}} = \int \frac{d^3\boldsymbol{q}_2}{(2\pi)^3} \left[1 - f_{\nu_2}\left(E_2\right)\right] R_\nu^{\rm in}\left(E_1, E_2, \cos\theta\right), \tag{3.17}$$

$$j_{\nu_1} = \int \frac{d^3\boldsymbol{q}_2}{(2\pi)^3} f_{\nu_2}\left(E_2\right) R_\nu^{\rm out}\left(E_1, E_2, \cos\theta\right), \tag{3.18}$$

just as in the leptonic scatterings. The reaction kernels are given as

$$R_\nu^{\rm in}\left(E_1, E_2, \cos\theta\right) = e^{\beta(E_1 - E_2 + \mu_\mu - \mu_e)} R_\nu^{\rm out}\left(E_1, E_2, \cos\theta\right), \tag{3.19}$$

$$R_\nu^{\rm out}\left(E_1, E_2, \cos\theta\right) = \frac{8 G_F^2}{(2\pi)^2 E_1 E_2} \left[\alpha_1 I_1\left(E_1, E_2, \cos\theta\right) + \alpha_2 I_2\left(E_1, E_2, \cos\theta\right)\right], \tag{3.20}$$

where I_1 and I_2 are expressed, respectively, as

$$I_1\left(E_1, E_2, \cos\theta\right) = \frac{2\pi E_1 E_2}{\Delta^5} \left(A_1 J_2 + B_1 J_1 + C_1 J_0\right), \tag{3.21}$$

$$I_2\left(E_1, E_2, \cos\theta\right) = I_1\left(-E_2, -E_1, \cos\theta\right). \tag{3.22}$$

Details of $\Delta, A_1, B_1, C_1, J_0, J_1$ and J_2 are presented in Appendix A.2.

The absorptivity and emissivity for ν_2 are also obtained as

$$\frac{1}{\lambda_{\nu_2}} = \int \frac{d^3\boldsymbol{q}_1}{(2\pi)^3} \left[1 - f_{\nu_1}(E_1)\right] R_\nu^{\rm out}(E_1, E_2, \cos\theta), \tag{3.23}$$

$$j_{\nu_2} = \int \frac{d^3\boldsymbol{q}_1}{(2\pi)^3} f_{\nu_1}(E_1) R_\nu^{\rm in}(E_1, E_2, \cos\theta). \tag{3.24}$$

Muon decays: $\mu^- \leftrightarrows e^- + \bar{\nu}_e + \nu_\mu$ and $\mu^+ \leftrightarrows e^+ + \nu_e + \bar{\nu}_\mu$

Below I give only the reaction rate of $\mu^- \leftrightarrows e^- + \bar{\nu}_e + \nu_\mu$. The counterpart for $\mu^+ \leftrightarrows e^+ + \nu_e + \bar{\nu}_\mu$ can be obtained just by changing the signature of the chemical potentials of charged leptons and exchanging the neutrino and anti-neutrino of the same flavor. The spin-averaged matrix element squared is written as

$$\langle|\mathcal{M}|^2\rangle = 64 G_F^2 (q_{\bar{\nu}_e} \cdot p_e)(q_{\nu_\mu} \cdot p_\mu). \tag{3.25}$$

The absorptivity and emissivity for $\bar{\nu}_e$ are expressed, respectively, as

$$\frac{1}{\lambda_{\bar{\nu}_e}} = \int \frac{d^3\boldsymbol{q}_{\nu_\mu}}{(2\pi)^3} f_{\nu_\mu}\left(E_{\nu_\mu}\right) R_{\bar{\nu}_e}^{\rm in}\left(E_{\bar{\nu}_e}, E_{\nu_\mu}, \cos\theta\right), \tag{3.26}$$

$$j_{\bar{\nu}_e} = \int \frac{d^3\boldsymbol{q}_{\nu_\mu}}{(2\pi)^3} \left[1 - f_{\nu_\mu}\left(E_{\nu_\mu}\right)\right] R_{\bar{\nu}_e}^{\rm out}\left(E_{\bar{\nu}_e}, E_{\nu_\mu}, \cos\theta\right), \tag{3.27}$$

where the reaction kernels are given as

$$R_{\bar{\nu}_e}^{\rm in}\left(E_{\bar{\nu}_e}, E_{\nu_\mu}, \cos\theta\right) = e^{\beta\left(E_{\bar{\nu}_e} + E_{\nu_\mu} + \mu_e - \mu_\mu\right)} R_{\bar{\nu}_e}^{\rm out}\left(E_{\bar{\nu}_e}, E_{\nu_\mu}, \cos\theta\right), \tag{3.28}$$

$$R_{\bar{\nu}_e}^{\rm out}\left(E_{\bar{\nu}_e}, E_{\nu_\mu}, \cos\theta\right) = \frac{8 G_F^2}{(2\pi)^2 E_{\bar{\nu}_e} E_{\nu_\mu}} I_1\left(E_{\bar{\nu}_e}, E_{\nu_\mu}, \cos\theta\right), \tag{3.29}$$

with

$$I_1\left(E_{\bar{\nu}_e}, E_{\nu_\mu}, \cos\theta\right) = \frac{2\pi E_{\bar{\nu}_e} E_{\nu_\mu}}{\Delta^5} \Theta(D) \left(A_1 J_2 + B_1 J_1 + C_1 J_0\right). \tag{3.30}$$

Details of $\Delta, A_1, B_1, C_1, D, J_0, J_1$ and J_2 are presented in Appendix A.3. The absorptivity and emissivity for ν_μ can be obtained just by exchanging $\bar{\nu}_e \leftrightarrow \nu_\mu$ in the above expression.

Pair creations/annihilations: $l^- + l^+ \leftrightharpoons \nu + \bar{\nu}$

In the pair process, $l^- + l^+ \leftrightharpoons \nu + \bar{\nu}$, ν is any one of ν_e, ν_μ, ν_τ and l is either e or μ, and the 4-momenta of neutrino and anti-neutrino are denoted by q_1^α and q_2^α, respectively, and those of lepton and anti-lepton by p_1^α and p_2^α, respectively. The spin-averaged matrix element squared is expressed as

$$\begin{aligned}\langle|\mathcal{M}|^2\rangle =& 32\alpha G_F^2 \left[\beta_1 (q_1 \cdot p_1)(q_2 \cdot p_2) + \beta_2 (q_1 \cdot p_2)(q_2 \cdot p_1)\right. \\ &\left. + \beta_3 m_l^2 (q_1 \cdot q_2)\right],\end{aligned} \tag{3.31}$$

where the coefficients α and β_i are given in Table 3.4. I present the absorptivity and emissivity for ν_1 alone, since those for ν_2 can be obtained just by exchanging the roles of ν_1 and ν_2.

Table 3.4: Coefficients in matrix element of pair annihilation

Pair process [1]	α	β_1 [2]	β_2	β_3
$l^- + l^+ \to \nu_l + \bar{\nu}_l$	1/4	$[(C_V+1)-(C_A+1)]^2$	$[(C_V+1)+(C_A+1)]^2$	$(C_A+1)^2-(C_V+1)^2$
$l^- + l^+ \leftarrow \nu_l + \bar{\nu}_l$	1	$[(C_V+1)-(C_A+1)]^2$	$[(C_V+1)+(C_A+1)]^2$	$(C_A+1)^2-(C_V+1)^2$
$l_1^- + l_1^+ \to \nu_{l_2} + \bar{\nu}_{l_2}$	1/4	$(C_V-C_A)^2$	$(C_V+C_A)^2$	$C_A^2-C_V^2$
$l_1^- + l_1^+ \leftarrow \nu_{l_2} + \bar{\nu}_{l_2}$	1	$(C_V-C_A)^2$	$(C_V+C_A)^2$	$C_A^2-C_V^2$

[a] $l \in \{e,\mu\}$, $l_1 \in \{e,\mu\}$, $l_2 \in \{e,\mu,\tau\}$ and $l_1 \neq l_2$
[b] $C_V = 2\sin^2\theta_W - 1/2$, $C_A = -1/2$ where θ_W is the Weinberg angle.

The results are written as

$$\frac{1}{\lambda_{\nu_1}} = \int \frac{d^3\boldsymbol{q}_2}{(2\pi)^3} f_{\nu_2}(E_2)\, R^{\rm in}_{\nu_1}(E_1, E_2, \cos\theta), \tag{3.32}$$

$$j_{\nu_1} = \int \frac{d^3\boldsymbol{q}_2}{(2\pi)^3} \left[1 - f_{\nu_2}(E_2)\right] R^{\rm out}_{\nu_1}(E_1, E_2, \cos\theta), \tag{3.33}$$

where the reaction kernels are given as

$$R^{\rm in}_{\nu_1}(E_1, E_2, \cos\theta) = e^{\beta(E_1+E_2)} R^{\rm out}_{\nu_1}(E_1, E_2, \cos\theta), \tag{3.34}$$

$$\begin{aligned} &R^{\rm out}_{\nu_1}(E_1, E_2, \cos\theta) \\ &= \frac{G_F^2}{(2\pi)^2 E_1 E_2}\left[\beta_1 I_1(E_1, E_2, \cos\theta) + \beta_2 I_2(E_1, E_2, \cos\theta)\right. \\ &\qquad \left. + \beta_3 I_3(E_1, E_2, \cos\theta)\right], \end{aligned} \tag{3.35}$$

with

$$\begin{aligned} &I_1(E_1, E_2, \cos\theta) \\ &= \frac{2\pi E_1^2 E_2^2}{\Delta^5}(1-\cos\theta)^2\,\Theta(D)\,(A_1 J_2 + B_1 J_1 + C_1 J_0), \end{aligned} \tag{3.36}$$

$$I_2(E_1, E_2, \cos\theta) = I_1(E_2, E_1, \cos\theta), \tag{3.37}$$

$$I_3(E_1, E_2, \cos\theta) = \frac{2\pi m_l^2 E_1 E_2}{\Delta}(1-\cos\theta)\,\Theta(D)\,J_0. \tag{3.38}$$

The details of $\Delta, A_1, B_1, C_1, D, J_0, J_1$ and J_2 are given in Appendix A.4.

Leptonic annihilations:
$e^- + \mu^+ \leftrightarrows \nu_e + \bar{\nu}_\mu$ **and** $e^+ + \mu^- \leftrightarrows \bar{\nu}_e + \nu_\mu$

These reactions normally give rather minor contributions to the absorptivity and emissivity, since the populations of positively-charged leptons are strongly suppressed. I present the calculation of these reaction rates for completeness. The two reactions are collectively denoted by $e + \mu \leftrightarrows \nu_e + \nu_\mu$. The spin-averaged matrix element squared is expressed as

$$\langle|\mathcal{M}|^2\rangle = 64\alpha G_F^2 (q_{\nu_e}\cdot p_e)(q_{\nu_\mu}\cdot p_\mu), \tag{3.39}$$

where $\alpha = 1/2$ for $e + \mu \to \nu_e + \nu_\mu$ and $\alpha = 2$ for $\nu_e + \nu_\mu \to e + \mu$.

The absorptivity and emissivity for $\bar{\nu}_e$ are written as

$$\frac{1}{\lambda_{\nu_e}} = \int \frac{d^3\boldsymbol{q}_{\nu_\mu}}{(2\pi)^3} \left[1 - f_{\nu_\mu}\left(E_{\nu_\mu}\right)\right] R^{\rm in}_{\nu_e}\left(E_{\nu_e}, E_{\nu_\mu}, \cos\theta\right), \tag{3.40}$$

$$j_{\nu_e} = \int \frac{d^3\boldsymbol{q}_{\nu_\mu}}{(2\pi)^3} f_{\nu_\mu}\left(E_{\nu_\mu}\right) R^{\rm out}_{\nu_e}\left(E_{\nu_e}, E_{\nu_\mu}, \cos\theta\right), \tag{3.41}$$

where the reaction kernels are expressed as

$$R^{\rm in}_{\nu_e}\left(E_{\nu_e}, E_{\nu_\mu}, \cos\theta\right) = e^{\beta\left(E_{\nu_e}+E_{\nu_\mu}-\mu_e-\mu_\mu\right)} R^{\rm out}_{\nu_e}\left(E_{\nu_e}, E_{\nu_\mu}, \cos\theta\right), \tag{3.42}$$

$$R^{\rm out}_{\nu_e}\left(E_{\nu_e}, E_{\nu_\mu}, \cos\theta\right) = \frac{8G_F^2}{(2\pi)^2 E_{\nu_e} E_{\nu_\mu}} I_1\left(E_{\nu_e}, E_{\nu_\mu}, \cos\theta\right), \tag{3.43}$$

with

$$I_1\left(E_{\nu_e}, E_{\nu_\mu}, \cos\theta\right) = \frac{2\pi E_{\nu_e} E_{\nu_\mu}}{\Delta^5} \Theta\left(D\right)\left(A_1 J_2 + B_1 J_1 + C_1 J_0\right). \tag{3.44}$$

Details of $\Delta, A_1, B_1, C_1, D, J_0, J_1$ and J_2 are given in Appendix A.5. The absorptivity and emissivity for ν_μ can be obtained just by exchanging $\nu_e \leftrightarrow \nu_\mu$ in the above formulae.

3.1.2 Semi-leptonic reactions

In this subsection, I deal with the interactions that involve nucleons, that is, the captures of electron- and muon-type neutrinos on neutron and those of the electron- and muon-type anti-neutrinos on proton, the scatterings of all flavors of neutrinos on nucleons and the beta decay of neutron and its inverse. These reactions, especially those via the CC are sensitive to the modifications of the dispersion relations of nucleons in the hot dense matter because they shift the thresholds in the reactions. In this work, I take them into account at the mean-field level. Although it is well known that the vertex corrections need to be considered simultaneously at the level of the random phase approximation Burrows and Sawyer (1998); Reddy et al. (1999); Yamada and Toki (1999); Oertel et al. (2020), I will defer it to a later paper as it is a major undertaking and I think it is still meaningful to make comparisons with other works that also neglected the corrections Guo et al. (2020). I note that our formulation is based on the structure function of nucleons, which is suited for the incorporation of RPA later. It should be also stressed that I employ in this paper the most generic form of the weak currents of nucleons with the weak magnetism and other form factors accounted for and fully consider the recoil of nucleons.

CC reactions: $\nu_l + n \leftrightarrows l^- + p$ **and** $\bar{\nu}_l + p \leftrightarrows l^+ + n$

I write these processes in general as

$$\nu_{l,1} + N_2 \leftrightarrows l_3 + N_4, \tag{3.45}$$

where $\nu_{l,1}$ denotes the neutrino (anti-neutrino), N_2 the neutron (proton), l_3 the charged lepton (antilepton), i.e., e or μ and N_4 the proton (neutron). The interaction Lagrangian at low energies may be given by the Fermi theory as

$$\mathcal{L} = \frac{G_F \cos\theta_C}{\sqrt{2}} l_\alpha \, j^\alpha_{\rm CC}, \tag{3.46}$$

where θ_C is the Cabibbo angle; the leptonic current is given as

$$l_\alpha = \bar{l}_3 \gamma_\alpha \left(1 - \gamma^5\right) \nu_1, \tag{3.47}$$

and the nucleonic charged current is expressed as

$$j^\alpha_{\rm CC} = \bar{\Psi}_4 \Big\{ \gamma^\alpha \left[G_V\left(q^2\right) - G_A\left(q^2\right)\gamma^5 \right] + F_2\left(q^2\right) \frac{i\sigma^{\alpha\beta} q_\beta}{M} - G_P\left(q^2\right)\gamma^5 \frac{q^\alpha}{M} \Big\} \Psi_2. \tag{3.48}$$

In the above expression, Ψ_2 and Ψ_4 are the wave functions of N_2 and N_4, respectively, and $q^\alpha = p_1^\alpha - p_3^\alpha$ is momentum transfer to nucleon; $M = \left(m_n + m_p\right)/2$ is the bare average mass of nucleons; the vector, axial vector, tensor and pseudoscalar form factors are given by Leitner (2005), respectively, as

$$G_V(q^2) = \frac{g_V \left[1 - \dfrac{q^2(\gamma_p - \gamma_n)}{4M^2}\right]}{\left(1 - \dfrac{q^2}{4M^2}\right)\left(1 - \dfrac{q^2}{M_V^2}\right)^2}, \tag{3.49}$$

$$G_A(q^2) = \frac{g_A}{\left(1 - \dfrac{q^2}{M_A^2}\right)^2}, \tag{3.50}$$

$$F_2(q^2) = \frac{\gamma_p - \gamma_n - 1}{\left(1 - \dfrac{q^2}{4M^2}\right)\left(1 - \dfrac{q^2}{M_V^2}\right)^2}, \tag{3.51}$$

$$G_P(q^2) = \frac{2M^2 G_A(q^2)}{m_\pi^2 - q^2}, \tag{3.52}$$

where $q^2 = q_\alpha q^\alpha$; $g_V = 1$ and $g_A = 1.27$ are the vector and axial vector coupling constants, respectively; $\gamma_p = 2.793$ and $\gamma_n = -1.913$ are the magnetic moments of proton and neutron, respectively; $M_V = 840\,\mathrm{MeV}$, $M_A = 1\,\mathrm{GeV}$ and $m_\pi = 139.57\,\mathrm{MeV}$ are the vector, axial and pion mass, respectively. Note that the tensor contribution to Eq. (3.48) is nothing but the weak magnetism. The spin-averaged matrix element squared can be expressed as

$$\langle |\mathcal{M}|^2 \rangle = \beta \frac{G_F^2 \cos^2\theta_C}{2} L_{\mu\nu} \Lambda^{\mu\nu}, \tag{3.53}$$

with the leptonic tensor $L_{\mu\nu}$ and the hadronic counterpart $\Lambda^{\mu\nu}$; the coefficient β originates from the spin average; $\beta = 1/2$ for $\nu_{l,1} + N_2 \to l_3 + N_4$ and $\beta = 1/4$ for $l_3 + N_4 \to \nu_{l,1} + N_2$. The leptonic tensor is written as

$$L_{\mu\nu} = 8\left(p_{3\mu}p_{1\nu} + p_{3\nu}p_{1\mu} - \eta_{\mu\nu}(p_1 \cdot p_3) \pm i p_3^\rho p_1^\sigma \epsilon_{\rho\mu\sigma\nu}\right), \tag{3.54}$$

where the sign is + for neutrino and − for anti-neutrino and all neutrinos are assumed to be massless. The hadronic tensor is modified in medium and, as I mentioned earlier, I take into account the modifications of the free nucleon propagators at the mean field level as follows Roberts and Reddy (2017a):

$$\Lambda^{\mu\nu} = \mathrm{Tr}\left\{ (\tilde{\not{p}}_4 + m_4^*) \left[\gamma^\mu (G_V - G_A\gamma^5) + F_2 \frac{i\sigma^{\mu\alpha}q_\alpha}{2M} - G_P \frac{q^\mu}{M}\gamma^5\right] \times (\tilde{\not{p}}_2 + m_2^*) \left[\gamma^\nu (G_V - G_A\gamma^5) - F_2 \frac{i\sigma^{\nu\beta}q_\beta}{2M} + G_P \frac{q^\nu}{M}\gamma^5\right] \right\}, \tag{3.55}$$

where I introduce the following notation: $\tilde{p}_2^\alpha = (E_2^*, \boldsymbol{p}_2)$, $\tilde{p}_4^\alpha = (E_4^*, \boldsymbol{p}_4)$ and

$$E_{2,4}^* = E_{2,4} - U_{2,4}, \tag{3.56}$$

with $U_{2,4}$ being the mean field potentials of particles 2 and 4; $E_{2,4}^*$ is given by the on-shell condition in medium as

$$E_{2,4}^* = \sqrt{|\boldsymbol{p}_{2,4}|^2 + {m_{2,4}^*}^2}, \tag{3.57}$$

where $m_{2,4}^*$ are the effective masses of particles 2 and 4, respectively.

The inverse mean free path of ν_1 is expressed as

$$\begin{aligned}\frac{1}{\lambda(E_1)} &= \int \frac{d^3\boldsymbol{p}_2}{(2\pi)^3}\frac{d^3\boldsymbol{p}_3}{(2\pi)^3}\frac{d^3\boldsymbol{p}_4}{(2\pi)^3} 2 f_2(E_2^*)\left[(1-f_3(E_3)\right]\left[1-f_4(E_4^*)\right] \\ &\quad\times \frac{1}{2^4 E_1 E_2^* E_3 E_4^*}(2\pi)^4\delta^{(4)}(p_1^\mu + p_2^\mu - p_3^\mu - p_4^\mu)|\mathcal{M}|^2 \\ &= \frac{G_F^2\cos^2\theta_C}{2}\frac{1}{E_1}\int \frac{d^3\boldsymbol{p}_3}{(2\pi)^3 2E_3}\left[1-f_3(E_3)\right] L_{\mu\nu}\,\mathcal{S}^{\mu\nu}\left(q^0, q\right), \end{aligned} \tag{3.58}$$

where $\mathcal{S}^{\mu\nu}$ is the so-called dynamical structure function of nucleon. It can be decomposed as follows due to the isotropy of the system:

$$\mathcal{S}^{\mu\nu}\left(q^0, q\right) = \bar{A}P_1^{\mu\nu} + \bar{B}P_2^{\mu\nu} + \bar{C}P_3^{\mu\nu} + \bar{D}P_4^{\mu\nu} + \bar{E}P_5^{\mu\nu}, \tag{3.59}$$

where the coefficients $\bar{A}, \bar{B}, \bar{C}, \bar{D}$ and $\bar{E}$ are functions of q^0 and $q = |\boldsymbol{q}|$, and $P_1^{\mu\nu}, P_2^{\mu\nu}, P_3^{\mu\nu}, P_4^{\mu\nu}$ and $P_5^{\mu\nu}$ are projectors relative to momentum transfer q^μ. Their detailed expressions are given in Appendix B. The Fermi integrals included in the coefficients from $\bar{A}$ to $\bar{E}$ and other remaining integrals in Eq. (3.58) are evaluated numerically.

The emissivity can be obtained from the absorptivity using the detailed balance condition as

$$\begin{aligned} j(E_1) &= \frac{G_F^2\cos^2\theta_C}{2}\frac{1}{E_1}\int \frac{d^3\boldsymbol{p}_3}{(2\pi)^3 2E_3} f_3(E_3) \\ &\quad\times \exp\left[\beta(-q^0 - \mu_2 + \mu_4)\right] L_{\mu\nu}\,\mathcal{S}^{\mu\nu}\left(q^0, q\right). \end{aligned} \tag{3.60}$$

NC reaction: $\nu + N \leftrightarrows \nu + N$

This is a neutrino scattering on a nucleon, which is denoted by

$$\nu_1 + N_2 \leftrightarrows \nu_3 + N_4, \tag{3.61}$$

and its rate is calculated in a similar way to the CC reactions presented above. The interaction Lagrangian is written as

$$\mathcal{L} = \frac{G_F}{\sqrt{2}} l_\alpha\, j_{\mathrm{NC}}^\alpha, \tag{3.62}$$

where the leptonic neutral current is expressed as

$$l_\alpha = \bar{\nu}_3\gamma_\alpha\left(1-\gamma^5\right)\nu_1, \tag{3.63}$$

whereas the nucleonic neutral current is given as

$$j_{\mathrm{NC}}^\alpha = \bar{\Psi}_4\left\{\gamma^\alpha\left[G_1^N\left(q^2\right) - G_A^N\left(q^2\right)\gamma^5\right] + G_2^N\left(q^2\right)\frac{i\sigma^{\alpha\beta}q_\beta}{M}\right\}\Psi_2. \tag{3.64}$$

The form factors in this expression are written as

$$G^p_{1,2}\left(q^2\right) = \frac{1}{2}\left[\left(1-4\sin^2\theta_W\right)F^p_{1,2} - F^n_{1,2}\right], \tag{3.65}$$

$$G^n_{1,2}\left(q^2\right) = \frac{1}{2}\left[\left(1-4\sin^2\theta_W\right)F^n_{1,2} - F^p_{1,2}\right], \tag{3.66}$$

$$G^p_A\left(q^2\right) = \frac{1}{2}G_A\left(q^2\right), \tag{3.67}$$

$$G^n_A\left(q^2\right) = -\frac{1}{2}G_A\left(q^2\right), \tag{3.68}$$

with

$$F^p_1\left(q^2\right) = \frac{1-\dfrac{q^2\gamma_p}{4M^2}}{\left(1-\dfrac{q^2}{4M^2}\right)\left(1-\dfrac{q^2}{M_V^2}\right)^2}, \tag{3.69}$$

$$F^p_2\left(q^2\right) = \frac{\gamma_p - 1}{\left(1-\dfrac{q^2}{4M^2}\right)\left(1-\dfrac{q^2}{M_V^2}\right)^2}, \tag{3.70}$$

$$F^n_1\left(q^2\right) = \frac{-\dfrac{q^2\gamma_n}{4M^2}}{\left(1-\dfrac{q^2}{4M^2}\right)\left(1-\dfrac{q^2}{M_V^2}\right)^2}, \tag{3.71}$$

$$F^n_2\left(q^2\right) = \frac{\gamma_n}{\left(1-\dfrac{q^2}{4M^2}\right)\left(1-\dfrac{q^2}{M_V^2}\right)^2}, \tag{3.72}$$

and $G_A(q^2)$ is given in Eq.(3.50). The inverse mean free path is written in general as

$$\frac{1}{\lambda(E_1)} = \frac{G_F^2}{2}\frac{1}{E_1}\int\frac{d^3\boldsymbol{p}_3}{(2\pi)^3 2E_3}\left[1-f_3(E_3)\right]L_{\mu\nu}\,\mathcal{S}^{\mu\nu}\left(q^0,q\right), \tag{3.73}$$

where $\mathcal{S}^{\mu\nu}$ is the structure function calculated in the same way as for the CC reaction just by replacing the form factors. The emissivity is also expressed as

$$j(E_1) = \frac{G_F^2}{2}\frac{1}{E_1}\int\frac{d^3\boldsymbol{p}_3}{(2\pi)^3 2E_3}f_3(E_3)\exp\left[-\beta q^0\right]L_{\mu\nu}\,\mathcal{S}^{\mu\nu}\left(q^0,q\right), \tag{3.74}$$

from the detailed balance condition.

Beta decay and its inverse: $\bar{\nu}_l + p + l^- \leftrightarrows n$

The interaction Lagrangian, matrix element and form factors are the same as those for the CC reaction except for the momentum transfer now given as $q^\alpha = p_1^\alpha + p_3^\alpha$. The inverse mean free path and emissivity are then expressed, respectively, as

$$\frac{1}{\lambda(E_1)} = \frac{G_F^2}{2}\frac{1}{E_1}\int\frac{d^3\boldsymbol{p}_3}{(2\pi)^3 2E_3}f_3(E_3)L_{\mu\nu}\,\mathcal{S}^{\mu\nu}\left(q^0,q\right), \tag{3.75}$$

$$j(E_1) = \frac{G_F^2}{2}\frac{1}{E_1}\int\frac{d^3\boldsymbol{p}_3}{(2\pi)^3 2E_3}\left[1-f_3(E_3)\right] \times\exp\left[\beta(-q^0-\mu_2+\mu_4)\right]L_{\mu\nu}\,\mathcal{S}^{\mu\nu}\left(q^0,q\right). \tag{3.76}$$

Table 3.5: Thermodynamical conditions considered in this study. Units of temperature T, chemical potentials, μ_n, μ_p, μ_e and μ_μ, nucleon potential difference $U_n - U_p$ and effective mass m^* are all MeV.

Model	$t_{\rm pb}$(s)	r(km)	ρ(g/cm^3)	T	Y_e	Y_μ	Y_n	Y_p[1]	μ_n	μ_p	μ_e	μ_μ	$U_n - U_p$
t1S	1	20.0	5.0×10^{12}	5.5	0.036	0.0025	0.95	2.3×10^{-2}	933.8	909.0	25.6	102.8	3.5
t3S	3	16.5	1.0×10^{13}	5.0	0.026	0.0025	0.94	1.1×10^{-2}	938.6	906.8	30.2	104.2	7.1
t10S	10	14.5	2.0×10^{13}	4.0	0.025	0.0025	0.86	4.5×10^{-4}	943.3	896.2	42.0	105.7	13.9
t30S	30	13.6	4.5×10^{13}	2.7	0.018	0.0025	0.84	5.0×10^{-11}	948.9	878.7	47.3	107.2	30.2
t50S	50	13.4	6.1×10^{13}	1.5	0.017	0.0025	0.79	2.0×10^{-20}	951.0	870.4	52.2	107.8	38.8
t1D	1	10.8	1.2×10^{14}	35.6	0.22	0.05	0.73	0.27	904.0	836.3	126.4	89.8	27.0
t3D	3	9.4	2.1×10^{14}	35.0	0.20	0.05	0.75	0.25	930.4	849.2	156.5	114.5	30.9
t10D	10	6.0	3.5×10^{14}	30.2	0.17	0.05	0.78	0.22	981.3	883.2	186.2	146.3	30.2
t30D	30	1.7	4.7×10^{14}	17.7	0.16	0.05	0.80	0.20	1037.0	924.8	210.2	174.1	28.5
t50D	50	1.69	4.9×10^{14}	2.8	0.15	0.05	0.80	0.20	1046.1	932.3	216.3	182.8	28.5

3.2 Results and discussions

Employing the formulae I obtained so far, I now evaluate the rates of all reactions listed in Table 3.1 numerically for the thermodynamic conditions that we find typically in the PNS cooling. I compare the inverse mean free paths for these reactions to see their relative importance quantitatively. I also discuss their possible implications for the cooling timescale.

For this purpose, I first extract the thermodynamical data at different times from a one-dimensional PNS cooling calculation under spherical symmetry conducted in Nakazato et al. (2018). The simulation was done as follows: core-collapse of a 15 $M_\odot$ progenitor Woosley and Weaver (1995) was first computed with the general relativistic neutrino-radiation hydrodynamics code Sumiyoshi et al. (2005) until $t = 0.3\,$s after core bounce when the shock wave is stalled. Knowing that this model does not explode in 1D but expecting that it will explode in multi-dimensions, the authors in Nakazato et al. (2018) extracted the region inside the shock wave (up to mass coordinate of $\sim 1.47 M_\odot$) from the result of the first simulation and use it as an initial condition of the second simulation of PNS cooling. In this second simulation, the quasi-static evolution of the PNS is computed by solving the Tolman-Oppenheimer-Volkov equation together with the neutrino transfer equation, the latter of which was solved with the multi-group flux limited diffusion scheme for neutrino transfer Suzuki (1994); the Shen EoS Shen et al. (2011) was adopted.

I then picked up the snapshots at $t = 1, 3, 10, 30, 50\,$s post bounce. At each time, I extracted the trio of the thermodynamical quantities: density, temperature and electron fraction (ρ, T, Y_e) at the neutrino sphere for the average neutrino energy as well as at the radius where the temperature reaches the maximum. Note that the peak temperature occurs off center particularly at early times. The choice of the latter position is motivated by the fact that the muon fraction is expected to be largest, since it is known to be correlated with temperature Bollig et al. (2017). It is noted here that the second simulation (and the first one as well) neglected muon entirely. I hence added it by hand as a parameter in this paper: $Y_\mu = 0.0025$ at the neutrino sphere and $Y_\mu = 0.05$ at the maximum temperature, with Y_μ being the muon fraction. As already explained in detail, the rates of the semi-leptonic reactions depend not only on the chemical potentials of nucleons but also on their dispersion relations in medium. I re-evaluated them at the mean field level,

just in the same way to produce the EoS, for the given quartet (ρ, T, Y_e, Y_μ). Note that the effective masses of neutron and proton are the same in the Shen EoS. All the relevant quantities are listed in Table 3.5.

3.2.1 Inverse mean free paths at $t_{\rm pb} = 10\,{\rm s}$

I first present the inverse mean free paths for all neutrino reactions at $t_{\rm pb} = 10\,{\rm s}$ as the fiducial model. Figure 3.1 shows the inverse mean free paths at the neutrino sphere (model t10S) as a function of the energy of the incoming neutrino.

Panel (a) is the results for ν_e. As expected the ν_e absorption on neutron, the CC reaction, is the dominant source of opacity at high energies of the incident neutrino $E_{\nu_e} \gtrsim 10\,{\rm MeV}$. The nucleon scattering is the second contributer at the same energy range. Since protons are much less abundant ($Y_p = 4.5 \times 10^{-4}$) than neutrons ($Y_n = 0.86$) due to the formation of heavy nuclei, the scattering on the former is dominnant by more than 4 orders. Note that the coherent scatterings on heavy nuclei are not considered here.

At low energies ($E_{\nu_e} \lesssim 10\,{\rm MeV}$), on the other hand, the flavor exchange reaction $\nu_e + \mu^- \to \nu_\mu + e^-$ dominates the opacity. This is one of the muon-related interactions, the main topic in this paper. It should be mentioned that this reaction is more important than the electron scattering at almost all energies of relevance ($E_{\nu_e} \lesssim 100\,{\rm MeV}$). This is due to the large mass difference between muon and electron.

The scattering on muon, on the other hand, is always smaller than that on electron, since muons are much less abundant. Note that the energy dependence is also different between these two reactions, since the muon is much heavier than the electron and the electron is strongly degenerate. One can see that the rise of the inverse mean free path for the muon scattering with the neutrino energy becomes less steep at $E_{\nu_e} \gtrsim 100\,{\rm MeV}$ as muons get relativistic.

The pair production of muon and anti-muon is less efficient than that of electron-positron again for the lager mass of muon. The three body reactions are very minor, since they involve positrons, the abundance of which is suppressed by the degeneracy of electrons.

Panel (b) shows the inverse mean free paths for $\bar{\nu}_e$. This time the absorption via the charged current is quite minor, since protons are scarce and, more importantly, the potential difference between proton and neutron disfavors the reaction, producing an effective threshold in fact. Note that this is also the threshold for the inverse beta decay of neutron, which occurs essentially below it.

The nucleon scatterings are dominant contributors to the inverse mean free path at high neutrino energies ($E_{\bar{\nu_e}} \gtrsim 10\,{\rm MeV}$), with the neutron scattering overwhelming the proton scattering for the same reason as for ν_e. Interestingly, the inverse muon decay is dominant below $\sim 10\,{\rm MeV}$. This happens because there is a large phase space available. Incidentally, the counterpart for ν_e: $\nu_e + e^+ + \bar{\nu}_\mu \to \mu^+$ is pretty minor, since the positron is strongly suppressed. Other features are common to ν_e.

For ν_μ, the scattering on neutron again gives the dominant contribution in the range of $E_{\nu_\mu} = 10 - 100\,{\rm MeV}$ (panel (c)). The inverse muon decay comes first at lower energies just as for $\bar{\nu}_e$. At higher energies, $E_{\nu_\mu} + U_n - U_p \gtrsim 100\,{\rm MeV}$, on the other hand, the neutrino capture on neutron becomes the most important. The scattering on muon is subdominant but is comparable with or even higher than the scattering on electron because the latter occurs only through the neutral current while the former takes place through both the neutral and charged currents. The flavor exchange reaction $\nu_\mu + e^- \to \nu_e + \mu^-$ is substantial only at high energies $E_{\nu_\mu} \gtrsim 100\,{\rm MeV}$, since the mass difference between electron and muon

disfavors in this time. The electron-positron and muon-anti-muon pair productions are both very minor.

As for $\bar{\nu}_\mu$ (panel (d)), the scattering on neutron is dominant at $E_{\bar{\nu}_\mu} \gtrsim 10\,\mathrm{MeV}$ while the flavor exchange reaction $\bar{\nu}_\mu + \mu^- \to \bar{\nu}_e + e^-$ pairs becomes most important at lower energies $E_{\nu_\mu} \lesssim 10\,\mathrm{MeV}$. The scattering on muon is more important than that on electron and the production of electron-positron pair is comparable to the former. The production of muon-anti-muon becomes as important at very high energies $E_{\bar{\nu}_\mu} \gtrsim 100\,\mathrm{MeV}$. The absorption and scattering on proton are much smaller due to the small abundance of proton. The inverse beta decay of muon is even smaller, since the positron abundance is more strongly suppressed.

In the presence of muons, the degeneracy between the μ-type and τ-type (anti-)neutrino is resolved. The muonic reactions for τ-type (anti-)neutrino occur only through the neutral leptonic or nucleonic current and are always subdominant, with the scattering on neutron being dominant (panel (e)). The difference in opacity between the electron and muon scatterings is originated from the differences in the electron and muon fractions and as well as in the Fermi-blocking factor. The difference between ν_τ and $\bar{\nu}_\tau$ is pretty minor. Note, however, that the opacity is always smaller for $\bar{\nu}_\tau$ than for ν_τ as pointed out in Horowitz (2002). The difference in the neutrino scatterings on nucleon is ascribed to the weak magnetism in the nucleon current.

So far I have been concerned with the reaction rates near the neutrino sphere, the region most important for the formation of neutrino signals as observed. Now we shift our interest to a deeper region with the highest temperature, where muons are expected to be most abundant. The results are presented in Figure 3.2.

Panel (a) shows the inverse mean free paths for ν_e. The absorption on neutron is the most important source of opacity in all range of the incident neutrino energy as expected. Since the temperature in model t10D is much higher than that of model t10S, the Fermi blocking by electron is more moderate, which is the reason why the CC reaction remains dominant even at low energies. The nucleon scatterings are the second dominant just as for model t10S (Figure 3.1(a)). Note that the scattering on proton is much larger compared with model t10S because the free proton is much more abundant in this region ($Y_p = 0.22$) than around the neutrino sphere.

The opacities of the scatterings on neutron, electron and muon are larger by an order than the counterparts in model t10S, since the scattered particles are more numerous. The flavor exchange reaction $\nu_e + \mu^- \to \nu_\mu + e^-$ is also enhanced compared with model t10S for the same reason. It is still minor than the CC reaction partly because the chemical potential of muon is overwhelmed by that of electron, which results in a smaller phase space available in the flavor exchange reaction whereas in the CC reaction the difference in the effective potentials between neutron and proton are significant. As I mentioned, since the Fermi blocking by leptons is weaker in this region, the electron-positron and muon-anti-muon pair processes are allowed even at lower neutrino energies. The three body reactions are very minor as in model t10S.

For $\bar{\nu}_e$, the inverse neutron decay is strongly enhanced and is dominant indeed in the energy range of $E_{\bar{\nu}_e} \lesssim 20\,\mathrm{MeV}$. This happens because the proton number density as well as the potential difference between proton and neutron are larger in model t10D. The latter broadens the available phase space. The inverse muon decay is not so large, but is still greater compared with model t10S. This is because the electron number density is larger and the inequality $\mu_{e^-} > \mu_{\mu^-}$ is satisfied for the chemical potentials at this radius while the opposite inequality $\mu_{e^-} < \mu_{\mu^-}$ holds near the neutrino sphere. The flavor exchange reaction $\bar{\nu}_e + e^- \to \bar{\nu}_\mu + \mu^-$ is also enhanced from model t10S in the same way as the

inverse muon decay is. The energy threshold for the absorption via the charged current is determined by the potential difference between neutron and proton as in model t10S. The features of other reactions are common to ν_e.

Panel (c) shows the results for ν_μ. The neutrino capture on neutron is the greatest source of opacity in a wider energy range $E_{\nu_\mu} \gtrsim 10\,\mathrm{MeV}$ compared with model t10S due to the larger potential difference between neutron and proton. The scattering on neutron gives the dominant contribution at $E_{\nu_\mu} \lesssim 10\,\mathrm{MeV}$. The flavor exchange reaction $\nu_\mu + e^- \to \nu_e + \mu^-$ and the inverse muon decay are subdominant compared with the scattering and absorption on neutron but are larger than those in model t10S. The reason is similar to the muon-related reaction for $\bar{\nu}_e$; the electron is more abundant and the chemical potential difference between electron and muon favors these reactions. The scattering on electron and muon and the pair-processes are minor just as for ν_e and $\bar{\nu}_e$.

For $\bar{\nu}_\mu$, the scattering on neutron gives the dominant contribution except at $2\,\mathrm{MeV} \lesssim E_{\bar{\nu}_\mu}$, where the flavor exchange reaction $\bar{\nu}_\mu + \mu^- \to \bar{\nu}_e + e^-$ is the largest contributor, which is similar to model t10S (see panel (d)). The reaction rate in model t10D, on the other hand, is larger by an order than that in model t10S because the number density of muon is larger by the same factor. In the similar way, the neutrino capture on proton is enhanced at high energies, since the proton number fraction is greater by an order again compared with model t10S, while the potential difference between proton and neutron prevents the reaction at low energies. Three body reaction $\bar{\nu}_\mu + e^+ + \nu_e \to \mu^+$ is strongly suppressed as positrons are scarce. It is mentioned for model t10S that the μ-type (anti-)neutrino scattering on muon is comparable with or higher than that on electron which is also confirmed in model t10D.

The scattering on neutron is again the dominant source of opacity for the τ-type neutrino (panel (e)). The scattering on proton is smaller owing to the smaller abundance proton. As pointed out in model t10S, the opacity of $\bar{\nu}_\tau$ is always smaller than ν_τ for all reactions and at all energies.

3.2.2 Corrections in semi-leptonic reactions

In the evaluation of rates for the semi-leptonic reactions, I include the mean field effect (MF), the weak magnetism (WM), the q^2 dependence of form factors and the pseudoscalar (PS) term. Here I pay attention to the differences that they make in the CC and NC reactions.

neutrino capture on neutron

Figure 3.3 summarizes the results for the CC reactions of ν_e and ν_μ in model t10S. The label "Full" (blue line) means that all corrections WM, PS, MF and the q^2 dependence of form factors are included; the orange line incorporates only WM, PS and MF; the green dotted line excludes PS further; the red dashed line includes only MF; the purple line corresponds to no corrections at all. The brown line shows the approximated rates given by Bruenn Bruenn (1985), in which they assume that the momentum transfer of the nucleon is approximately zero and the nucleon mass is infinitely large. I include the MF effect in the Bruenn approximation which is expressed as

$$\frac{1}{\lambda(E_1)} = \frac{G_F^2 \cos^2\theta_C}{\pi}\left(g_V^2 + 3g_A^2\right) p_3 E_3 \left[1 - f_3(E_3)\right] \frac{n_2 - n_4}{1 - \exp\left[\beta\left(-\mu_2 + \mu_4\right)\right]}, \tag{3.77}$$

where $E_3 = E_1 + U_2 - U_4 + m_2^* - m_4^*$, $p_3 = \sqrt{E_3^2 - m_3^2}$ and n_2 and n_4 are number densities of N_2 and N_4, respectively. I define the relative deviation of the inverse mean free path

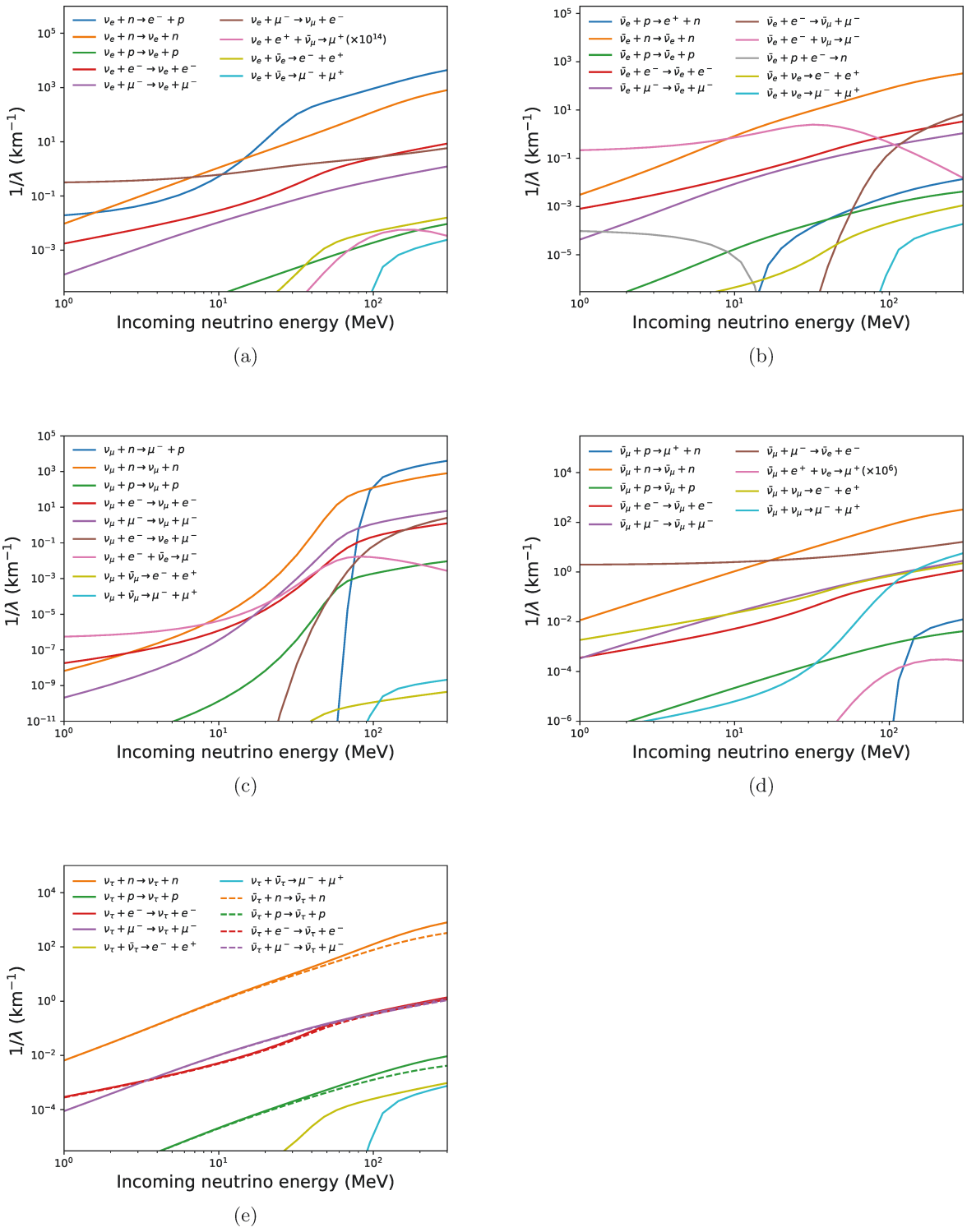

Figure 3.1: Inverse mean free paths for different neutrino flavors in model t10S. Panels (a), (b), (c) and (d) are the results for ν_e, $\bar{\nu}_e$, ν_μ and $\bar{\nu}_\mu$, respectively. Panel (e) shows those for both ν_τ and $\bar{\nu}_\tau$ where the solid and dashed lines are for ν_τ and $\bar{\nu}_\tau$, respectively. Colors denote the different reactions written in the legends in each panel. Note that the values for $\nu_e + e^+ + \bar{\nu}_\mu \to \mu^+$ in panel (a) are multiplies by 10^{14}. Note also that the values for $\bar{\nu}_\mu + e^+ + \nu_e \to \mu^+$ are multiplied by 10^6.

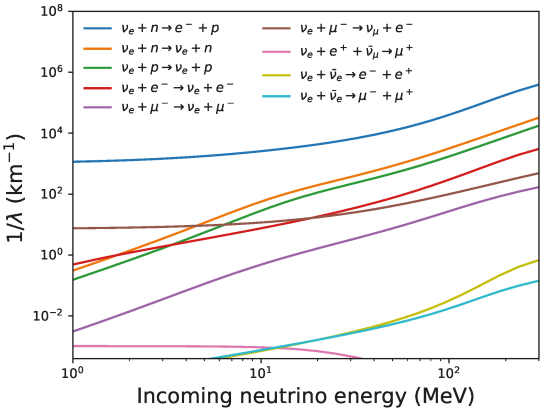

(a)

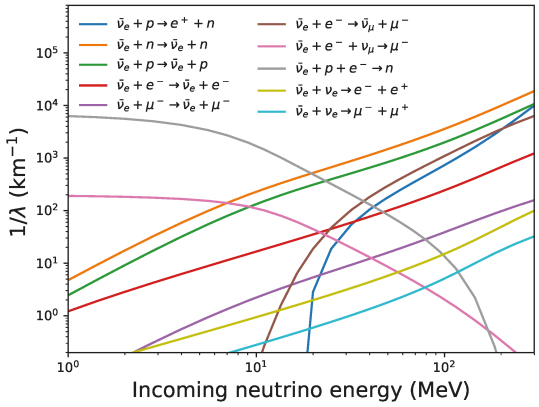

(b)

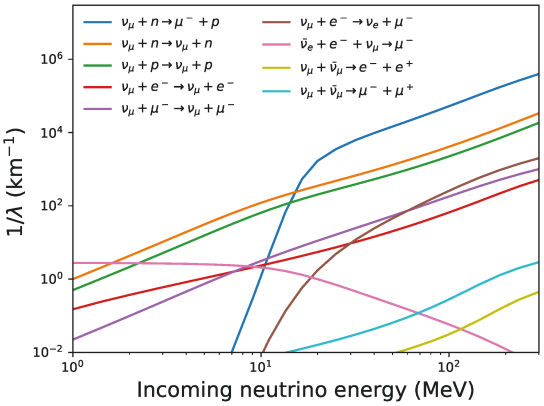

(c)

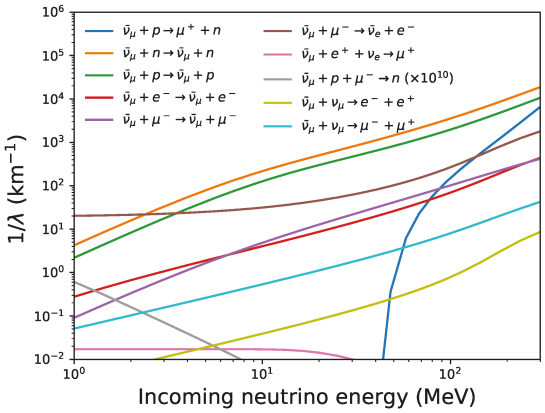

(d)

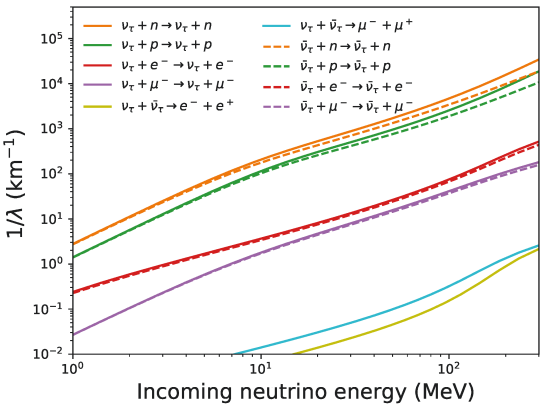

(e)

Figure 3.2: Same as Figure 3.1 but for model t10D. Note that the values for $\bar{\nu}_\mu + p + \mu^- \to n$ are multiplied by 10^{10}.

for each approximation from the complete one as follows:

$$\delta_i = \frac{1/\lambda_i - 1/\lambda_{\rm full}}{1/\lambda_{\rm full}}. \tag{3.78}$$

It is obvious that the purple solid line is deviated from all the others substantially. This is due to the mean field effect as can be most clearly understood from the comparison with the red dashed line. It is clear that the absorptivity is enhanced in general. This happens for ν_e (panel (a)) because the energy that the produced electron gains becomes greater by the mean field potential difference between proton and neutron and, as a result, the final-state Fermi-blocking of electron is suppressed Martínez-Pinedo et al. (2012). For ν_μ (panel (b)), the reason is essentially the same but the muon rest mass gives the threshold at a higher energy.

We can see how the approximation given by Bruenn Bruenn (1985) behaves by comparing the brown and red dashed lines. In both ν_e and ν_μ capture on neutron, the approximated rates are always larger than the case with full kinematics. The differences between them depends on the incoming neutrino energies: $\sim 20\%$ in $E_\nu \lesssim 30\,\mathrm{MeV}$ and $\sim 30\%$ at $E_\nu = 100\,\mathrm{MeV}$. Note that in ν_μ capture on neutron, the reaction cannot be occurred when the incoming neutrino is $E_\nu < m_\mu - (U_n - U_p)$ in the approximated rate.

The effect of the weak magnetism can be seen from the comparison between the red dashed line and the green dotted line. It tends to enhance the absorptivity, the degree of which depends on the momentum transfer q/M: $\sim 10\%$ at $E_\nu \sim 10\,\mathrm{MeV}$ and $\sim 30\%$ at $E_\nu \sim 100\,\mathrm{MeV}$ for ν_e whereas for $\nu_\mu \sim 20\%$ at $E_\nu \sim 100\,\mathrm{MeV}$ as shown at the bottom of each panel. The difference between the green dotted line and the orange dash-dotted line reflects the effects of pseudoscalar term. Since it is proportional to $m_l^2 \ll M^2$ in the matrix elements, the changes that this term induces are rather small both for ν_e and ν_μ.

The effects of the q^2 dependence of form factors are encoded in the difference between the blue solid line and the orange dash-dotted line. The absorptivity is reduced in general by the inclusion of the dependence and the reduction is larger for higher neutrino energies, scaling with q^2/M^2. This correction reaches $\sim 10\%$ and $\sim 5\%$ at $\sim 100\,\mathrm{MeV}$ for ν_e and ν_μ, respectively.

neutrino nucleon scattering

Now we shift our interest to the NC reaction. Figure 3.4(a) shows the effects of the corrections on the neutrino scattering on neutron in model t10D. The effect of MF can be seen from the comparison between the purple solid lines and the red dashed lines, in which the nucleon mass is set to the vacuum value in the former while it is given the effective mass in the latter, respectively. Note that there is no potential difference in the NC reactions. In the calculation of the dynamical structure functions of nucleons, the integration ranges that appear in the Fermi integral (for example see . Eq. (B.24)) strongly depend on the effective mass. In fact, for the NC reaction, in which $\kappa = 1$, $\tilde{q}^0 = q^0$ and $\Delta^2 = \left(q^0\right)^2 - q^2 < 0$ are satisfied, the integration range (see Eqs. (B.25) and (B.26)) becomes

$$E_{\rm min} = \max\left\{m_2^*, m_4^* - \tilde{q}^0, E_{2,+}^*\right\},\ E_{\rm max} = \infty, \tag{3.79}$$

where $E_{2,+}^*$ is given as

$$E_{2,+}^* = -\frac{q^0}{2} + \frac{|q|}{2}\sqrt{1 - \frac{4m_2^{*2}}{\Delta^2}}. \tag{3.80}$$

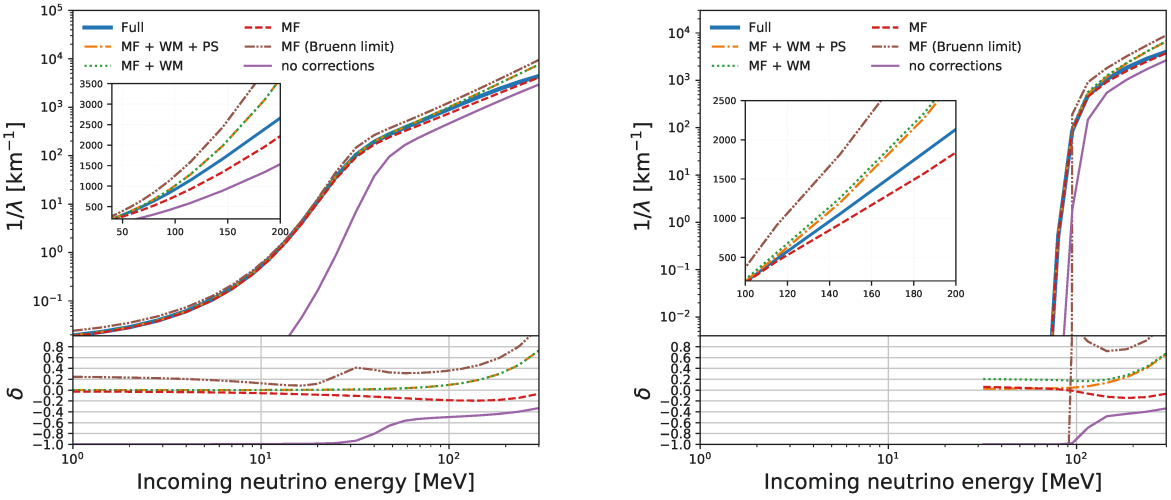

Figure 3.3: Inverse mean free paths for $\nu_e + n \to e^- + p$ (panel (a)) and $\nu_\mu + n \to \mu^- + p$ (panel (b)) with and without some corrections to the charged currents of nucleons for model t10S. The label "Full" (blue line) means that all corrections WM, PS, MF and the q^2 dependence of form factors are included; the orange line incorporates only WM, PS and MF; the green dotted line excludes PS further; the red dashed line includes only MF; the purple line corresponds to no corrections at all. The brown line shows the approximated rate given by Bruenn Bruenn (1985) with the MF being included. The relative differences are shown at the bottom of each panel. The insets are the zoom-in on high energy ranges.

Since the effective mass of nucleon, m^*, in the dense region is substantially smaller than the vacuum mass, the integration ranges are wider in general. This is the reason why the inverse mean free paths are enhanced by including the effective mass.

The brown line shows the approximation given by Bruenn Bruenn (1985) as follows:

$$\frac{1}{\lambda(E_1)} = \int \frac{d^3\boldsymbol{p}_3}{(2\pi)^3} \left[1 - f_3(E_3)\right] R_{\rm Bruenn}, \tag{3.81}$$

with the reaction kernel

$$\begin{aligned} R_{\rm Bruenn} &= 2\pi G_F^2 \eta_{\rm NN} \delta(E_1 - E_3) \\ &\times \left\{ (G_1^N(0))^2 + 3(G_A^N(0))^2 + \left[(G_1^N(0))^2 - (G_A^N(0))^2 \right] \cos\theta \right\}, \end{aligned} \tag{3.82}$$

where θ is an angle between incoming and outgoing neutrinos and $\eta_{\rm NN}$ is defined as

$$\eta_{NN} = \int \frac{2d^3\boldsymbol{p}_N}{(2\pi)^3} f_N(E_N^*) \left[1 - f_N(E_N^*)\right]. \tag{3.83}$$

By comparing with red dashed lines, the approximated rate is larger than that including full kinematics for higher energies $E_\nu \gtrsim 70\,\mathrm{MeV}$ and $E_\nu \gtrsim 40\,\mathrm{MeV}$ for ν_e and $\bar{\nu}_e$, respectively. On the other hand for lower energies, the rate including full kinematics is larger by an order than the approximated, so I can say that the momentum transfer gives great influences in the deeper region where the effective mass is reduced.

The WM correction gives opposite modifications for neutrino and anti-neutrino (compare the green and red lines in panels (a) and (b): it tends to enhance (suppresses) the reaction for neutrino (anti-neutrino). The degrees of change are a few % at $E_\nu \sim 10\,\mathrm{MeV}$ and $\sim 10\%$ at $E_\nu \sim 100\,\mathrm{MeV}$ in both cases. These results are qualitatively consistent with those of the previous study Horowitz (2002).

The q^2 dependence of form factors reduces the inverse mean free paths just as the CC reactions do. The relative difference it makes is a few percent around $E_\nu \sim 10\,\mathrm{MeV}$ and reaches a few tens percent at $E_\nu = 300\,\mathrm{MeV}$.

Note in passing that the NC reactions do not distinguish the neutrino flavors except their distribution functions, the results mentioned above for the e-type neutrino and anti-neutrino are applied also to other flavors of neutrinos and anti-neutrinos.

3.2.3 Inverse mean free paths at other times

I move on to the results for other thermodynamical conditions obtained at $t = 1, 3\,\mathrm{s}$ (the earlier phase) and $t = 30, 50\,\mathrm{s}$ (the later phase) to infer the time evolutions of the mean free paths in the PNS cooling.

The inverse mean free paths for ν_e at the neutrino sphere are shown in Figure 3.5. Comparing them with Figure 3.1(a), one finds that the neutrino capture on neutron is enhanced at later times. This is due to the widening of the effective potential difference between neutron and proton $U_n - U_p$ as well as to the increase in the number density of neutron. The inverse mean free paths for the neutrino scattering on neutron and the flavor exchange reaction also rise as the density at the neutrino sphere increases in time. The scattering on proton, on the other hand, gets strongly suppressed at later times due to the declining proton fraction at the neutrino sphere. As the temperature lowers, the pair production reactions are suppressed at low energies as I mentioned in Figure 3.2.

Figure 3.6 is the same as Figure 3.5 but for the deeper region, where the temperature becomes maximum. Note that the radius changes in time (see Table 3.5). The inverse

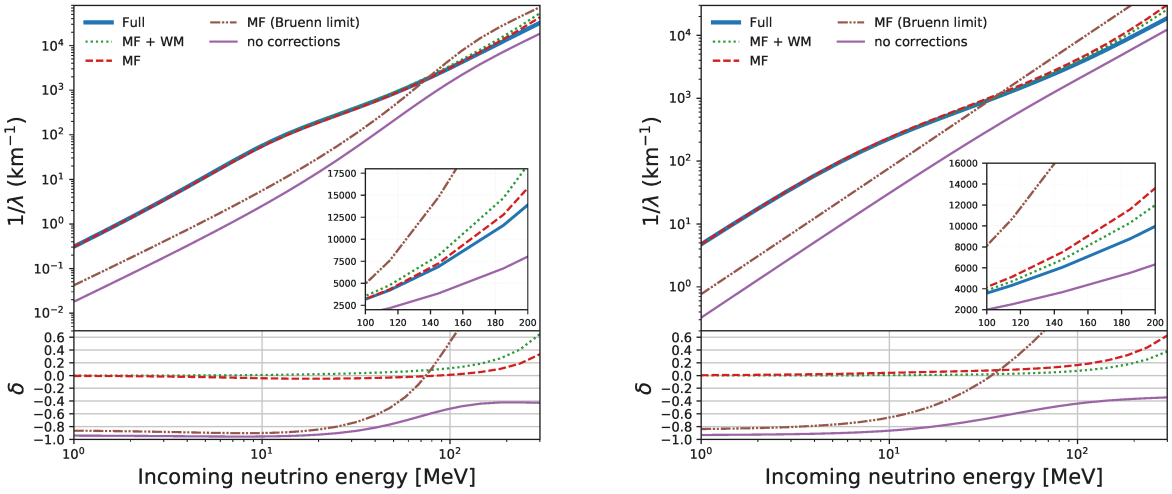

(a) (b)

Figure 3.4: Inverse mean free paths of the neutrino scattering on neutron for ν_e (panel (a)) and $\bar{\nu}_e$ (panel (b)) with and without some corrections to the neutral currents of nucleons ofr model t10D. The label "Full" (blue line) means that all corrections WM, MF and the q^2 dependence of form factors are included; the green dotted line incorporates only WM and MF; the red dashed line includes only MF; the purple line corresponds to no corrections at all. The brown line shows the approximated rate given by Bruenn Bruenn (1985) with the MF being included. The relative differences are shown at the bottom of each panel. The insets are the zoom-in on high energy ranges.

mean free paths of the neutrino capture on neutron is the dominant source of opacity in all times, but it drastically decreases at $t = 50\,\mathrm{s}$. This is because the Fermi blocking by electron at $E_\nu \lesssim \mu_e - (U_n - U_p)$ is more effective. This applies also to the suppression of the flavor exchange reaction at $t = 50\,\mathrm{s}$. On the other hand, the decline of the neutrino scatterings on nucleon at $t = 50\,\mathrm{s}$ is due to the strong Fermi blocking by ν_e, the Fermi energy of which is $\mu_{\nu_e} = \mu_p + \mu_e - \mu_n \simeq 100\,\mathrm{MeV}$.

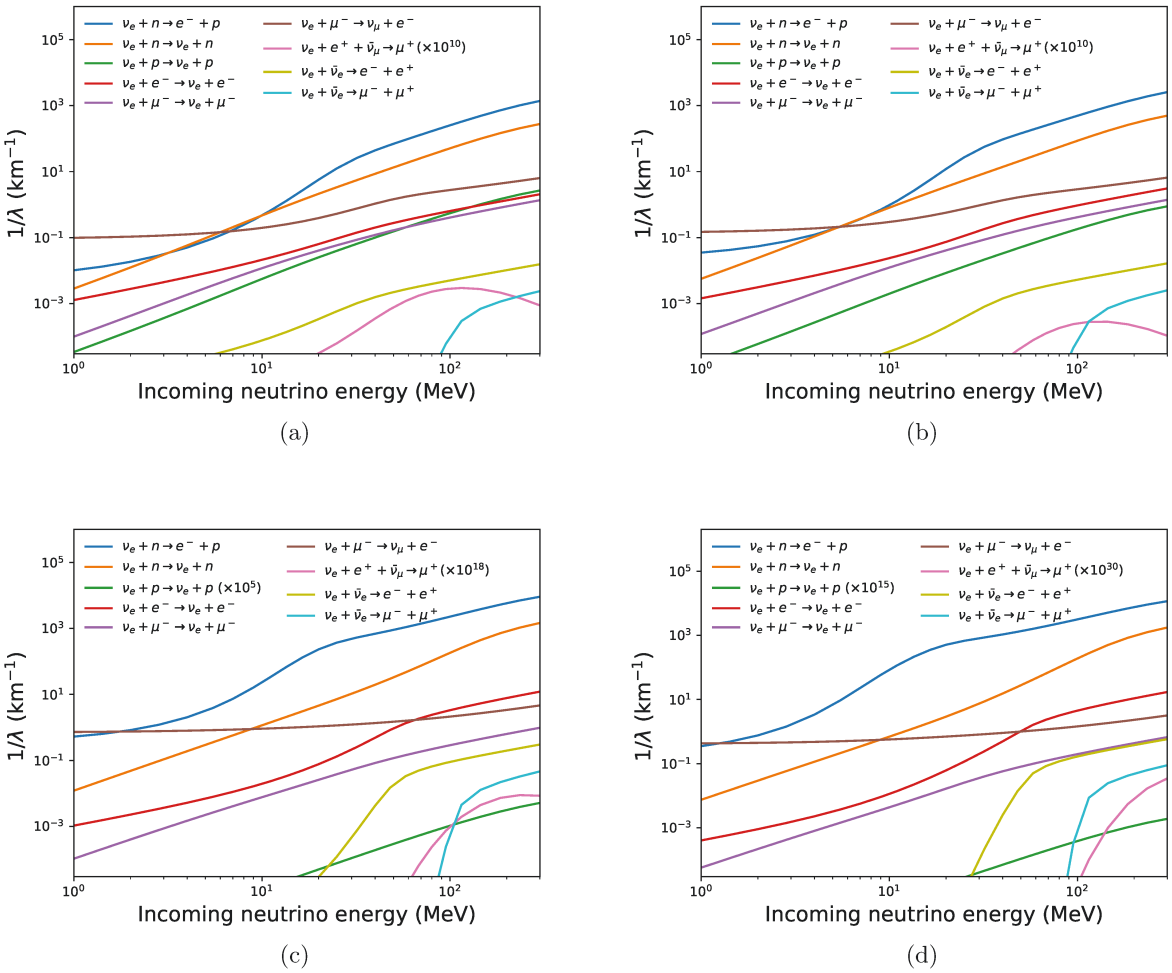

Figure 3.5: Inverse mean free paths for ν_e at different times. Panel (a): $t = 1\,\mathrm{s}$ (model t1S); Panel (b): $t = 3\,\mathrm{s}$ (model t3S); Panel (c): $t = 30\,\mathrm{s}$ (model t30S); Panel (d): $t = 50\,\mathrm{s}$ (model t50S). Colors denote different reactions. Note that the values for $\nu_e + e^+ + \bar{\nu}_\mu \to \mu^+$ are multiplied by the factors given in the legend in each panel.

Figures 3.7 and 3.8 are the inverse mean free paths for $\bar{\nu}_e$ at the neutrino sphere and at the deeper region, respectively, and the four panels in each figure correspond to different times as in Figures 3.5 and 3.6. These results have similar features as those for models t10S and t10D at $t = 10\,\mathrm{s}$. At low energies, the inverse muon decay is dominant at the neutrino sphere, and is second dominant at the deeper region. In model t50S (see panel 3.7(d)), however, its rate is strongly suppressed due to the Fermi blocking by muon. In the deeper region, the inverse neutron decay is dominant at low energies in all phases just as in model t10D. The neutrino capture on proton is strongly suppressed due to the effective potential difference between neutron and proton also as in models t10S and t10D. The neutrino

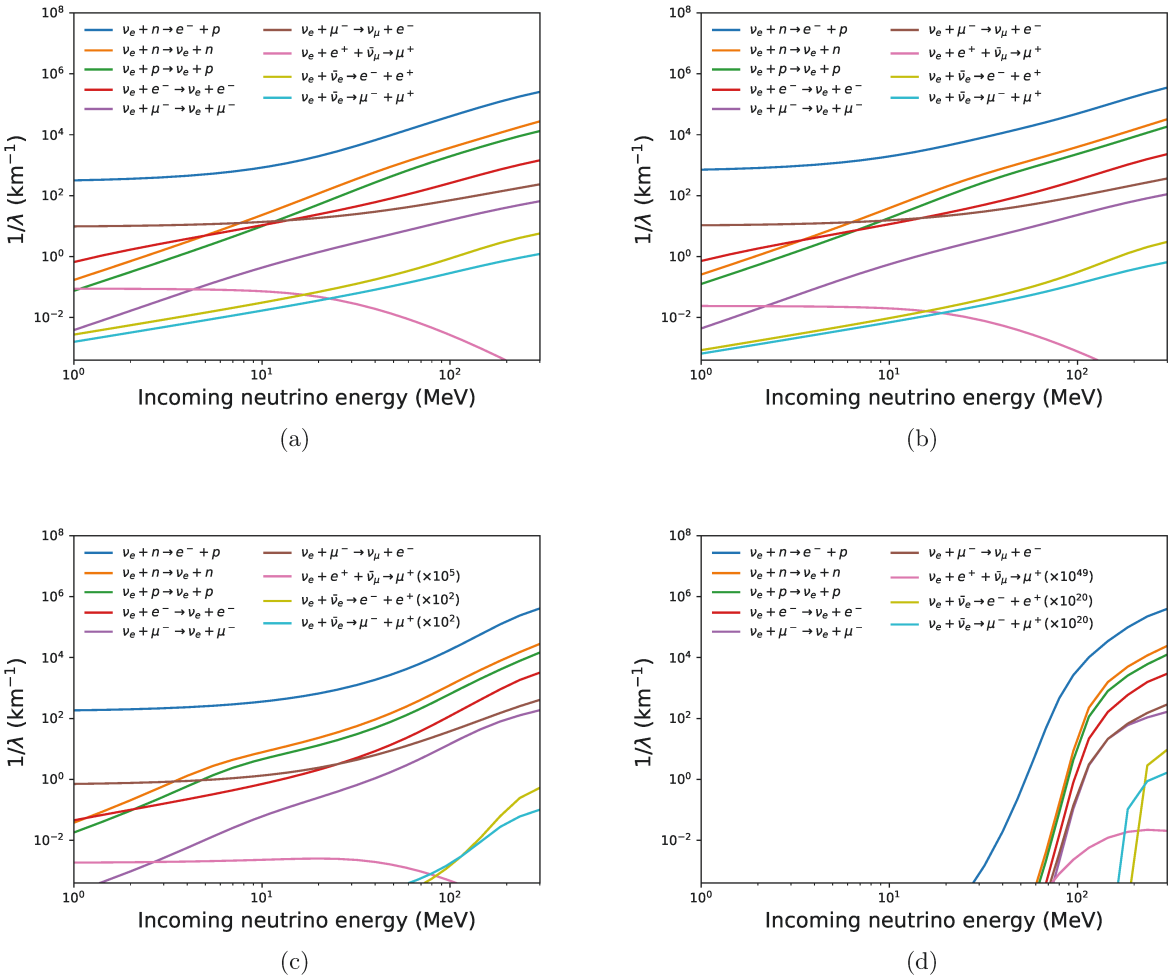

Figure 3.6: Same as Figure 3.5 but for the deeper regions. Panel (a): $t = 1\,\mathrm{s}$ (model t1D); Panel (b): $t = 3\,\mathrm{s}$ (model t3D); Panel (c): $t = 30\,\mathrm{s}$ (model t30D); Panel (d): $t = 50\,\mathrm{s}$ (model t50D). Colors denote different reactions. Note that the values for $\nu_e + e^+ + \bar{\nu}_\mu \to \mu^+$ and the pair production reactions in models t30D and t50D are multiplied by the factors given in the legend in each panel.

scattering on neutron is the dominant source of opacity at high neutrino energies, which is also similar to the result at $t = 10\,\mathrm{s}$. The inverse mean free paths of the scatterings at $t = 50\,\mathrm{s}$ are smaller by an order compared with those at $t = 30\,\mathrm{s}$ because the temperature decreases by an order. Note that J_i's that appear in the dynamical structure functions (Eqs. (B.32)-(B.34)) are proportional to T^{i+1}.

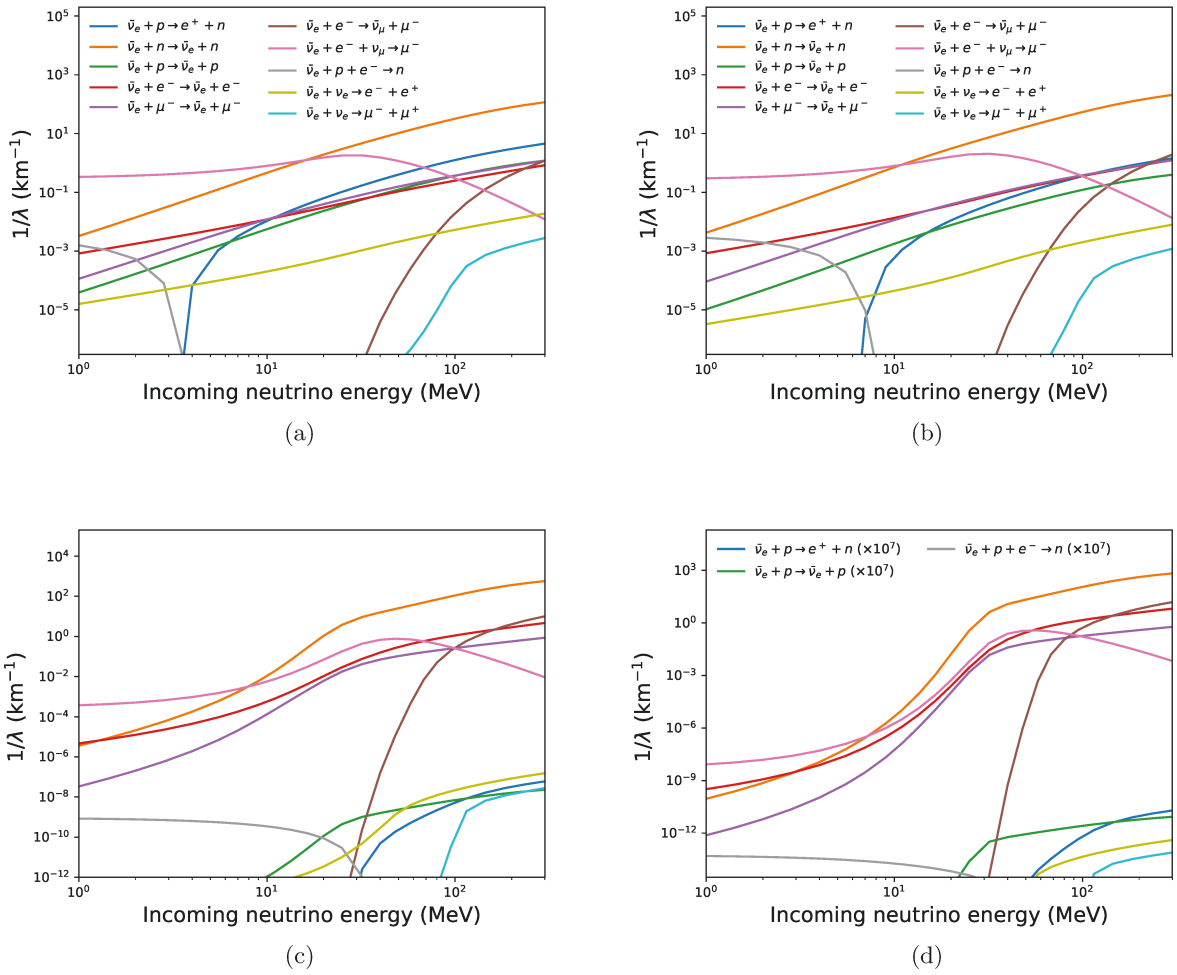

Figure 3.7: Same as Figure 3.5 but for $\bar{\nu}_e$. Colors denote the different reactions. The legends are omitted in panels (c) and (d) for visibility but the notations are the same as in panel (a). Note that the values for $\bar{\nu}_e + p \to e^+ + n$, $\bar{\nu}_e + p \to \bar{\nu}_e + p$ and $\bar{\nu}_e + p + e^- \to n$ in panel (d) are multiplied by 10^7.

The results for ν_μ are exhibited in Figures 3.9 and 3.10. At the neutrino sphere (see Figure 3.9), the time evolutions of the inverse mean free paths are not so remarkable: the inverse muon decay, the neutrino scattering on neutron and the neutrino absorption on neutron are the dominant sources of opacity at low, middle and high neutrino energies, respectively. However, in the deeper region at the later phase, the inverse muon decay $\nu_\mu + e^- + \bar{\nu}_e \to \mu^-$ remains subdominant even at low neutrino energies because the number density of $\bar{\nu}_e$ declines due to large negative values of $\mu_{\bar{\nu}_e}$ in β-equilibrium.

Finally, figures 3.11 and 3.12 present the inverse mean free paths for $\bar{\nu}_\mu$. At the neutrino sphere, the neutrino scattering on neutron and the flavor exchange reaction $\bar{\nu}_\mu + \mu^- \to \bar{\nu}_e + e^-$ are the dominant sources of opacity at high and low energies, respectively. The

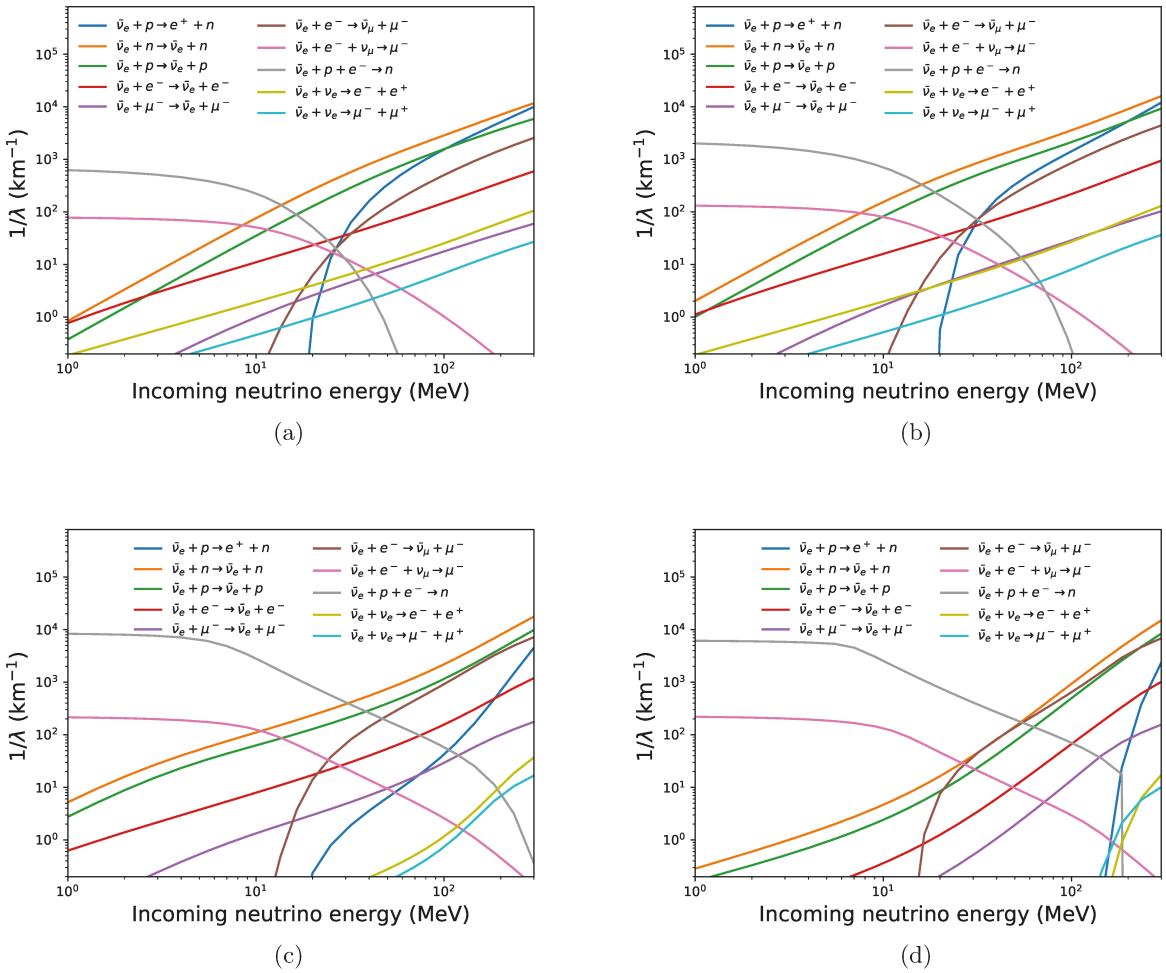

Figure 3.8: Same as Figure 3.6 but for $\bar{\nu}_e$. Colors denote different reactions.

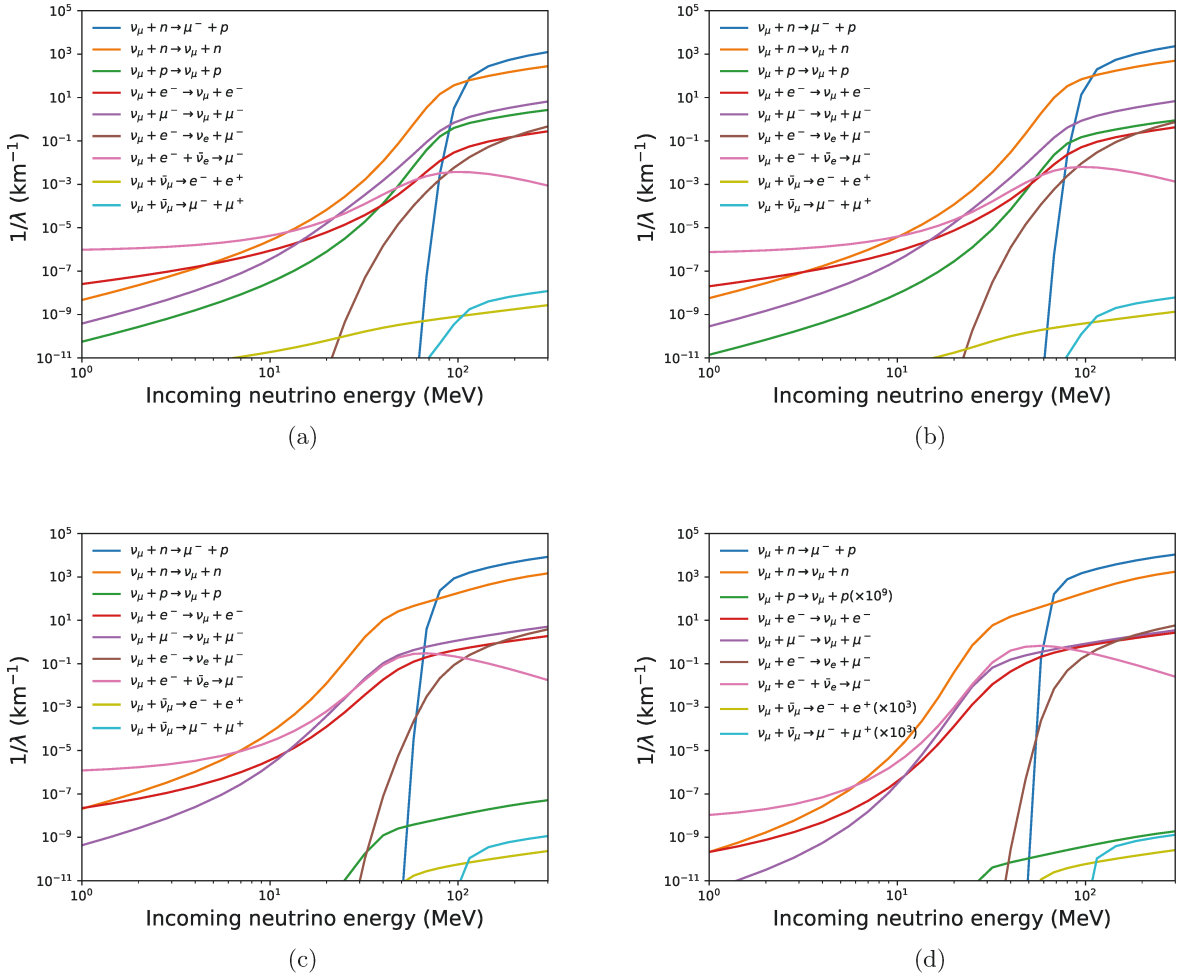

Figure 3.9: Same as Figure 3.5 but for ν_μ. Colors denote different reactions. Not that the values of the pair production reactions in panel (d) are multiplied by 10^3.

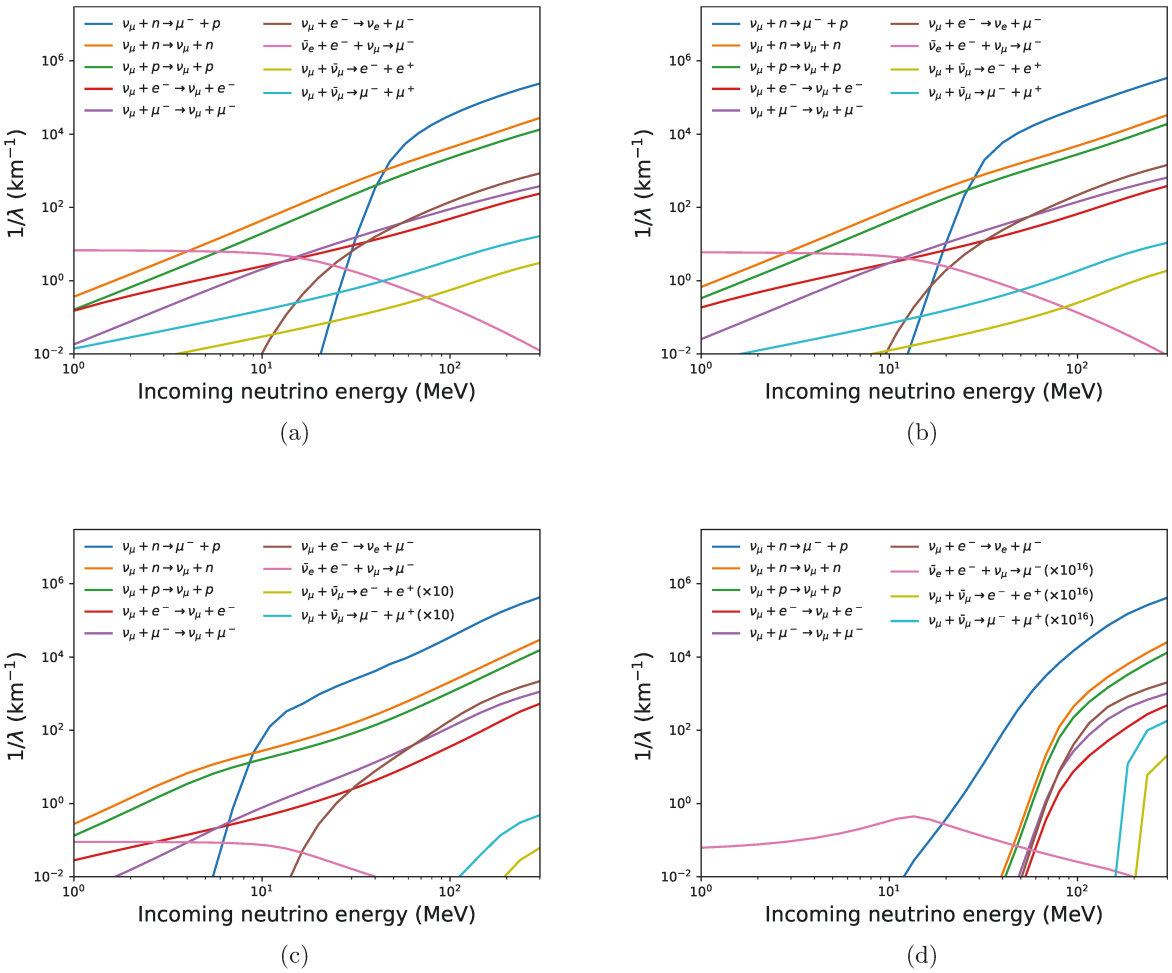

Figure 3.10: Same as Figure 3.6 but for ν_μ. Colors denote different reactions. Note that the values for $\nu_\mu + e^- + \bar{\nu}_e \to \mu^-$ and the pair production reactions in panels (c) and (d) are multiplied by the factors given in the legend in each panel.

electron-positron pair production comes next except at very high energies, where muon-anti-muon production takes its place in the earlier phase because the incoming neutrino energy is so high that muons can be produced, but gets suppressed in the later phase due to the strong Fermi blocking by electron and muon at low temperatures. In the deeper region, the flavor exchange reaction is dominant at low energies in the early phase just as in model t10D, while it is suppressed in the later phase (especially in Model t50D) because the temperature is so low that the Fermi blocking by muon cannot be overcome. In these conditions, the scattering on proton is the second dominant reaction.

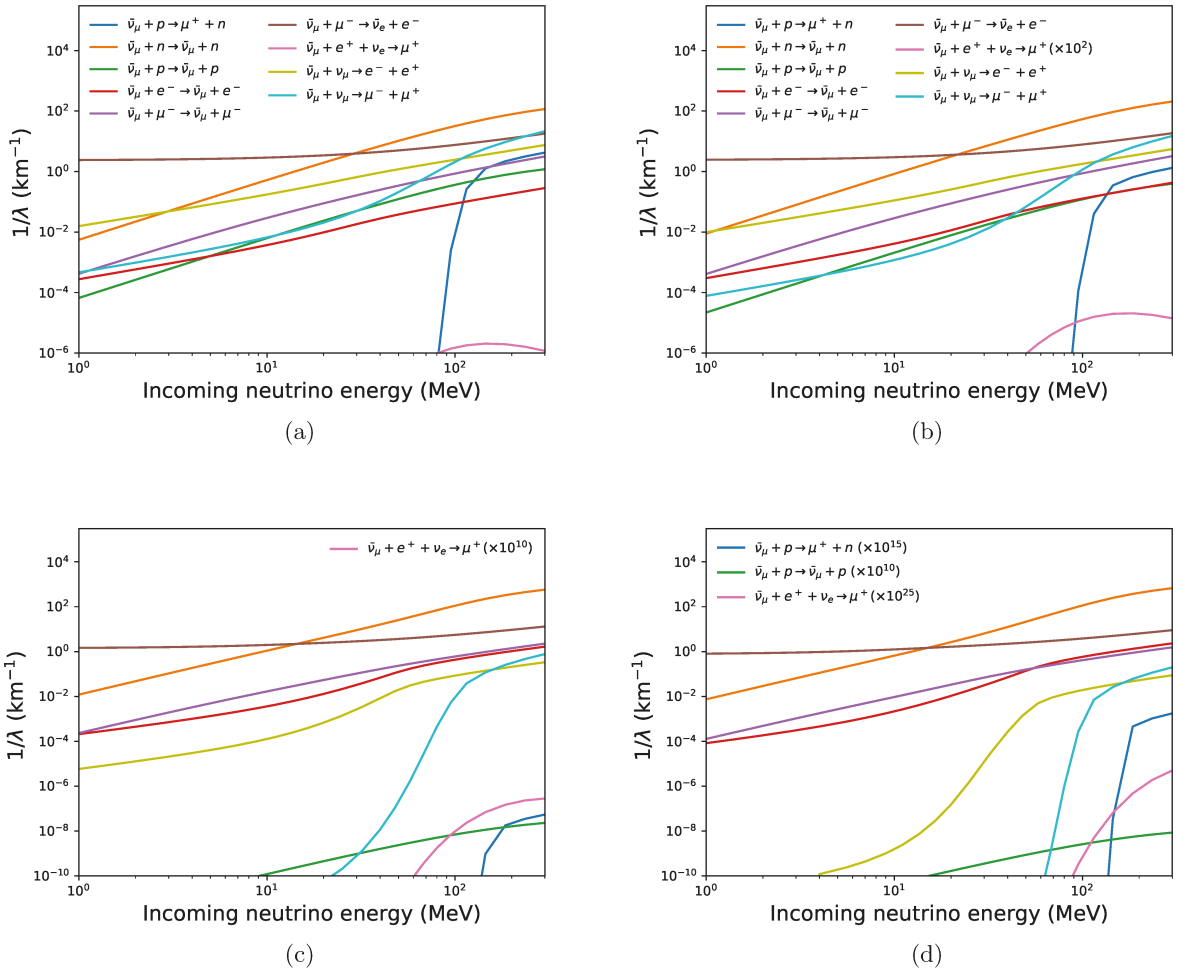

Figure 3.11: Same as Figure 3.5 but for $\bar{\nu}_\mu$. Colors denote different reactions. The legends are omitted in panels (c) and (d) but the notations are the same as in panel (a). Note that the values for $\bar{\nu}_\mu + p \to \mu^+ + n$ and the scattering on proton in panel (d) and $\bar{\nu}_\mu + e^+ + \nu_e \to \mu^+$ in panels (b), (c) and (d) are multiplied by the factors given in the legend in each panel.

Before closing this subsection, I give a brief comment on the comparison with the previous work Guo et al. (2020), which focused on the muonization of matter and the muon-related reactions of $\bar{\nu}_e$ and ν_μ in the very early phase of PNS cooling, or more appropriately the post-bounce phase of CCSNe. The thermal conditions in the earlier phase, especially for model t1D, are similar to condition A in Guo et al. (2020). Our results, Figures 3.8(a) and 3.10(a), are perfectly consistent with their results: condition

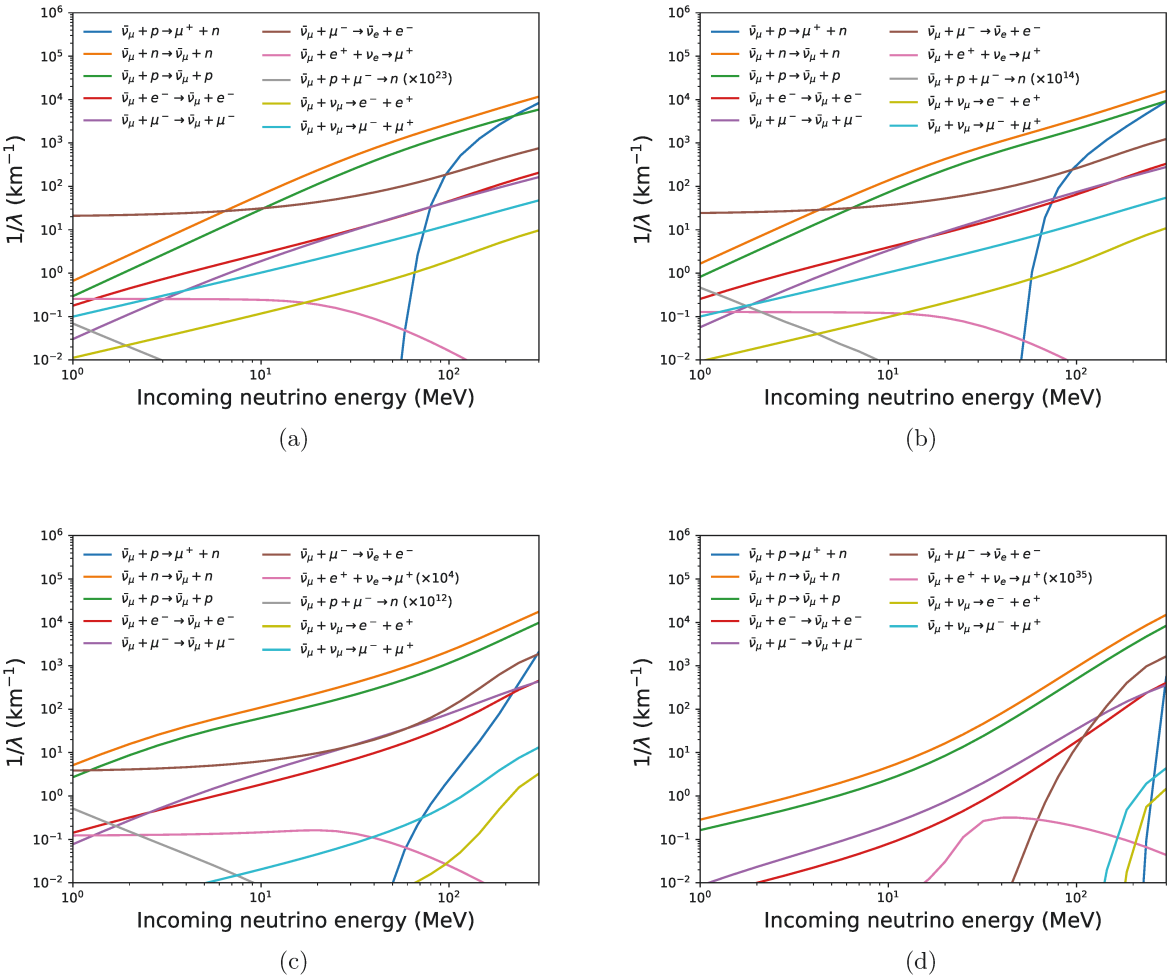

Figure 3.12: Same as Figure 3.6 but for $\bar{\nu}_\mu$. Colors denote different reactions. Note that the values for $\bar{\nu}_\mu + e^+ + \nu_e \to \mu^+$ and $\bar{\nu}_\mu + p + \mu^- \to n$ are multiplied by the factors given in the legends in each panel.

A in figures 5 and 6 in their paper except for minor deviations induced inevitably by the use of different EoS and the values of the mean field parameters. Condition B in Guo et al. (2020) is similar to our model t10S except that the temperature and the electron fraction in the latter are lower than those in the former due to the advanced cooling and neutronization in our model. The trends in the inverse mean free paths are qualitatively the same: for ν_μ, for example, the inverse muon decay and the neutrino scattering on neutron are dominant at low and high energies, respectively.

3.2.4 Reaction kernels of the flavor-exchange reaction and the inverse muon decay

So far I have looked at the inverse mean free path alone, the quantity integrated over the energy and angle. In this section I will look into more details, i.e., the energy- and angular dependences of the reaction kernels for some muon-related reactions that become significant as an opacity source at some energies: the flavor-exchange reaction $\nu_e + \mu^- \leftrightarrows \nu_\mu + e^-$ and the inverse muon decay $\bar{\nu}_e + \nu_\mu + e^- \to \mu^-$. I show the results at $t = 10\,\mathrm{s}$. These are relevant information for detailed neutrino transport calculations but have not been presented so far.

Figure 3.13 exhibits as a color contour the reaction kernel $R^{\mathrm{in}}_{\nu_e}$ for the flavor exchange reaction, $\nu_e + \mu^- \to \nu_\mu + e^-$, as a function of the energy and the angle of the outgoing ν_μ with the energy of the incoming ν_e being fixed. The angle is measured from the flight direction of the incident ν_e. The upper panels (a), (b) and (c) are the results for model t10S while panels (d), (e) and (f) are for model t10D. The energy of the incoming ν_e is set to 1, 10 and 100 MeV for the left, middle and right columns, respectively.

It is observed that the energy of ν_μ is larger than the energy of ν_e thanks to the large difference of the rest masses between muon and electron. It is also clear that ν_μ is preferentially emitted in the forward direction irrespective of the incident energy of ν_e. As the energy ν_e gets larger, the forward peak becomes more remarkable whereas the energy gain gets smaller. From the comparison between models t10S and t10D, I find that these features are shared not only qualitatively but also quantitatively although the thermodynamic conditions are fairly different and the energy of ν_μ, at which the kernel attains the maximum, is somewhat different. Since this is true also for the other reactions, I will focus on model t10S in the following.

Figure 3.14 presents the reaction kernel $R^{\mathrm{in}}_{\nu_\mu}\left(= R^{\mathrm{out}}_{\nu_e}\right)$ for the inverse process of the flavor-exchange reaction discussed above: $\nu_\mu + e^- \to \nu_e + \mu^-$. This time the energy of the incident ν_μ is fixed to 1, 10 and 100 MeV in panels (a), (b) and (c), respectively, and the reaction kernel is regarded as a function of the energy and angle of the outgoing ν_e. For rather low incident energies (see panels (a) and (b)), the outgoing ν_e has very low energies, since most of the energy is exhausted to generate the muon mass. You can see again the outgoing neutrinos are emitted preferentially in the forward direction. For the high incident energy, the energy of outgoing neutrino rises accordingly and the forward peak gets pronounced. These results simply reflect the detailed balance expected as Eq. (3.10)

Now I move on to the reaction kernel for the inverse muon decay, $\bar{\nu}_e + \nu_\mu + e^- \to \mu^-$. Figure 3.15 shows $R^{\mathrm{in}}_{\bar{\nu}_e}$ as a function of the energy and angle of ν_μ with the energy of incoming $\bar{\nu}_e$ being fixed to either 1, 10 or 100 MeV (corresponding to panels (a), (b) and (c), respectively). The angle is measured from the flight direction of the other neutrino, $\bar{\nu}_e$. It is found that the kernel is largest when the sum of energies, $E_{\bar{\nu}_e} + E_{\nu_\mu}$ is close to the rest mass of muon and the neutrinos collide head on, i.e., $\cos\theta = -1$. When one looks at this reaction from the standpoint of ν_μ, on the other hand, the picture could

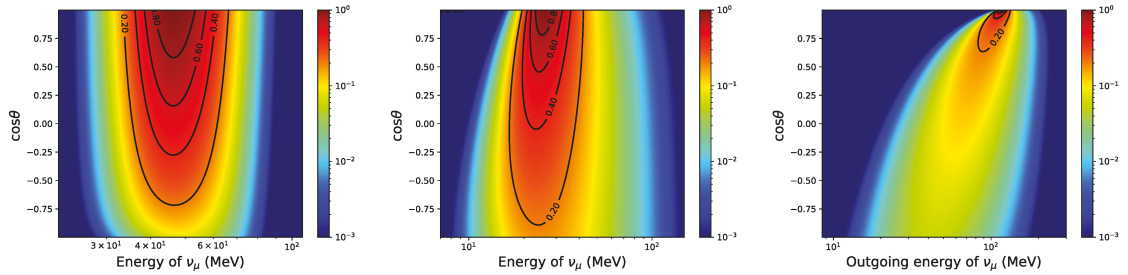

(a) $E_{\nu_e} = 1\,\mathrm{MeV}$ (b) $E_{\nu_e} = 10\,\mathrm{MeV}$ (c) $E_{\nu_e} = 100\,\mathrm{MeV}$

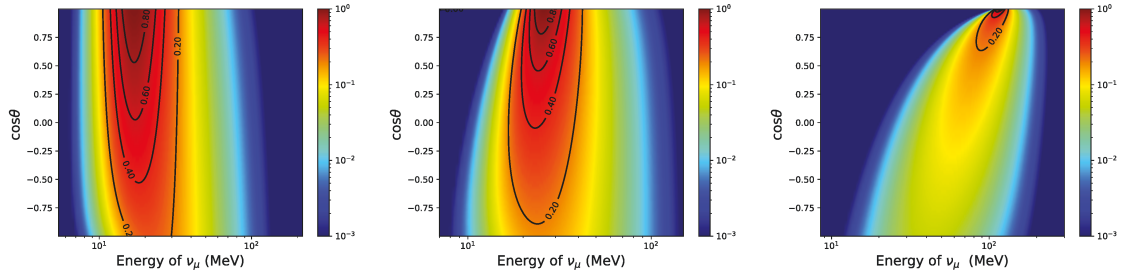

(d) $E_{\nu_e} = 1\,\mathrm{MeV}$ (e) $E_{\nu_e} = 10\,\mathrm{MeV}$ (f) $E_{\nu_e} = 100\,\mathrm{MeV}$

Figure 3.13: The reaction kernel $R^{\mathrm{in}}_{\nu_e}$ of the flavor-exchange reaction $\nu_e + \mu^- \to \nu_\mu + e^-$ for models t10S (panels (a), (b) and (c)) and t10D (panels (d), (e) and (f)) as a function of the energy and angle of outgoing ν_μ. The angle is measured from the flight direction of ν_e. The energy of ν_e is fixed to the value show in each panel. The value of the kernel is normalized by its maximum.

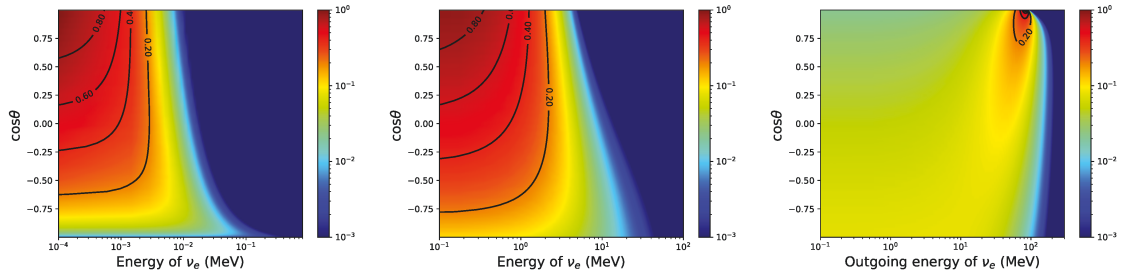

(a) $E_{\nu_\mu} = 1\,\mathrm{MeV}$ (b) $E_{\nu_\mu} = 10\,\mathrm{MeV}$ (c) $E_{\nu_\mu} = 100\,\mathrm{MeV}$

Figure 3.14: Same as Figure 3.13 but the kernel $R^{\mathrm{in}}_{\nu_\mu}$ for $\nu_\mu + e^- \to \nu_e + \mu^-$ as a function of the energy and angle of outgoing ν_e for model t10S.

be different. This can be seen in Figure 3.16, in which I display the same kernel as a function of the energy and angle of $\bar{\nu}_e$ for some fixed energies of ν_μ: 1, 10 or 100 MeV for panels (a), (b) and (c). For the low energy of 1 MeV (see panel (a)), the kernel reaches the maximum at $E_{\bar{\nu}_e} + E_{\nu_\mu} \approx m_\mu$ again but when the two neutrinos move in the same direction, i.e., $\cos\theta = 1$. As the incident energy becomes higher, however, the head-on collision is preferred again as is obvious in panels (b) and (c).

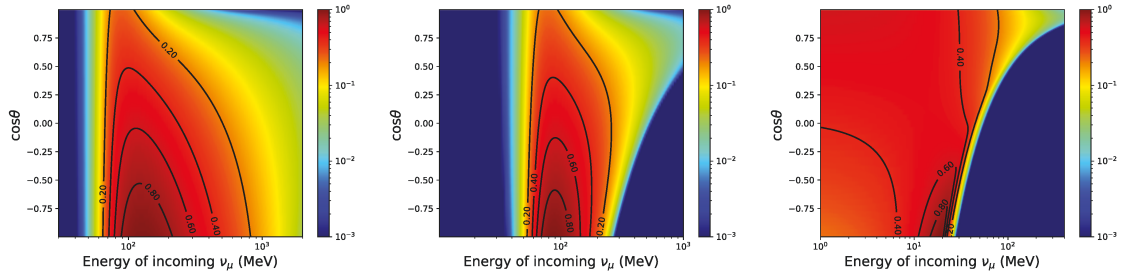

(a) $E_{\bar{\nu}_e} = 1\,\mathrm{MeV}$ (b) $E_{\bar{\nu}_e} = 10\,\mathrm{MeV}$ (c) $E_{\bar{\nu}_e} = 100\,\mathrm{MeV}$

Figure 3.15: The reaction kernel $R^{\mathrm{in}}_{\bar{\nu}_e}$ of the inverse muon decay $\bar{\nu}_e + \nu_\mu + e^- \to \mu^-$ for model t10S as a function of energy and angle of incoming ν_μ. The energy of $\bar{\nu}_e$ is fixed to $E_{\bar{\nu}_e} = 1, 10, 100\,\mathrm{MeV}$ for panels (a), (b) and (c), respectively. The values of the kernel is normalized by its maximum.

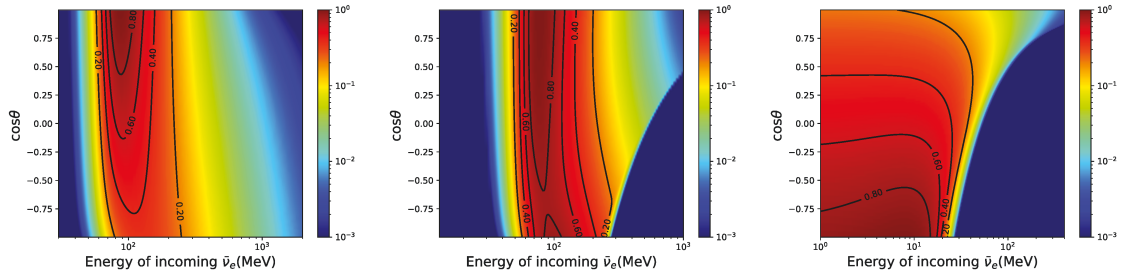

(a) $E_{\nu_\mu} = 1\,\mathrm{MeV}$ (b) $E_{\nu_\mu} = 10\,\mathrm{MeV}$ (c) $E_{\nu_\mu} = 100\,\mathrm{MeV}$

Figure 3.16: Same as Figure 3.15 but as a function of the energy and angle of incoming $\bar{\nu}_e$. The energy of ν_μ is fixed to $E_{\nu_\mu} = 1, 10, 100\,\mathrm{MeV}$ for panels (a), (b) and (c), respectively.

3.2.5 Implications for the cooling timescale

We have so far looked into the inverse mean free paths for individual reactions. What determines the thermal history of PNS is the sum of all these and inverse reactions as well as the advection of all species of neutrinos in the PNS. Except near the PNS surface, matter is so dense in the PNS interior that neutrinos are almost in thermal and chemical equilibria with matter. In such circumstances, each reaction is almost balanced with its inverse reaction. Then the neutrino distributions become nearly isotropic in momentum space and can be expanded as $f_\nu(\varepsilon, \cos\theta) = f_\nu^{(0)}(\varepsilon) + \cos\theta f_\nu^{(1)}(\varepsilon)$. This is nothing but the diffusion approximation, in which the energy flux of ν_i can be written as Pons et al.

(1999); Roberts and Reddy (2017b)

$$F_{\nu_i} = \frac{1}{6\pi^2}\int f^{(1)}_{\nu_i}(\varepsilon)\varepsilon^2 d\varepsilon$$
$$= -\frac{\Gamma T^3}{\alpha 6\pi^2}\left[D_{4,\nu_i}\frac{\partial \alpha T}{\partial r} + D_{3,\nu_i}(\alpha T)\frac{\partial \eta_{\nu_i}}{\partial r}\right], \tag{3.84}$$

where $\eta_{\nu_i} = \mu_{\nu_i}/T$, $\Gamma = \sqrt{1-2GM_g/r}$ and α is the lapse function, or the (00)-component of the metric. The diffusion coefficients in this expression are given as

$$D_{n,\nu_i} = \int_0^\infty d\varepsilon \frac{\varepsilon^n}{T^{n+1}}\frac{1}{\kappa^*_{\nu_i}} f^{(0)}_{\nu_i}(\varepsilon)\left[1 - f^{(0)}_{\nu_i}(\varepsilon)\right], \tag{3.85}$$

where $\kappa^*_{\nu_i}$ is the total absorption opacity defined as

$$\kappa^*_{\nu_i} = \frac{1}{\lambda^{\rm tot}_{\nu_i}} + j^{\rm tot}_{\nu_i}. \tag{3.86}$$

Since the second term in Eq. (3.84) is normally negligible in the PNS cooling Roberts and Reddy (2017b), the energy flux is reduced to

$$F_{\nu_i} \simeq -\frac{\Gamma T^3}{\alpha 6\pi^2} D_{4,\nu_i}\frac{\partial \alpha T}{\partial r}. \tag{3.87}$$

It is then obvious that the diffusion coefficient D_{4,ν_i} is the key factor to determine the cooling timescale through Eq. (1.12). I hence investigate this coefficient, in particular, the contribution of each reaction:

$$D^r_{4,\nu_i} = \int_0^\infty d\varepsilon \frac{\varepsilon^4}{T^5}\frac{1}{\kappa^r_{\nu_i}} f^{(0)}_{\nu_i}(\varepsilon)\left[1 - f^{(0)}_{\nu_i}(\varepsilon)\right], \tag{3.88}$$

where r specifies the reaction we consider and $\kappa^r_{\nu_i} = 1/\lambda^r_{\nu_i} + j^r_{\nu_i}$. Although $1/D_{4,\nu_i}$ is not the sum of $1/D^r_{4,\nu_i}$, I use it instead of D_{4,ν_i}, since it corresponds to the inverse mean free path.

Figures 3.17 and 3.18 show the values of $1/D^r_{4,\nu_i}$ for different reactions again at the neutrino sphere (figure 3.17) and at the radius (figure 3.18), where the temperature is highest and hence muons are expected to be most abundant, as a function of time. We can see from figure 3.17 that at the neutrino surface, the neutrino scattering on neutron is dominant for $\bar{\nu}_e$, ν_μ, ν_τ and $\bar{\nu}_\tau$. For ν_e, the capture on neutron is almost comparable. For $\bar{\nu}_\mu$, on the other hand, the flavor exchange reaction exceeds the neutron scattering at all times, which suggests that the $\bar{\nu}_\mu$ flux may be most affected by the muon existence. The flavor exchange reaction and the muon decay are smaller but not negligible also for ν_e, $\bar{\nu}_e$ and ν_μ. In the deeper region, on the other hand, the flavor exchange reaction as well as the muon decay is suppressed. I find for ν_μ that the CC reaction dominates all other reactions around $t = 20\,$s due to the reduction of effective mass, which makes a wider region available in the phase space just as for the enhancement of the neutrino scattering rate discussed in subsection 3.2.2 (see Eq. (3.80)). In the later phase, this CC reaction is suppressed due to the strong Fermi blocking of muon in the cooled PNS.

The reason for the sudden rises of $1/D_{4,\bar{\nu}_e}$ and $1/D_{4,\bar{\nu}_\mu}$ at $t \gtrsim 30\,$s in Figures 3.18(b) and 3.18(d) is that the chemical potential $\mu_{\bar{\nu}_{e,\mu}} = -\mu_{\nu_{e,\mu}} = \mu_n - \mu_p - \mu_{e,\mu}$ takes large negative values. Since the factor $f_{\bar{\nu}_{e,\mu}}(1 - f_{\bar{\nu}_{e,\mu}})$ in Eq. (3.85) is peaked at $\varepsilon = \mu_{\bar{\nu}_{e,\mu}}$ and declines rapidly at $\varepsilon > \mu_{\bar{\nu}_{e,\mu}}$, $D_{4,\bar{\nu}_e}$ and $D_{4,\bar{\nu}_\mu}$ become also smaller, which means that

matter may be transparent in this region. If so, the diffusion approximation is no longer valid and the diffusion coefficients are not a good measure for the cooling timescale.

In Figure 3.19, I show $D^{\mathrm{w/o}\ \mu}_{4,\nu_i}/D^{\mathrm{tot}}_{4,\nu_i}$, the ratios of the diffusion coefficients not including the contributions from the muon-related reactions to that including the contributions from all reactions, to see to what extent the muon-related reactions affect the energy flux at the neutrino sphere. In so doing I change the muon fraction rather arbitrarily. We can see from the figure that the ratios are enhanced for neutrinos and anti-neutrinos other than the τ-type of them as the muon fraction gets larger, i.e. the diffusion of these neutrinos is suppressed. To these changes the following reactions $\nu_e + \mu^- \to \nu_\mu + e^-$ and $\bar{\nu}_\mu + \mu^- \to \bar{\nu}_e + e^-$ give the greatest contributions for ν_e and $\bar{\nu}_\mu$, respectively, whereas the inverse muon decay $\bar{\nu}_e + \nu_\mu + e^- \to \mu^-$ is the most important for $\bar{\nu}_e$ and ν_μ. These results imply that muons behave as a reservoir of these neutrinos, disturbing their diffusions in the PNS. This in turn leads tho the prolongation of the cooling timescale of PNS.

3.3 Summary

In this chapter, I have numerically evaluated the rates of muon- and nucleon-related weak interactions of all species of neutrinos that are relevant in the cooling phase of PNS. For the semi-leptonic interactions, I have taken fully into account the relativistic kinematics of nucleon as well as the weak magnetism, the pseudoscalar term, and the q^2 dependence of form factors for nucleon; I have also considered the corrections to the dispersion relations of nucleons from nuclear interactions on the mean field level.

I have compared the inverse mean free paths of these reactions at different times. At the neutrino sphere, the inverse muon decay $\bar{\nu}_e + e^- + \nu_\mu \to \mu^-$ is the dominant source of opacity for $\bar{\nu}_e$ and ν_μ at low incoming neutrino energies whereas the flavor exchanging reactions: $\nu_e + \mu^- \to \nu_\mu + e^-$ and $\bar{\nu}_\mu + \mu^- \to \bar{\nu}_e + e^-$ give the greatest contributions for ν_e and $\bar{\nu}_\mu$ also at low neutrino energies. At high energies, on the other hand, the neutrino capture on neutron is dominant for ν_e and ν_μ whereas the scattering on neutron dominates the opacity for $\bar{\nu}_e$ and $\bar{\nu}_\mu$. In the deeper region, the muon-related reactions are suppressed compared with the semi-leptonic reactions although general features are similar to what I have found at the neutrino sphere.

In the exploration of the semi-leptonic reactions, we have observed that the weak-magnetism enhances (suppresses) the opacities for neutrino (anti-neutrino) both in the CC and NC current reactions; the q^2 dependence of form factors tends to reduce the opacities both via the CC and NC currents. I have confirmed that the pseudoscalar term gives only miner corrections even in the muon-related CC semi-leptonic reactions.

The difference of the effective potentials between neutron and proton, which I incorporate on the mean field level, shifts the threshold of the CC semi-leptonic reactions and, as a results, enhances the neutrino capture on neutron as well as the inverse neutron decay, which is one of the dominant sources of opacity in the deeper region. The neutrino scattering on neutron is enhanced, on the other hand, because the effective mass of nucleons becomes smaller in the dense region.

I have investigated the diffusion coefficients for neutrinos, which are relevant for neutrino transport in the optically thick regime. I have paid particular attention to the changes that the existence of muon will make. I have found that muons play a role of reservoir for the e- and μ-type neutrinos by disturbing their diffusion in the PNS interior. I hence expect that the cooling timescale will be longer in the presence of muons.

Our eventual goal is to employ the reaction rates obtained here in calculations of the PNS cooling, possibly in multi-spatial dimensions, and explore quantitatively their influ-

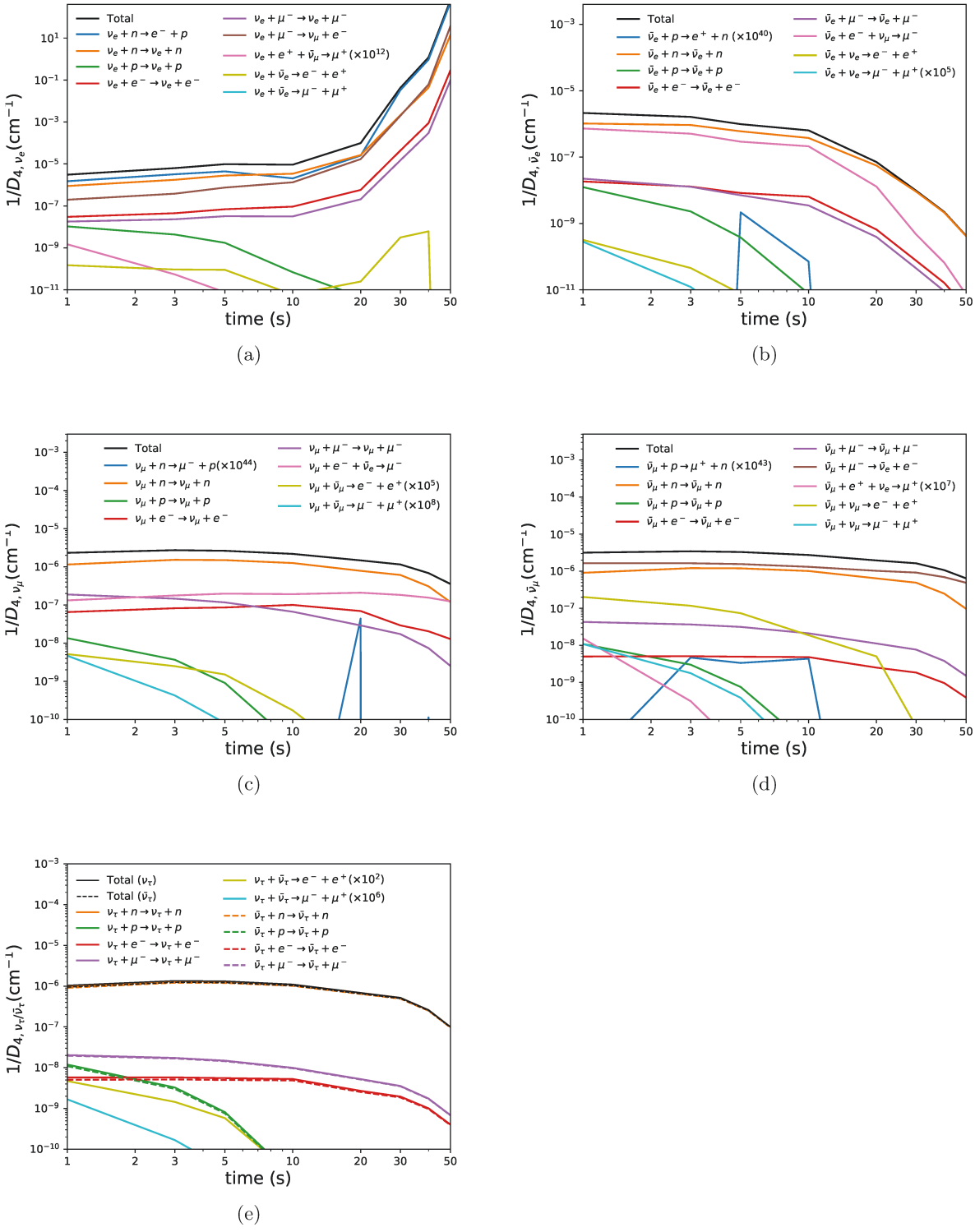

Figure 3.17: Inverse of the diffusion coefficients D_4's at the neutrino sphere for different reactions. Panels (a), (b), (c) and (d) are the results for ν_e, $\bar{\nu}_e$, ν_μ and $\bar{\nu}_\mu$, respectively. Panel (e) shows those for both ν_τ (solid line) and $\bar{\nu}_\tau$ (dashed line), respectively. Colors denote different reactions (see the legends in each panel).

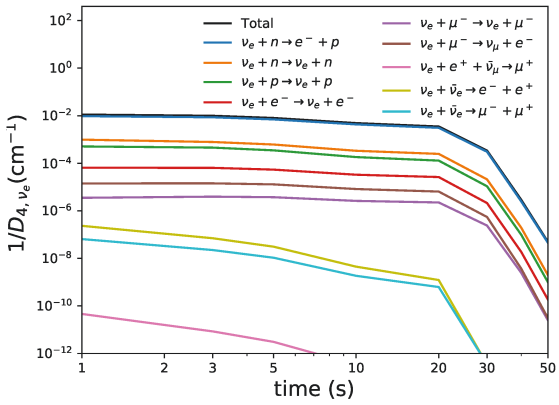

(a)

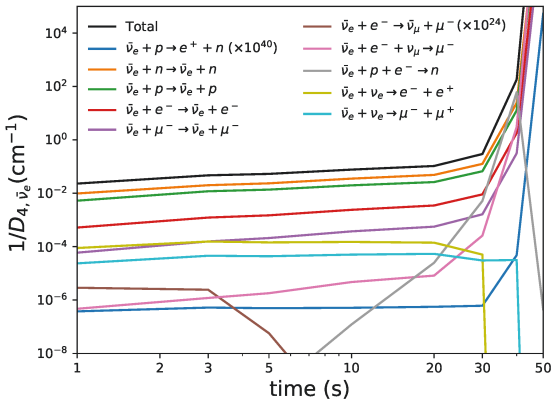

(b)

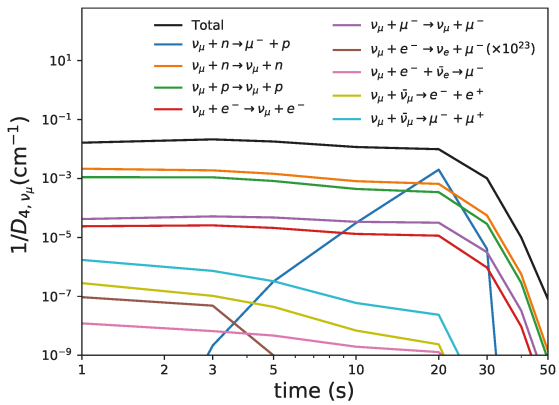

(c)

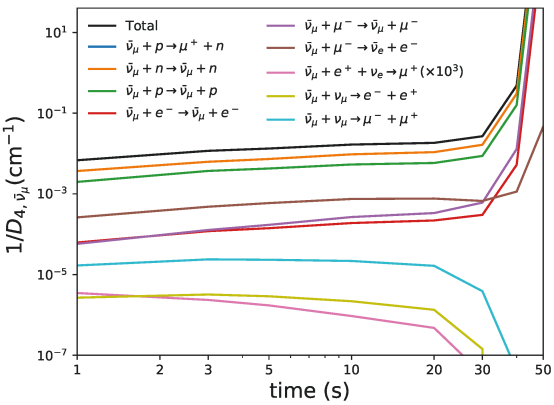

(d)

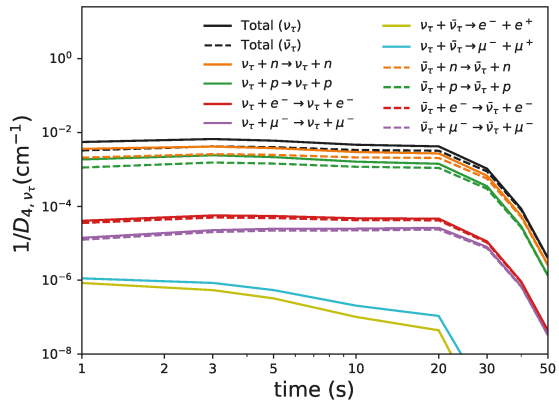

(e)

Figure 3.18: Same as Figure 3.17 but for the deeper region.

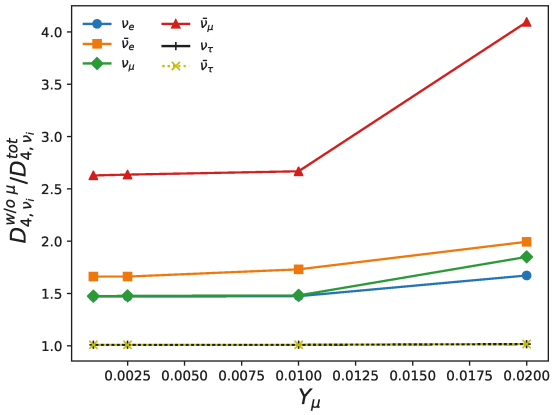

Figure 3.19: The ratio of the diffusion coefficient without the contribution from the muon-related reactions to the one with their contributions. Different colors indicate the neutrino flavors.

ences on the thermal history and neutrino emissions of PNS. It will be also interesting to apply them to CCSN simulations. The reaction rates obtained in this paper are admittedly imperfect and there is an ample room for improvement. For example, it is well known that the corrections to the dispersion relations of nucleons should be accompanied by the corrections to the vertex. On the mean field level this corresponds to the random phase approximation (RPA) to the structure functions. Note that the relativistic mean field theory, which I adopt for EoS is particularly convenient for the RPA calculations Yamada and Toki (1999). Pions are another interesting particles that may be populated in PNS and have an impact on the the opacity of ν_μ Fore and Reddy (2020). Implementing these effects in the calculations of PNS cooling is certainly the future task.

Chapter 4

Conclusion

Numerical simulations of CCSN has been conducted energetically to unveil the physical mechanism and the observable signatures of the CCSNe for decades. Due to the remarkable improvement of numerical computation technology, such as supercomputer, we can now compute multi-dimensional hydrodynamical evolution including detailed neutrino transfer. In fact, many interesting key physics such as LESA, the muon existence and so on have been found. The observation technology of neutrino also developed recently, and if the Galactic supernova occur, it is estimated that neutrino can be detected $\sim 100\,\mathrm{s}$ after the core bounce, which include the later phase of PNS cooling. However, since the Galactic supernova is so rare, the more accurate prediction and its interpretation have to be prepared in advance to extract the most information we can get from one CCSN event. In that point of view, we have to improve several things. One thing is the qualitative or intuitive understanding of the CCSN numerical simulation. Especially, multi-dimensional effects I mentioned in this thesis interact with each other complicatedly to hinder the clear understanding of the detailed physics. Another thing is taking into more precise physics (especially neutrino physics and nuclear physics) with the solid understanding. I tackled to the former problem by using the linear analysis of the shock dynamics by decomposing the multi-dimensional effects. Related with the latter problem, I reveal the fundamental neutrino interaction related with muon which understandings is indispensable to interpret the CCSN numerical simulation.

In chapter 2, the instability of the standing shock wave and the accretion flows downstream in the core of CCSNe have been investigated by linear analysis. I have focused particularly on the influences of the fluctuations at the inner boundary. The influence of the injection of acoustic power from the PNS also have been explored . Unlike the perturbation at the outer boundary, those at the inner boundary change the growth rates and oscillation frequencies of eigenmodes directly. I have hence calculated them together with the excitation amplitudes for various neutrino luminosities. I have found that the acoustic power injection enhances the growth rates of the fluid instabilities in general and the critical luminosity is reduced and the enhancement is especially remarkable at low neutrino luminosities. This is because the mismatch between the g-mode oscillations of the PNS and the oscillations in the accretion flow is reduced. The perturbation from the inner boundary excites some modes and the excitation amplitudes are also enhanced by the injection of acoustic powers. On the other hand, the perturbations of the neutrino luminosities have a slight effect on the growth rates and oscillation frequencies of eigenmodes as well as on their excitation amplitudes at least at the linear level. I have then investigated steady perturbed solutions, being motivated by the LESA phenomenon (Tamborra et al. (2014a)). I have found the steady perturbed solutions in which the neutrino lumi-

nosities is fluctuated, which we assumed are induced by the fluctuation in temperature and/or Y_e, and studied if self-sustained configurations are obtained or not. It should be stressed that it is not a trivial thing. The obtained structures are consistent with that proposed by Tamborra et al. (2014a) and such self-sustained steady states are obtained without asymmetry between ν_e and $\bar{\nu}_e$, It seems that it is the temperature fluctuation and the resultant perturbation to the sum of the fluxes of ν_e and $\bar{\nu}_e$, $F_{\nu_e} + F_{\bar{\nu}_e}$, rather than their difference that is the key to the production of these steady states. This seems consistent with the claim by Dolence et al. (2015). On the other hand, the asymmetries in the lepton emissions and in the Y_e distribution as Tamborra et al. (2014a) found them are also self-sustained although they may be a by-product.

In chapter 3, I have numerically evaluated the rates of muon- and nucleon-related weak interactions of all species of neutrinos that are relevant in the cooling phase of PNS. In the calculation of reaction rate of the semi-leptonic interactions, the relativistic kinematics of nucleon as well as the weak magnetism, the pseudoscalar term, and the q^2 dependence of form factors for nucleon have been fully taken into account I have also considered the corrections to the dispersion relations of nucleons from nuclear interactions on the mean field level. Then I focus on the inverse mean free paths of these reactions in the typical condition realized at different times of PNS cooling. I have found that muon-related reaction can be the the dominant source of opacity. At the neutrino sphere, the inverse muon decay $\bar{\nu}_e + e^- + \nu_\mu \rightarrow \mu^-$ give the greatest contributions for for $\bar{\nu}_e$ and ν_μ at low incoming neutrino energies whereas the flavor exchanging reactions: $\nu_e + \mu^- \rightarrow \nu_\mu + e^-$ and $\bar{\nu}_\mu + \mu^- \rightarrow \bar{\nu}_e + e^-$ are the dominant source of opacities for ν_e and $\bar{\nu}_\mu$ also at low neutrino energies. At high energies, on the other hand, the neutrino capture on neutron is dominant for ν_e and ν_μ whereas the scattering on neutron dominates the opacity for $\bar{\nu}_e$ and $\bar{\nu}_\mu$. In the deeper region, the muon-related reactions are suppressed compared with the semi-leptonic reactions although general features are similar to what we have found at the neutrino sphere. I have also explored the corrections to the semi-leptonic reactions and evaluated how much each correction modified the inverse mean free path. Especially I have found in the mean-field approximation, the neutrino capture on neutron is enhanced as well as the inverse neutron decay, which is one of the dominant sources of opacity in the deeper region. I have also found that the neutrino scattering on neutron is enhanced due to the suppression of the the effective mass of nucleons in the dense region. I have also investigated the diffusion coefficients for neutrinos and muons may be play a role of reservoir for the e- and μ-type neutrinos by disturbing their diffusion in the PNS interior in the later phase of the PNS cooling. I hence expect that the cooling timescale will be longer in the presence of muons.

Appendix A

Details of the derivation of leptonic reaction rates

In this appendix, I present the detailed calculations of reaction kernels for the leptonic reactions listed in Table 3.1.

A.1 Scatterings: $\nu + l \leftrightarrows \nu + l$

The spin-averaged matrix elements squared for this type of reactions are given in Eq. (3.2) with the coefficients β_i being listed in Table 3.2. The corresponding reaction kernel is written as

$$\begin{aligned} & R^{\mathrm{in}}\left(E_1, E_2, \cos\theta\right) \\ & = \iint \frac{d^3\boldsymbol{p}_1}{(2\pi)^3}\frac{d^3\boldsymbol{p}_2}{(2\pi)^3}\frac{\langle|\mathcal{M}|^2\rangle}{16E_1E_2p_1^0p_2^0}\,2f_l\left(p_1^0\right)\left[1-f_l\left(p_2^0\right)\right](2\pi)^4\,\delta^{(4)}\left(q_1^\alpha+p_1^\alpha-q_2^\alpha-p_2^\alpha\right) \quad \text{(A.1)} \\ & = \frac{G_F^2}{(2\pi)^2E_1E_2}\left[\beta_1 I_1\left(E_1,E_2,\cos\theta\right)+\beta_2 I_2\left(E_1,E_2,\cos\theta\right)+\beta_3 I_3\left(E_1,E_2,\cos\theta\right)\right], \quad \text{(A.2)} \end{aligned}$$

where the three functions I_1 through I_3 are given as

$$I_1\left(E_1,E_2,\cos\theta\right)=\iint d^3\boldsymbol{p}_1 d^3\boldsymbol{p}_2\frac{1}{p_1^0p_2^0}\delta^{(4)}\left(q_1^\alpha+p_1^\alpha-q_2^\alpha-p_2^\alpha\right)f_l\left(p_1^0\right)\left[1-f_l\left(p_2^0\right)\right](q_1\cdot p_1)\,(q_2\cdot p_2)\,, \quad \text{(A.3)}$$

$$I_2\left(E_1,E_2,\cos\theta\right)=\iint d^3\boldsymbol{p}_1 d^3\boldsymbol{p}_2\frac{1}{p_1^0p_2^0}\delta^{(4)}\left(q_1^\alpha+p_1^\alpha-q_2^\alpha-p_2^\alpha\right)f_l\left(p_1^0\right)\left[1-f_l\left(p_2^0\right)\right](q_1\cdot p_2)\,(q_2\cdot p_1)\,, \quad \text{(A.4)}$$

$$I_3\left(E_1,E_2,\cos\theta\right)=\iint d^3\boldsymbol{p}_1 d^3\boldsymbol{p}_2\frac{1}{p_1^0p_2^0}\delta^{(4)}\left(q_1^\alpha+p_1^\alpha-q_2^\alpha-p_2^\alpha\right)f_l\left(p_1^0\right)\left[1-f_l\left(p_2^0\right)\right]m_l^2\,(q_1\cdot q_2)\,. \quad \text{(A.5)}$$

The integrations in I_1, I_2 and I_3 can be analytically done following the previous works Yueh and Buchler (1977); Mezzacappa and Bruenn (1993):

$$I_1\left(E_1, E_2, \cos\theta\right) = \frac{2\pi E_1^2 E_2^2}{\Delta^5}\left(1-\cos\theta\right)^2 \int_{\epsilon_{\min}}^{\infty} d\epsilon_l f_l\left(\epsilon_l\right)\left[1-f_l\left(\epsilon_l + E_1 - E_2\right)\right]\left(A_1\epsilon_l^2 + B_1\epsilon_l + C_1\right), \tag{A.6}$$

$$A_1 = E_1^2 + E_2^2 + E_1E_2\left(3+\cos\theta\right), \tag{A.7}$$

$$B_1 = E_1\left[2E_1^2 + E_1E_2\left(3-\cos\theta\right) - E_2^2\left(1+3\cos\theta\right)\right], \tag{A.8}$$

$$C_1 = E_1^2\left[E_1^2 - 2E_1E_2\cos\theta + \frac{1}{2}E_2^2\left(3\cos^2\theta - 1\right) - \frac{m_l^2}{2}\frac{1+\cos\theta}{1-\cos\theta}\frac{\Delta^2}{E_1^2}\right], \tag{A.9}$$

$$\Delta = \sqrt{E_1^2 + E_2^2 - 2E_1E_2\cos\theta}, \tag{A.10}$$

$$\epsilon_{\min} = \max\left\{m_l, \epsilon_-, -\left(E_1 - E_2\right)\right\}, \tag{A.11}$$

$$\epsilon_- = -\frac{E_1 - E_2}{2} + \frac{\Delta}{2}\sqrt{1 + \frac{2m_l^2}{E_1E_2(1-\cos\theta)}}; \tag{A.12}$$

the remaining integral over ϵ_l can be reduced to the Fermi-Dirac integrals:

$$\begin{aligned} J_0 &= \int_{\epsilon_{\min}}^{\infty} d\epsilon_l f_l\left(\epsilon_l\right)\left[1-f_l\left(\epsilon_l + E_1 - E_2\right)\right] \\ &= \frac{1}{e^{-\beta(E_1-E_2)}-1}\int_{\epsilon_{\min}}^{\infty} d\epsilon_l\left[f_l\left(\epsilon_l + E_1 - E_2\right) - f_l\left(\epsilon_l\right)\right] \\ &= \frac{1}{\beta}\frac{1}{e^{-\beta(E_1-E_2)}-1}\int_0^{\infty} dz\left\{\frac{1}{1+\exp\left[z - \beta\left(\mu_l - \left(E_1-E_2\right) - \epsilon_{\min}\right)\right]} - \frac{1}{1+\exp\left[z-\beta\left(\mu_l - \epsilon_{\min}\right)\right]}\right\} \\ &= \frac{T}{e^{(E_2-E_1)/T}-1}G_0\left(\beta\epsilon_{\min}\right), \end{aligned} \tag{A.13}$$

$$\begin{aligned} J_1 &= \int_{\epsilon_{\min}}^{\infty} d\epsilon_l f_l\left(\epsilon_l\right)\left[1-f_l\left(\epsilon_l + E_1 - E_2\right)\right]\epsilon_l \\ &= \frac{T^2}{e^{(E_2-E_1)/T}-1}\left[G_1\left(\beta\epsilon_{\min}\right) + \beta\epsilon_{\min}G_0\left(\beta\epsilon_{\min}\right)\right], \end{aligned} \tag{A.14}$$

$$\begin{aligned} J_2 &= \int_{\epsilon_{\min}}^{\infty} d\epsilon_l f_l\left(\epsilon_l\right)\left[1-f_l\left(\epsilon_l + E_1 - E_2\right)\right]\epsilon_l^2 \\ &= \frac{T^3}{e^{(E_2-E_1)/T}-1}\left[G_2\left(\beta\epsilon_{\min}\right) + 2\beta\epsilon_{\min}G_1\left(\beta\epsilon_{\min}\right) + \left(\beta\epsilon_{\min}\right)^2 G_0\left(\beta\epsilon_{\min}\right)\right], \end{aligned} \tag{A.15}$$

where $\beta = 1/T$ and μ_l is the chemical potential of lepton l and G_i is defined as

$$G_i(\beta\epsilon) = F_i\left[\beta\left(\mu_l - \left(E_1 - E_2\right) - \epsilon\right)\right] - F_i\left[\beta\left(\mu_l - \epsilon\right)\right] \tag{A.16}$$

with $F_i[\eta]$ being the Fermi-Dirac integrals defined as

$$F_i[\eta] = \int_0^{\infty}\frac{x^i}{e^{x-\eta}+1}dx \quad (\text{for } i \geq 0). \tag{A.17}$$

Note that J_0 through J_2 are not divergent at $E_1 = E_2$ and are given as

$$J_0 = TF_{-1}\left[\beta\left(\mu_l - \epsilon_{\min}\right)\right], \tag{A.18}$$

$$J_1 = T^2\left\{F_0\left[\beta\left(\mu_l - \epsilon_{\min}\right)\right] + \beta\epsilon_{\min}F_{-1}\left[\beta\left(\mu_l - \epsilon_{\min}\right)\right]\right\}, \tag{A.19}$$

$$J_2 = T^3\left\{2F_1\left[\beta\left(\mu_l - \epsilon_{\min}\right)\right] + 2\beta\epsilon_{\min}F_0\left[\beta\left(\mu_l - \epsilon_{\min}\right)\right] + \left(\beta\epsilon_{\min}\right)^2 F_{-1}\left[\beta\left(\mu_l - \epsilon_{\min}\right)\right]\right\}, \tag{A.20}$$

with

$$F_{-1}[\eta] = \frac{1}{e^{-\eta}+1}. \tag{A.21}$$

To summarize, we get

$$I_1\left(E_1, E_2, \cos\theta\right) = \frac{2\pi E_1^2 E_2^2}{\Delta^5}\left(1-\cos\theta\right)^2\left(A_1 J_2 + B_1 J_1 + C_1 J_0\right). \tag{A.22}$$

The other two integrals I_2 and I_3 are calculated in a similar way as

$$\begin{aligned}
&I_2\left(E_1, E_2, \cos\theta\right) \\
&= \int d^3\boldsymbol{p}_1 d^3\boldsymbol{p}_2 \frac{1}{p_1^0 p_2^0}\,\delta^{(4)}\left((-q_2^\alpha) + p_1^\alpha - (-q_1^\alpha) - p_2^\alpha\right) f_l\left(p_1^0\right)\left[1 - f_l\left(p_2^0\right)\right]\left((-q_1)\cdot p_2\right)\left((-q_2)\cdot p_1\right) \\
&= I_1\left(-E_2, -E_1, \cos\theta\right), \qquad (A.23) \\
&I_3\left(E_1, E_2, \cos\theta\right) \\
&= \frac{2\pi m_l^2 E_1 E_2}{\Delta}\left(1-\cos\theta\right)\int_{\epsilon_{\min}}^{\infty} d\epsilon_l f_l\left(\epsilon_l\right)\left[1 - f_l\left(\epsilon_l + E_1 - E_2\right)\right] \\
&= \frac{2\pi m_l^2 E_1 E_2}{\Delta}\left(1-\cos\theta\right) J_0. \qquad (A.24)
\end{aligned}$$

The other kernel R^{out} is obtained from the detailed balance, Eq. (3.10).

A.2 Lepton flavor exchange/conversion reactions

The spin-averaged matrix element squared for these reactions are given in Eq. (3.16) and the coefficients α_i are listed in Table 3.3. I present here the detailed expression of R_ν^{out} in Eq. (3.20), which is similar to that of the lepton scattering counterpart:

$$\begin{aligned}
&R_\nu^{\text{out}}\left(E_1, E_2, \cos\theta\right) \\
&= \iint \frac{d^3\boldsymbol{p_1}}{(2\pi)^3}\frac{d^3\boldsymbol{p_2}}{(2\pi)^3}\frac{\langle|\mathcal{M}|^2\rangle}{16 E_1 E_2 p_1^0 p_2^0}\,2 f_e\left(p_e^0\right)\left[1 - f_\mu\left(p_\mu^0\right)\right](2\pi)^4\,\delta^{(4)}\left(q_1^\alpha + p_\mu^\alpha - q_2^\alpha - p_e^\alpha\right) \qquad (A.25) \\
&= \frac{8G_F^2}{(2\pi)^2 E_1 E_2}\left[\alpha_1 I_1\left(E_1, E_2, \cos\theta\right) + \alpha_2 I_2\left(E_1, E_2, \cos\theta\right)\right], \qquad (A.26)
\end{aligned}$$

where I_1 is expressed as

$$I_1\left(E_1,E_2,\cos\theta\right)=\iint d^3\boldsymbol{p}_\mu d^3\boldsymbol{p}_e\frac{1}{p_\mu^0 p_e^0}\,\delta^{(4)}\left(q_1^\alpha+p_\mu^\alpha-q_2^\alpha-p_e^\alpha\right)f_e\left(p_e^0\right)\left[1-f_\mu\left(p_\mu^0\right)\right](q_1\cdot p_e)\,(q_2\cdot p_\mu)\,, \tag{A.27}$$

$$=\frac{2\pi E_1E_2}{\Delta^5}\left(A_1J_2+B_1J_1+C_1J_0\right), \tag{A.28}$$

$$A_1=E_1E_2\left(1-\cos\theta\right)^2\left[E_1^2+E_2^2+E_1E_2\left(3+\cos\theta\right)\right], \tag{A.29}$$

$$\begin{aligned}B_1=&E_1E_2^2\left(1-\cos\theta\right)^2\left[E_1^2\left(1+3\cos\theta\right)-E_1E_2\left(3-\cos\theta\right)-2E_2^2\right]\\&+Q\left(E_2-E_1\right)\left(1-\cos\theta\right)\left[E_1^2+E_1E_2\left(3+\cos\theta\right)+E_2^2\right],\end{aligned} \tag{A.30}$$

$$\begin{aligned}C_1=&E_1E_2^3\left(1-\cos\theta\right)^2\left[\frac{1}{2}E_1^2\left(3\cos^2\theta-1\right)-2E_1E_2\cos\theta+E_2^2\right]-\frac{m_\mu^2}{2}E_1E_2\left(1-\cos^2\theta\right)\Delta^2\\&-QE_2\left(1-\cos\theta\right)\left[E_1^3\cos\theta-E_1^2E_2\left(2-\cos^2\theta\right)-E_1E_2^2\cos\theta+E_2^3\right]\\&+Q^2\left[E_1^2\cos\theta-\frac{1}{2}E_1E_2\left(3+\cos^2\theta\right)+E_2^2\cos\theta\right],\end{aligned} \tag{A.31}$$

$$\Delta=\sqrt{E_1^2+E_2^2-2E_1E_2\cos\theta}, \tag{A.32}$$

$$Q=\frac{1}{2}\left(m_\mu^2-m_e^2\right). \tag{A.33}$$

In the above expression, J_i's are again written with the Fermi-Dirac integrals:

$$J_0=\frac{T}{1-e^{[\mu_\mu-(\mu_e+E_2-E_1)]/T}}G_0\left(\beta\epsilon_{\min}\right), \tag{A.34}$$

$$J_1=\frac{T^2}{1-e^{[\mu_\mu-(\mu_e+E_2-E_1)]/T}}\left[G_1\left(\beta\epsilon_{\min}\right)+\beta\epsilon_{\min}G_0\left(\beta\epsilon_{\min}\right)\right], \tag{A.35}$$

$$J_2=\frac{T^3}{1-e^{[\mu_\mu-(\mu_e+E_2-E_1)]/T}}\left[G_2\left(\beta\epsilon_{\min}\right)+2\beta\epsilon_{\min}G_1\left(\beta\epsilon_{\min}\right)+\left(\beta\epsilon_{\min}\right)^2G_0\left(\beta\epsilon_{\min}\right)\right], \tag{A.36}$$

$$\Delta=\sqrt{E_1^2+E_2^2-2E_1E_2\cos\theta}, \tag{A.37}$$

$$\epsilon_{\min}=\max\left\{m_\mu,\epsilon_+,m_e+E_2-E_1\right\}, \tag{A.38}$$

$$\epsilon_+=\frac{E_2-E_1}{2}\left(1-\kappa\right)+\frac{\Delta}{2}\sqrt{\left(1-\kappa\right)^2+\frac{2m_\mu^2}{E_1E_2(1-\cos\theta)}}, \tag{A.39}$$

$$\kappa=\frac{Q}{E_1E_2\left(1-\cos\theta\right)}, \tag{A.40}$$

where μ_μ and μ_e are the chemical potentials of muon and electron, respectively, and G_i's are given as

$$G_i\left(\beta\epsilon\right)=F_i\left[\beta\left(\mu_e-\left(E_1-E_2\right)-\epsilon\right)\right]-F_i\left[\beta\left(\mu_\mu-\epsilon\right)\right]. \tag{A.41}$$

There is no divergence at $\mu_\mu=\mu_e+E_2-E_1$, and J_0 through J_2 are obtained as

$$J_0=TF_{-1}\left[\beta\left(\mu_\mu-\epsilon_{\min}\right)\right], \tag{A.42}$$

$$J_1=T^2\left\{F_0\left[\beta\left(\mu_\mu-\epsilon_{\min}\right)\right]+\beta\epsilon_{\min}F_{-1}\left[\beta\left(\mu_\mu-\epsilon_{\min}\right)\right]\right\}, \tag{A.43}$$

$$J_2=T^3\left\{2F_1\left[\beta\left(\mu_\mu-\epsilon_{\min}\right)\right]+2\beta\epsilon_{\min}F_0\left[\beta\left(\mu_\mu-\epsilon_{\min}\right)\right]+\left(\beta\epsilon_{\min}\right)^2F_{-1}\left[\beta\left(\mu_\mu-\epsilon_{\min}\right)\right]\right\}. \tag{A.44}$$

The remaining I_2 can be obtained from the following relation:

$$I_2\left(E_1, E_2, \cos\theta\right) = I_1\left(-E_2, -E_1, \cos\theta\right). \tag{A.45}$$

The other kernel $R_\nu^{\rm in}$ is obtained from the detailed balance, Eq. (3.19).

A.3 Muon decays

The calculation of $R_{\bar{\nu}_e}^{\rm out}$ in Eq. (3.29) proceeds in a similar way to those for the above two reactions:

$$\begin{aligned} &R_{\bar{\nu}_e}^{\rm out}\left(E_{\bar{\nu}_e}, E_{\nu_\mu}, \cos\theta\right) \\ &= \iint \frac{d^3\boldsymbol{p}_\mu}{(2\pi)^3}\frac{d^3\boldsymbol{p}_e}{(2\pi)^3}\frac{\langle|\mathcal{M}|^2\rangle}{16E_{\bar{\nu}_e}E_{\nu_\mu}p_\mu^0 p_e^0}\,2f_\mu\left(p_\mu^0\right)\left[1-f_e\left(p_e^0\right)\right](2\pi)^4\,\delta^{(4)}\left(p_\mu^\alpha - p_e^\alpha - q_{\bar{\nu}_e}^\alpha - q_{\nu_\mu}^\alpha\right) \end{aligned} \tag{A.46}$$

$$= \frac{8G_F^2}{(2\pi)^2 E_{\bar{\nu}_e}E_{\nu_\mu}} I_1\left(E_{\bar{\nu}_e}, E_{\nu_\mu}, \cos\theta\right), \tag{A.47}$$

in which the spin-averaged matrix element squared is given in Eq. (3.25) and I_1 is written as

$$\begin{aligned} &I_1\left(E_{\bar{\nu}_e}, E_{\nu_\mu}, \cos\theta\right) \\ &= \iint d^3\boldsymbol{p}_\mu d^3\boldsymbol{p}_e \frac{1}{p_\mu^0 p_e^0}\delta^{(4)}\left(p_\mu^\alpha - p_e^\alpha - q_{\bar{\nu}_e}^\alpha - q_{\nu_\mu}^\alpha\right) 2f_\mu\left(p_\mu^0\right)\left[1-f_e\left(p_e^0\right)\right]\left(q_{\bar{\nu}_e}\cdot p_e\right)\left(q_{\nu_\mu}\cdot p_\mu\right), \end{aligned} \tag{A.48}$$

$$= \frac{2\pi E_{\bar{\nu}_e}E_{\nu_\mu}}{\Delta^5}\Theta(D)\left(A_1 J_2 + B_1 J_1 + C_1 J_0\right), \tag{A.49}$$

with Θ being the Heaviside function and

$$A_1 = -E_{\bar{\nu}_e}E_{\nu_\mu}\left(1-\cos\theta\right)^2\left[E_{\bar{\nu}_e}^2 + E_{\nu_\mu}^2 - E_{\bar{\nu}_e}E_{\nu_\mu}\left(3+\cos\theta\right)\right], \tag{A.50}$$

$$\begin{aligned} B_1 = {} & E_{\bar{\nu}_e}E_{\nu_\mu}^2\left(1-\cos\theta\right)^2\left[E_{\bar{\nu}_e}^2\left(1+3\cos\theta\right) + E_{\bar{\nu}_e}E_{\nu_\mu}\left(3-\cos\theta\right) - 2E_{\nu_\mu}^2\right] \\ & + Q\left(E_{\nu_\mu} + E_{\bar{\nu}_e}\right)\left(1-\cos\theta\right)\left[E_{\bar{\nu}_e}^2 - E_{\bar{\nu}_e}E_{\nu_\mu}\left(3+\cos\theta\right) + E_{\nu_\mu}^2\right], \end{aligned} \tag{A.51}$$

$$\begin{aligned} C_1 = {} & -E_{\bar{\nu}_e}E_{\nu_\mu}^3\left(1-\cos\theta\right)^2\left[\frac{1}{2}E_{\bar{\nu}_e}^2\left(3\cos^2\theta - 1\right) + 2E_{\bar{\nu}_e}E_{\nu_\mu}\cos\theta + E_{\nu_\mu}^2\right] + \frac{m_e^2}{2}E_{\bar{\nu}_e}E_{\nu_\mu}\left(1-\cos^2\theta\right)\Delta^2 \\ & - QE_{\nu_\mu}\left(1-\cos\theta\right)\left[E_{\bar{\nu}_e}^3\cos\theta + E_{\bar{\nu}_e}^2E_{\nu_\mu}\left(2-\cos^2\theta\right) - E_{\bar{\nu}_e}E_{\nu_\mu}^2\cos\theta - E_{\nu_\mu}^3\right] \\ & + Q^2\left[E_{\bar{\nu}_e}^2\cos\theta + \frac{1}{2}E_{\bar{\nu}_e}E_{\nu_\mu}\left(3+\cos^2\theta\right) + E_{\nu_\mu}^2\cos\theta\right], \end{aligned} \tag{A.52}$$

$$\Delta = \sqrt{E_{\bar{\nu}_e}^2 + E_{\nu_\mu}^2 + 2E_{\bar{\nu}_e}E_{\nu_\mu}\cos\theta}, \tag{A.53}$$

$$Q = \frac{1}{2}\left(m_\mu^2 - m_e^2\right), \tag{A.54}$$

$$D = \left(1-\kappa\right)^2 - \frac{2m_e^2}{E_{\bar{\nu}_e}E_{\nu_\mu}\left(1-\cos\theta\right)}, \tag{A.55}$$

$$\kappa = \frac{Q}{E_{\bar{\nu}_e}E_{\nu_\mu}\left(1-\cos\theta\right)}; \tag{A.56}$$

J_i's are given by the Fermi-Dirac integrals:

$$J_0 = \frac{T}{1-e^{\left(E_{\bar{\nu}_e}+E_{\nu_\mu}+\mu_e-\mu_\mu\right)/T}}\left[G_0\left(\beta\epsilon_{\min}\right)-G_0\left(\beta\epsilon_{\max}\right)\right], \tag{A.57}$$

$$J_1 = \frac{T^2}{1-e^{\left(E_{\bar{\nu}_e}+E_{\nu_\mu}+\mu_e-\mu_\mu\right)/T}}\left\{\left[G_1\left(\beta\epsilon_{\min}\right)+\beta\epsilon_{\min}G_0\left(\beta\epsilon_{\min}\right)\right]-\left[G_1\left(\beta\epsilon_{\max}\right)+\beta\epsilon_{\max}G_0\left(\beta\epsilon_{\max}\right)\right]\right\}, \tag{A.58}$$

$$J_2 = \frac{T^3}{1-e^{\left(E_{\bar{\nu}_e}+E_{\nu_\mu}+\mu_e-\mu_\mu\right)/T}}\left\{\left[G_2\left(\beta\epsilon_{\min}\right)+2\beta\epsilon_{\min}G_1\left(\beta\epsilon_{\min}\right)+\left(\beta\epsilon_{\min}\right)^2G_0\left(\beta\epsilon_{\min}\right)\right]\right.$$
$$\left.-\left[G_2\left(\beta\epsilon_{\max}\right)+2\beta\epsilon_{\max}G_1\left(\beta\epsilon_{\max}\right)+\left(\beta\epsilon_{\max}\right)^2G_0\left(\beta\epsilon_{\max}\right)\right]\right\}, \tag{A.59}$$

$$\epsilon_{\min} = \max\left\{m_l, \epsilon_-, m_\mu-\left(E_{\bar{\nu}_e}+E_{\nu_\mu}\right)\right\}, \tag{A.60}$$

$$\epsilon_{\max} = \epsilon_+, \tag{A.61}$$

$$\epsilon_\pm = \frac{E_{\bar{\nu}_e}+E_{\nu_\mu}}{2}(\kappa-1)\pm\frac{\Delta}{2}\sqrt{(1-\kappa)^2-\frac{2m_e^2}{E_{\bar{\nu}_e}E_{\nu_\mu}(1-\cos\theta)}} = \frac{E_{\bar{\nu}_e}+E_{\nu_\mu}}{2}(\kappa-1)\pm\frac{\Delta}{2}\sqrt{D}, \tag{A.62}$$

where μ_μ and μ_e are the chemical potentials of muon and electron, respectively, and G_i's are given as

$$G_i\left(\beta\epsilon\right) = F_i\left[\beta\left(\mu_\mu-\left(E_{\bar{\nu}_e}+E_{\nu_\mu}\right)-\epsilon\right)\right]-F_i\left[\beta\left(\mu_e-\epsilon\right)\right] \tag{A.63}$$

We obtain J_0 through J_2 at $\mu_\mu = \mu_e + E_{\bar{\nu}_e} + E_{\nu_\mu}$ by taking appropriate limits:

$$J_0 = T\left\{F_{-1}\left[\beta\left(\mu_e-\epsilon_{\min}\right)\right]-F_{-1}\left[\beta\left(\mu_e-\epsilon_{\max}\right)\right]\right\}, \tag{A.64}$$

$$J_1 = T^2\left(\left\{F_0\left[\beta\left(\mu_e-\epsilon_{\min}\right)\right]+\beta\epsilon_{\min}F_{-1}\left[\beta\left(\mu_e-\epsilon_{\min}\right)\right]\right\}\right.$$
$$\left.-\left\{F_0\left[\beta\left(\mu_e-\epsilon_{\max}\right)\right]+\beta\epsilon_{\max}F_{-1}\left[\beta\left(\mu_e-\epsilon_{\max}\right)\right]\right\}\right), \tag{A.65}$$

$$J_2 = T^3\left(\left\{2F_1\left[\beta\left(\mu_e-\epsilon_{\min}\right)\right]+2\beta\epsilon_{\min}F_0\left[\beta\left(\mu_e-\epsilon_{\min}\right)\right]+\left(\beta\epsilon_{\min}\right)^2F_{-1}\left[\beta\left(\mu_e-\epsilon_{\min}\right)\right]\right\}\right.$$
$$\left.-\left\{2F_1\left[\beta\left(\mu_e-\epsilon_{\max}\right)\right]+2\beta\epsilon_{\max}F_0\left[\beta\left(\mu_e-\epsilon_{\max}\right)\right]+\left(\beta\epsilon_{\max}\right)^2F_{-1}\left[\beta\left(\mu_e-\epsilon_{\max}\right)\right]\right\}\right). \tag{A.66}$$

The other kernel $R^{\text{in}}_{\bar{\nu}_e}$ is obtained from the detailed balance, Eq. (3.28)

A.4 Pair creations/annihilations

The spin-averaged matrix element squared is given in (3.31) and the coefficients α and β_i are listed in Table 3.4. Here I presents the detailed expression of $R^{\text{out}}_{\nu_1}$ in Eq. (3.35), which is written as

$$R^{\text{out}}_{\nu_1}\left(E_1, E_2, \cos\theta\right)$$
$$= \iint\frac{d^3\boldsymbol{p}_1}{(2\pi)^3}\frac{d^3\boldsymbol{p}_2}{(2\pi)^3}\frac{\langle|\mathcal{M}|^2\rangle}{16E_1E_2p_1^0p_2^0}2f_{l^-}\left(p_1^0\right)2f_{l^+}\left(p_2^0\right)(2\pi)^4\delta^{(4)}\left(q_1^\alpha+q_2^\alpha-p_1^\alpha-p_2^\alpha\right) \tag{A.67}$$

$$= \frac{2G_F^2}{(2\pi)^2E_1E_2}\left[\beta_1I_1\left(E_1,E_2,\cos\theta\right)+\beta_2I_2\left(E_1,E_2,\cos\theta\right)+\beta_3I_3\left(E_1,E_2,\cos\theta\right)\right], \tag{A.68}$$

where I_1 can be cast into the following form:

$$I_1\left(E_1,E_2,\cos\theta\right)=\iint d^3\boldsymbol{p}_1 d^3\boldsymbol{p}_2\frac{1}{p_1^0p_2^0}\delta^{(4)}\left(q_1^\alpha+q_2^\alpha-p_1^\alpha-p_2^\alpha\right)f_{l^-}\left(p_1^0\right)f_{l^+}\left(p_2^0\right)\left(q_1\cdot p_1\right)\left(q_2\cdot p_2\right), \tag{A.69}$$

$$=\frac{2\pi E_1^2E_2^2}{\Delta^5}\left(1-\cos\theta\right)^2\Theta(D)\left(A_1J_2+B_1J_1+C_1J_0\right), \tag{A.70}$$

$$A_1=E_1^2+E_2^2-E_1E_2\left(3+\cos\theta\right), \tag{A.71}$$

$$B_1=E_1\left[-2E_1^2+E_1E_2\left(3-\cos\theta\right)+E_2^2\left(1+3\cos\theta\right)\right], \tag{A.72}$$

$$C_1=E_1^2\left[E_1^2+2E_1E_2\cos\theta+\frac{1}{2}E_2^2\left(3\cos^2\theta-1\right)-\frac{m_l^2}{2}\frac{1+\cos\theta}{1-\cos\theta}\frac{\Delta^2}{E_1^2}\right], \tag{A.73}$$

$$\Delta=\sqrt{E_1^2+E_2^2+2E_1E_2\cos\theta}, \tag{A.74}$$

$$D=1-\frac{2m_l^2}{E_1E_2\left(1-\cos\theta\right)}. \tag{A.75}$$

Here again J_i's are written in terms of the Fermi-Dirac integrals:

$$J_0=\frac{T}{e^{(E_1+E_2)/T}-1}\left[G_0\left(\beta\epsilon_{\min}\right)-G_0\left(\beta\epsilon_{\max}\right)\right], \tag{A.76}$$

$$J_1=\frac{T^2}{e^{(E_1+E_2)/T}-1}\left\{\left[G_1\left(\beta\epsilon_{\min}\right)+\beta\epsilon_{\min}G_0\left(\beta\epsilon_{\min}\right)\right]-\left[G_1\left(\beta\epsilon_{\max}\right)+\beta\epsilon_{\max}G_0\left(\beta\epsilon_{\max}\right)\right]\right\}, \tag{A.77}$$

$$J_2=\frac{T^3}{e^{(E_1+E_2)/T}-1}\left\{\left[G_2\left(\beta\epsilon_{\min}\right)+2\beta\epsilon_{\min}G_1\left(\beta\epsilon_{\min}\right)+\left(\beta\epsilon_{\min}\right)^2G_0\left(\beta\epsilon_{\min}\right)\right]-\left[G_2\left(\beta\epsilon_{\max}\right)+2\beta\epsilon_{\max}G_1\left(\beta\epsilon_{\max}\right)+\left(\beta\epsilon_{\max}\right)^2G_0\left(\beta\epsilon_{\max}\right)\right]\right\}, \tag{A.78}$$

$$\epsilon_{\min}=\max\left\{m_l,\epsilon_-\right\}, \tag{A.79}$$

$$\epsilon_{\max}=\min\left\{E_1+E_2-m_l,\epsilon_+\right\}, \tag{A.80}$$

$$\epsilon_\pm=\frac{E_1+E_2}{2}\pm\frac{\Delta}{2}\sqrt{1-\frac{2m_l^2}{E_1E_2(1-\cos\theta)}}=\frac{E_1+E_2}{2}\pm\frac{\Delta}{2}\sqrt{D}, \tag{A.81}$$

with

$$G_i\left(\beta\epsilon\right)=F_i\left[\beta\left(\mu_{l^-}+E_1+E_2-\epsilon\right)\right]-F_i\left[\beta\left(\mu_{l^-}-\epsilon\right)\right]; \tag{A.82}$$

I_2 and I_3 are calculated in the similar way as

$$I_2\left(E_1,E_2,\cos\theta\right)=I_1\left(E_2,E_1,\cos\theta\right), \tag{A.83}$$

$$I_3\left(E_1,E_2,\cos\theta\right)=\frac{2\pi m_l^2E_1E_2}{\Delta}\left(1-\cos\theta\right)\Theta\left(D\right)J_0. \tag{A.84}$$

The other kernel $R^{\rm in}_{\nu_1}$ is obtained from the detailed balance, Eq. (3.34).

A.5 Leptonic annihilations

The calculation of $R^{\rm out}_{\nu_e}$ in Eq. (3.43) proceeds similarly to that for the muon decay. It is expressed as

$$\begin{aligned} &R^{\rm out}_{\nu_e}\left(E_{\nu_e}, E_{\nu_\mu}, \cos\theta\right) \\ &= \iint \frac{d^3\boldsymbol{p}_\mu}{(2\pi)^3}\frac{d^3\boldsymbol{p}_e}{(2\pi)^3}\frac{\langle|\mathcal{M}|^2\rangle}{16E_{\nu_e}E_{\nu_\mu}p^0_\mu p^0_e} 2f_e\left(p^0_e\right)2f_\mu\left(p^0_\mu\right)(2\pi)^4\,\delta^{(4)}\left(p^\alpha_e + p^\alpha_\mu - q^\alpha_{\nu_e} - q^\alpha_{\nu_\mu}\right) \end{aligned} \tag{A.85}$$

$$= \frac{8G_F^2}{(2\pi)^2 E_{\nu_e}E_{\nu_\mu}} I_1\left(E_{\nu_e}, E_{\nu_\mu}, \cos\theta\right), \tag{A.86}$$

where the spin-averaged matrix element squared is given in Eq. (3.39) and I_1 can be cast into the following form:

$$\begin{aligned} &I_1\left(E_{\nu_e}, E_{\nu_\mu}, \cos\theta\right) \\ &= \iint d^3\boldsymbol{p}_\mu d^3\boldsymbol{p}_e \frac{1}{p^0_\mu p^0_e}\delta^{(4)}\left(p^\alpha_e + p^\alpha_\mu - q^\alpha_{\nu_e} - q^\alpha_{\nu_\mu}\right) 2f_e\left(p^0_e\right)2f_\mu\left(p^0_\mu\right)\left(q_{\nu_e}\cdot p_e\right)\left(q_{\nu_\mu}\cdot p_\mu\right), \end{aligned} \tag{A.87}$$

$$= \frac{2\pi E_{\nu_e}E_{\nu_\mu}}{\Delta^5}\Theta(D)\left(A_1J_2 + B_1J_1 + C_1J_0\right), \tag{A.88}$$

where Θ is again the Heaviside function and other factors are given as follows:

$$A_1 = E_{\nu_e}E_{\nu_\mu}\left(1-\cos\theta\right)^2\left[E^2_{\nu_e} + E^2_{\nu_\mu} - E_{\nu_e}E_{\nu_\mu}\left(3+\cos\theta\right)\right], \tag{A.89}$$

$$\begin{aligned} B_1 = {}& E^2_{\nu_e}E_{\nu_\mu}\left(1-\cos\theta\right)^2\left[E^2_{\nu_\mu}\left(1+3\cos\theta\right) + E_{\nu_\mu}E_{\nu_e}\left(3-\cos\theta\right) - 2E^2_{\nu_e}\right] \\ &- Q\left(E_{\nu_e}+E_{\nu_\mu}\right)\left(1-\cos\theta\right)\left[E^2_{\nu_\mu} - E_{\nu_\mu}E_{\nu_e}\left(3+\cos\theta\right) + E^2_{\nu_e}\right], \end{aligned} \tag{A.90}$$

$$\begin{aligned} C_1 = {}& -E_{\nu_\mu}E^3_{\nu_e}\left(1-\cos\theta\right)^2\left[\frac{1}{2}E^2_{\nu_\mu}\left(3\cos^2\theta - 1\right) + 2E_{\nu_\mu}E_{\nu_e}\cos\theta + E^2_{\nu_e}\right] - \frac{m^2_\mu}{2}E_{\nu_\mu}E_{\nu_e}\left(1-\cos^2\theta\right)\Delta^2 \\ &+ QE_{\nu_e}\left(1-\cos\theta\right)\left[-E^3_{\nu_\mu}\cos\theta - E^2_{\nu_\mu}E_{\nu_e}\left(2-\cos^2\theta\right) + E_{\nu_\mu}E^2_{\nu_e}\cos\theta + E^3_{\nu_e}\right] \\ &- Q^2\left[E^2_{\nu_\mu}\cos\theta + \frac{1}{2}E_{\nu_\mu}E_{\nu_e}\left(3+\cos^2\theta\right) + E^2_{\nu_e}\cos\theta\right], \end{aligned} \tag{A.91}$$

$$\Delta = \sqrt{E^2_{\nu_\mu} + E^2_{\nu_e} + 2E_{\nu_\mu}E_{\nu_e}\cos\theta}, \tag{A.92}$$

$$Q = \frac{1}{2}\left(m^2_\mu - m^2_e\right), \tag{A.93}$$

$$D = (1+\kappa)^2 - \frac{2m^2_\mu}{E_{\nu_\mu}E_{\nu_e}\left(1-\cos\theta\right)}, \tag{A.94}$$

$$\kappa = \frac{Q}{E_{\nu_\mu}E_{\nu_e}\left(1-\cos\theta\right)}; \tag{A.95}$$

J_i's are expressed in terms of the Fermi-Dirac integrals:

$$J_0 = \frac{T}{1-e^{\left(E_{\nu_e}+E_{\nu_\mu}+\mu_e-\mu_\mu\right)/T}}\left[G_0\left(\beta\epsilon_{\min}\right)-G_0\left(\beta\epsilon_{\max}\right)\right], \tag{A.96}$$

$$J_1 = \frac{T^2}{1-e^{\left(E_{\nu_e}+E_{\nu_\mu}+\mu_e-\mu_\mu\right)/T}}\left\{\left[G_1\left(\beta\epsilon_{\min}\right)+\beta\epsilon_{\min}G_0\left(\beta\epsilon_{\min}\right)\right]-\left[G_1\left(\beta\epsilon_{\max}\right)+\beta\epsilon_{\max}G_0\left(\beta\epsilon_{\max}\right)\right]\right\}, \tag{A.97}$$

$$J_2 = \frac{T^3}{1-e^{\left(E_{\nu_e}+E_{\nu_\mu}+\mu_e-\mu_\mu\right)/T}}\left\{\left[G_2\left(\beta\epsilon_{\min}\right)+2\beta\epsilon_{\min}G_1\left(\beta\epsilon_{\min}\right)+\left(\beta\epsilon_{\min}\right)^2G_0\left(\beta\epsilon_{\min}\right)\right]\right.$$
$$\left.-\left[G_2\left(\beta\epsilon_{\max}\right)+2\beta\epsilon_{\max}G_1\left(\beta\epsilon_{\max}\right)+\left(\beta\epsilon_{\max}\right)^2G_0\left(\beta\epsilon_{\max}\right)\right]\right\}, \tag{A.98}$$

$$\epsilon_{\min} = \max\left\{m_\mu,\epsilon_-\right\}, \tag{A.99}$$

$$\epsilon_{\max} = \min\left\{\epsilon_+,E_{\nu_e}+E_{\nu_\mu}-m_e\right\}, \tag{A.100}$$

$$\epsilon_\pm = \frac{E_{\nu_e}+E_{\nu_\mu}}{2}\left(\kappa+1\right)\pm\frac{\Delta}{2}\sqrt{\left(1+\kappa\right)^2-\frac{2m_\mu^2}{E_{\nu_e}E_{\nu_\mu}(1-\cos\theta)}} = \frac{E_{\nu_e}+E_{\nu_\mu}}{2}\left(\kappa+1\right)\pm\frac{\Delta}{2}\sqrt{D}, \tag{A.101}$$

and

$$G_i\left(\beta\epsilon\right) = F_i\left[\beta\left(E_{\nu_e}+E_{\nu_\mu}-\mu_e-\epsilon\right)\right]-F_i\left[\beta\left(\mu_\mu-\epsilon\right)\right]. \tag{A.102}$$

An appropriate limit to $\mu_\mu = E_{\nu_e}+E_{\nu_\mu}-\mu_e$ results in the following expressions of J_0 through J_2:

$$J_0 = T\left\{F_{-1}\left[\beta\left(\mu_\mu-\epsilon_{\min}\right)\right]-F_{-1}\left[\beta\left(\mu_\mu-\epsilon_{\max}\right)\right]\right\}, \tag{A.103}$$

$$J_1 = T^2\left(\left\{F_0\left[\beta\left(\mu_\mu-\epsilon_{\min}\right)\right]+\beta\epsilon_{\min}F_{-1}\left[\beta\left(\mu_\mu-\epsilon_{\min}\right)\right]\right\}\right.$$
$$\left.-\left\{F_0\left[\beta\left(\mu_\mu-\epsilon_{\max}\right)\right]+\beta\epsilon_{\max}F_{-1}\left[\beta\left(\mu_\mu-\epsilon_{\max}\right)\right]\right\}\right), \tag{A.104}$$

$$J_2 = T^3\left(\left\{2F_1\left[\beta\left(\mu_\mu-\epsilon_{\min}\right)\right]+2\beta\epsilon_{\min}F_0\left[\beta\left(\mu_\mu-\epsilon_{\min}\right)\right]+\left(\beta\epsilon_{\min}\right)^2F_{-1}\left[\beta\left(\mu_\mu-\epsilon_{\min}\right)\right]\right\}\right.$$
$$\left.-\left\{2F_1\left[\beta\left(\mu_\mu-\epsilon_{\max}\right)\right]+2\beta\epsilon_{\max}F_0\left[\beta\left(\mu_\mu-\epsilon_{\max}\right)\right]+\left(\beta\epsilon_{\max}\right)^2F_{-1}\left[\beta\left(\mu_\mu-\epsilon_{\max}\right)\right]\right\}\right). \tag{A.105}$$

Finally, the other kernel $R^{\text{in}}_{\nu_e}$ is obtained from the detailed balance, Eq. (3.42).

Appendix B

Nucleon structure function

I give here the detailed calculations of the structure function of nucleons, which, under the current approximation, are generally witten (Eq. (3.59)) as

$$\mathcal{S}^{\mu\nu}\left(q^0,q\right)=\iint\frac{d^3\boldsymbol{p}_2}{(2\pi)^3 2E_2^*}\frac{d^3\boldsymbol{p}_4}{(2\pi)^3 2E_4^*}f_2\left(E_2^*\right)\left[1-f_4\left(E_4^*\right)\right]\,\Lambda^{\mu\nu}\,(2\pi)^4\delta^{(4)}(p_1^\mu+p_2^\mu-p_3^\mu-p_4^\mu). \tag{B.1}$$

I follow the procedure given in Roberts and Reddy (2017a). First, I decompose the hadronic tensor, $\Lambda^{\mu\nu}$, as follows:

$$\Lambda^{\mu\nu}=AP_1^{\mu\nu}+BP_2^{\mu\nu}+CP_3^{\mu\nu}+DP_4^{\mu\nu}+EP_5^{\mu\nu}+FP_6^{\mu\nu}, \tag{B.2}$$

where $P_i^{\mu\nu}$ $(i=1,\ldots,6)$ are defined with the transferred 4 momentum transfer $q^\alpha=(q^0,0,0,q)$ and another vector $n^\alpha=(q,0,0,q^0)$, orthogonal to q^α;

$$P_1^{\mu\nu}=\eta^{\mu\nu}-\frac{1}{q_\alpha^2}q^\mu q^\nu-\frac{1}{n^2}n^\mu n^\nu, \tag{B.3}$$

$$P_2^{\mu\nu}=\frac{1}{q_\alpha^2}q^\mu q^\nu, \tag{B.4}$$

$$P_3^{\mu\nu}=\frac{1}{n^2}n^\mu n^\nu, \tag{B.5}$$

$$P_4^{\mu\nu}=\frac{1}{q_\alpha^2}\left(q^\mu n^\nu+q^\nu n^\mu\right), \tag{B.6}$$

$$P_5^{\mu\nu}=\frac{1}{q_\alpha^2}q_\alpha q_\beta\epsilon^{\mu\nu\alpha\beta}, \tag{B.7}$$

$$P_6^{\mu\nu}=\frac{1}{q_\alpha^2}\left(q^\mu n^\nu-q^\nu n^\mu\right), \tag{B.8}$$

where $q_\alpha^2=q_\alpha q^\alpha$, $n^2=n_\alpha n^\alpha$ and $\epsilon^{\mu\nu\alpha\beta}$ is the anti-symmetric tensor. These tensors are orthogonal to one another and satisfy the following relations:

$$P_{1\,\mu\nu}P_1^{\mu\nu}=2,\ P_{2\,\mu\nu}P_2^{\mu\nu}=1,\ P_{3\,\mu\nu}P_3^{\mu\nu}=1,\ P_{4\,\mu\nu}P_4^{\mu\nu}=-2,\ P_{5\,\mu\nu}P_5^{\mu\nu}=-2,\ P_{6\,\mu\nu}P_6^{\mu\nu}=2. \tag{B.9}$$

Then the coefficients in the decomposition (Eq. (B.2)) are given as follows:

$$A = 4m_2^* m_4^* \left(G_V^2 - G_A^2\right) - 4\left(G_V^2 + G_A^2\right)\frac{1}{q_\alpha^2}\left[(q\cdot\tilde{p}_2)(q\cdot\tilde{p}_4) - (n\cdot\tilde{p}_2)(n\cdot\tilde{p}_4)\right] + 4\frac{F_2 G_V}{M}\left[m_2^*(q\cdot\tilde{p}_4) - m_4^*(q\cdot\tilde{p}_2)\right] + \frac{F_2^2}{M^2}\left[-(n\cdot\tilde{p}_2)(n\cdot\tilde{p}_4) + m_2^* m_4^* q_\alpha^2\right], \tag{B.10}$$

$$B = 4m_2^* m_4^* \left(G_V^2 - G_A^2\right) + 4\left(G_V^2 + G_A^2\right)\frac{1}{q_\alpha^2}\left[2(q\cdot\tilde{p}_2)(q\cdot\tilde{p}_4) - q_\alpha^2(\tilde{p}_2\cdot\tilde{p}_4)\right] - 2\frac{F_2^2}{M^2}(q\cdot\tilde{p}_2)(q\cdot\tilde{p}_4) + 8\frac{G_A G_P}{M}\left[m_4^*(q\cdot\tilde{p}_2) - m_2^*(q\cdot\tilde{p}_4)\right] + 4\frac{G_P^2}{M^2}q_\alpha^2\left[(\tilde{p}_2\cdot\tilde{p}_4) - m_2^* m_4^*\right], \tag{B.11}$$

$$C = 4m_2^* m_4^* \left(G_V^2 - G_A^2\right) - 4\left(G_V^2 + G_A^2\right)\frac{1}{n^2}\left[(n\cdot\tilde{p}_2)(n\cdot\tilde{p}_4) - n^2(\tilde{p}_2\cdot\tilde{p}_4)\right] - 4\frac{F_2 G_V}{M}\left[m_4^*(q\cdot\tilde{p}_2) - m_2^*(q\cdot\tilde{p}_4)\right] + \frac{F_2^2}{M^2}\left[-n^2(\tilde{p}_2\cdot\tilde{p}_4) + 2(n\cdot\tilde{p}_2)(n\cdot\tilde{p}_4) - 2(q\cdot\tilde{p}_2)(q\cdot\tilde{p}_4) + m_2^* m_4^* q_\alpha^2\right], \tag{B.12}$$

$$D = -4\left(G_V^2 + G_A^2\right)\frac{1}{q_\alpha^2}\left[(q\cdot\tilde{p}_2)(n\cdot\tilde{p}_4) + (q\cdot\tilde{p}_4)(n\cdot\tilde{p}_2)\right] + 2\frac{F_2 G_V}{M}\left[m_2^*(n\cdot\tilde{p}_4) - m_4^*(n\cdot\tilde{p}_2)\right] + 4\frac{G_A G_P}{M}\left[m_2^*(n\cdot\tilde{p}_4) - m_4^*(n\cdot\tilde{p}_2)\right], \tag{B.13}$$

$$E = 8iG_V G_A\frac{1}{q_\alpha^2}\left[(q\cdot\tilde{p}_4)(n\cdot\tilde{p}_2) - (q\cdot\tilde{p}_2)(n\cdot\tilde{p}_4)\right] + 4i\frac{F_2 G_A}{M}\left[m_2^*(n\cdot\tilde{p}_4) + m_4^*(n\cdot\tilde{p}_2)\right], \tag{B.14}$$

$$F = -4iG_V G_A\frac{1}{q_\alpha^2}(q_\mu n_\nu - q_\nu n_\mu)\tilde{p}_{4\alpha}\tilde{p}_{2\beta}\epsilon^{\alpha\mu\beta\nu} - 2i\frac{F_2 G_P}{M^2}n_\mu\tilde{p}_{4\rho}\tilde{p}_{2\sigma}q_\beta\epsilon^{\rho\sigma\beta\mu}. \tag{B.15}$$

Now, the calculation of the structure function is reduced to integrations over $\boldsymbol{p}_2$ and $\boldsymbol{p}_4$ of the following 10 scalar variables:

$$1, (\tilde{p}_2\cdot\tilde{p}_4), (q\cdot\tilde{p}_2), (q\cdot\tilde{p}_4), (n\cdot\tilde{p}_2), (n\cdot\tilde{p}_4), (q\cdot\tilde{p}_2)(q\cdot\tilde{p}_4), (n\cdot\tilde{p}_2)(n\cdot\tilde{p}_4), (q\cdot\tilde{p}_2)(n\cdot\tilde{p}_4), (n\cdot\tilde{p}_2)(q\cdot\tilde{p}_4). \tag{B.16}$$

As an example, I show the calculation for 1:

$$\mathcal{I}_1(q^0, q) = \iint \frac{d^3\boldsymbol{p}_2}{(2\pi)^3 2E_2^*}\frac{d^3\boldsymbol{p}_4}{(2\pi)^3 2E_4^*} f_2(E_2^*)\left[1 - f_4(E_4^*)\right]\cdot 1\cdot(2\pi)^4\delta^{(4)}(p_1^\mu + p_2^\mu - p_3^\mu - p_4^\mu). \tag{B.17}$$

The integration over $\boldsymbol{p}_4$ is done with the delta function as

$$\mathcal{I}_1(q^0, q) = \frac{1}{16\pi^2}\iint\frac{d^3\boldsymbol{p}_2}{E_2^*}d^3\boldsymbol{p}_4\int\frac{dE_4^*}{E_4^*}\delta\left(E_4^* - \sqrt{|\boldsymbol{p}_4|^2 + m_4^{*2}}\right) f_2(E_2^*)\left[1 - f_4(E_4^*)\right]\cdot 1\cdot\delta^{(4)}(p_1^\mu + p_2^\mu - p_3^\mu - p_4^\mu) \tag{B.18}$$

$$= \frac{1}{8\pi^2}\int p_2\, dE_2^*\, d\cos\alpha\, d\beta f_2(E_2^*)\left(1 - f_4(E_4^*)\right)\cdot 1\cdot\delta\left(\tilde{p}_4^2 - m_4^{*2}\right)\Theta(E_4^* - m_4^*), \tag{B.19}$$

where I used the following relations, $\frac{1}{E_4^*}\delta\left(E_4^* - \sqrt{|\boldsymbol{p}_4|^2 + m_4^{*2}}\right) = \delta\left(\tilde{p}_4^2 - m_4^{*2}\right)$, $p_2 dp_2 = E_2^* dE_2^*$, and α and β are the zenith and azimuth angles of $\boldsymbol{p}_2$, respectively, with $\boldsymbol{q}$ being the z-axis;

I also note

$$E_4^* = E_2^* + U_2 - U_4 + q^0 =: E_2^* + \tilde{q}^0, \tag{B.20}$$

$$\boldsymbol{p}_4 = \boldsymbol{p}_2 + \boldsymbol{q}, \tag{B.21}$$

and

$$\delta\left(\tilde{p}_4^2 - m_4^{*2}\right) = \frac{1}{|2qp_2|}\delta\left(\cos\alpha - \cos\alpha_0\right), \tag{B.22}$$

$$\cos\alpha_0 = \frac{\left(\tilde{q}^0\right)^2 + 2\tilde{q}^0 E_2^* - q^2 + m_2^{*2} - m_4^{*2}}{2qp_2}. \tag{B.23}$$

The integrations over β and $\cos\alpha$ can be done to give

$$\mathcal{I}_1\left(q^0, q\right) = \frac{1}{8\pi|q|}\int_{E_{\min}}^{E_{\max}} dE_2^* f_2\left(E_2^*\right)\left[1 - f_4\left(E_4^*\right)\right], \tag{B.24}$$

where $E_{\min}$ and $E_{\max}$ are given as

$$\begin{cases} E_{\min} = \max\left\{m_2^*, m_4^* - \tilde{q}^0, E_{2,+}^*\right\}, E_{\max} = \infty & \left(\Delta^2 := \left(\tilde{q}^0\right)^2 - q^2 < 0\right) \\ E_{\min} = \max\left\{m_2^*, m_4^* - \tilde{q}^0, E_{2,-}^*\right\}, E_{\max} = E_{2,+}^* & \left(\Delta^2 > 0 \text{ and } \Delta^2 < (m_2^{*2} - m_4^{*2}) \text{ or } \Delta^2 > (m_2^{*2} + m_4^{*2})\right) \end{cases} \tag{B.25}$$

with

$$E_{2,\pm}^* = -\frac{\tilde{q}^0}{2}\kappa \pm \frac{|q|}{2}\sqrt{\kappa^2 - \frac{4m_2^{*2}}{\Delta^2}},\ \kappa = 1 + \frac{m_2^{*2} - m_4^{*2}}{\Delta^2}; \tag{B.26}$$

otherwise $E_{2,\pm}^*$ has no real solutions for $(m_2^{*2} - m_4^{*2}) < \Delta^2 < (m_2^{*2} + m_4^{*2})$ and $\mathcal{I}_1 = 0$.

The remaining integration (B.24) can be written with the Fermi-Dirac integral, which can be easily evaluated numerically, in the following way:

$$\mathcal{I}_1\left(q^0, q\right) = \frac{1}{8\pi|q|}J_0, \tag{B.27}$$

where J_0 as well as J_1 and J_2, which will be needed later, are expressed as

$$J_0 = \frac{T}{1 - \exp\left[\beta\left(-\tilde{q}^0 - \mu_2 + \mu_4\right)\right]}\left[G_0\left(\beta E_{\min}\right) - G_0\left(\beta E_{\max}\right)\right], \tag{B.28}$$

$$J_1 = \frac{T^2}{1 - \exp\left[\beta\left(-\tilde{q}^0 - \mu_2 + \mu_4\right)\right]}\left\{\left[G_1\left(\beta E_{\min}\right) + \beta E_{\min} G_0\left(\beta E_{\min}\right)\right] - \left[G_1\left(\beta E_{\max}\right) + \beta E_{\max} G_0\left(\beta E_{\max}\right)\right]\right\}, \tag{B.29}$$

$$J_2 = \frac{T^3}{1 - \exp\left[\beta\left(-\tilde{q}^0 - \mu_2 + \mu_4\right)\right]}\left\{\left[G_2\left(\beta E_{\min}\right) + 2\beta E_{\min} G_1\left(\beta E_{\min}\right) + \left(\beta E_{\min}\right)^2 G_0\left(\beta E_{\min}\right)\right] - \left[G_2\left(\beta E_{\max}\right) + 2\beta E_{\max} G_1\left(\beta E_{\max}\right) + \left(\beta E_{\max}\right)^2 G_0\left(\beta E_{\max}\right)\right]\right\}, \tag{B.30}$$

with

$$G_i\left(\beta E\right) = F_i\left[\beta\left(\mu_2 - E\right)\right] - F_i\left[\beta\left(\mu_4 - \tilde{q}^0 - E\right)\right]. \tag{B.31}$$

Taking appropriate limits, we obtain for $\tilde{q}^0 = \mu_4 - \mu_2$

$$J_0 = T\left\{F_{-1}\left[\beta\left(\mu_2 - E_{\min}\right)\right] - F_{-1}\left[\beta\left(\mu_2 - E_{\max}\right)\right]\right\}, \tag{B.32}$$

$$\begin{aligned} J_1 = T^2\Big(&\left\{F_0\left[\beta\left(\mu_2 - E_{\min}\right)\right] + \beta E_{\min} F_{-1}\left[\beta\left(\mu_2 - E_{\min}\right)\right]\right\} \\ &- \left\{F_0\left[\beta\left(\mu_2 - E_{\max}\right)\right] + \beta E_{\max} F_{-1}\left[\beta\left(\mu_2 - E_{\max}\right)\right]\right\}\Big), \end{aligned} \tag{B.33}$$

$$\begin{aligned} J_2 = T^3\Big(&\left\{2F_1\left[\beta\left(\mu_2 - E_{\min}\right)\right] + 2\beta E_{\min} F_0\left[\beta\left(\mu_2 - E_{\min}\right)\right] + \left(\beta E_{\min}\right)^2 F_{-1}\left[\beta\left(\mu_2 - E_{\min}\right)\right]\right\} \\ &- \left\{2F_1\left[\beta\left(\mu_2 - E_{\max}\right)\right] + 2\beta E_{\max} F_0\left[\beta\left(\mu_2 - E_{\max}\right)\right] + \left(\beta E_{\max}\right)^2 F_{-1}\left[\beta\left(\mu_2 - E_{\max}\right)\right]\right\}\Big). \end{aligned} \tag{B.34}$$

In a similar way, other integrals for the remaining 9 scalars in Eq. (B.16) can be accomplished to get the followings:

$$\mathcal{I}_{(\tilde{p}_2\cdot\tilde{p}_4)}\left(q^0, q\right) = \frac{1}{8\pi|q|}\left[m_2^{*2} - \frac{1}{2}\left(\Delta^2 + m_2^{*2} - m_4^{*2}\right)\right] J_0, \tag{B.35}$$

$$\mathcal{I}_{(q\cdot\tilde{p}_2)}\left(q^0, q\right) = \frac{1}{8\pi|q|}\left(b_{(q\cdot\tilde{p}_2)} J_1 + c_{(q\cdot\tilde{p}_2)} J_0\right), \tag{B.36}$$

$$b_{(q\cdot\tilde{p}_2)} = U_4 - U_2 =: \Delta U, \tag{B.37}$$

$$c_{(q\cdot\tilde{p}_2)} = -\frac{1}{2}\left(\Delta^2 + m_2^{*2} - m_4^{*2}\right), \tag{B.38}$$

$$\mathcal{I}_{(q\cdot\tilde{p}_4)}\left(q^0, q\right) = \frac{1}{8\pi|q|}\left(b_{(q\cdot\tilde{p}_4)} J_1 + c_{(q\cdot\tilde{p}_4)} J_0\right), \tag{B.39}$$

$$b_{(q\cdot\tilde{p}_4)} = \Delta U, \tag{B.40}$$

$$c_{(q\cdot\tilde{p}_4)} = -\frac{1}{2}\left(\Delta^2 + m_2^{*2} - m_4^{*2}\right) + q^0\tilde{q}^0 - q^2, \tag{B.41}$$

$$\mathcal{I}_{(n\cdot\tilde{p}_2)}\left(q^0, q\right) = \frac{1}{8\pi|q|}\left(b_{(n\cdot\tilde{p}_2)} J_1 + c_{(n\cdot\tilde{p}_2)} J_0\right), \tag{B.42}$$

$$b_{(n\cdot\tilde{p}_2)} = q - \frac{q^0\tilde{q}^0}{q}, \tag{B.43}$$

$$c_{(n\cdot\tilde{p}_2)} = -\frac{q^0}{2q}\left(\Delta^2 + m_2^{*2} - m_4^{*2}\right), \tag{B.44}$$

$$\mathcal{I}_{(n\cdot\tilde{p}_4)}\left(q^0, q\right) = \frac{1}{8\pi|q|}\left(b_{(n\cdot\tilde{p}_4)} J_1 + c_{(n\cdot\tilde{p}_4)} J_0\right), \tag{B.45}$$

$$b_{(n\cdot\tilde{p}_4)} = q - \frac{q^0\tilde{q}^0}{q}, \tag{B.46}$$

$$c_{(n\cdot\tilde{p}_4)} = -\frac{q^0}{2q}\left(\Delta^2 + m_2^{*2} - m_4^{*2}\right) + q\left(\tilde{q}^0 - q^0\right), \tag{B.47}$$

$$\mathcal{I}_{(q\cdot\tilde{p}_2)(q\cdot\tilde{p}_4)}\left(q^0, q\right) = \frac{1}{8\pi|q|}\left(a_{(q\cdot\tilde{p}_2)(q\cdot\tilde{p}_4)} J_2 + b_{(q\cdot\tilde{p}_2)(q\cdot\tilde{p}_4)} J_1 + c_{(q\cdot\tilde{p}_2)(q\cdot\tilde{p}_4)} J_0\right), \tag{B.48}$$

$$a_{(q\cdot\tilde{p}_2)(q\cdot\tilde{p}_4)} = (\Delta U)^2, \tag{B.49}$$

$$b_{(q\cdot\tilde{p}_2)(q\cdot\tilde{p}_4)} = \Delta U\left[\left(q^0\tilde{q}^0 - q^2\right) - \left(\Delta^2 + m_2^{*2} - m_4^{*2}\right)\right], \tag{B.50}$$

$$c_{(q\cdot\tilde{p}_2)(q\cdot\tilde{p}_4)} = \frac{1}{4}\left(\Delta^2 + m_2^{*2} - m_4^{*2}\right)^2 - \frac{1}{2}\left(\Delta^2 + m_2^{*2} - m_4^{*2}\right)\left(q^0\tilde{q}^0 - q^2\right), \tag{B.51}$$

$$\mathcal{I}_{(n\cdot\tilde{p}_2)(n\cdot\tilde{p}_4)}\left(q^0,q\right)=\frac{1}{8\pi|q|}\left(a_{(n\cdot\tilde{p}_2)(n\cdot\tilde{p}_4)}J_2+b_{(n\cdot\tilde{p}_2)(n\cdot\tilde{p}_4)}J_1+c_{(n\cdot\tilde{p}_2)(n\cdot\tilde{p}_4)}J_0\right), \tag{B.52}$$

$$a_{(n\cdot\tilde{p}_2)(n\cdot\tilde{p}_4)}=\left(q-\frac{q^0\tilde{q}^0}{q}\right)^2, \tag{B.53}$$

$$b_{(n\cdot\tilde{p}_2)(n\cdot\tilde{p}_4)}=q\left(\tilde{q}^0-q^0\right)\left(q-\frac{q^0\tilde{q}^0}{q}\right)-\frac{q^0}{q}\left(\Delta^2+m_2^{*2}-m_4^{*2}\right)\left(q-\frac{q^0\tilde{q}^0}{q}\right), \tag{B.54}$$

$$c_{(n\cdot\tilde{p}_2)(n\cdot\tilde{p}_4)}=\frac{1}{4}\left(\frac{q^0}{q}\right)^2\left(\Delta^2+m_2^{*2}-m_4^{*2}\right)^2-\frac{1}{2}q^0\left(\tilde{q}^0-q^0\right)\left(\Delta^2+m_2^{*2}-m_4^{*2}\right), \tag{B.55}$$

$$\mathcal{I}_{(q\cdot\tilde{p}_2)(n\cdot\tilde{p}_4)}\left(q^0,q\right)=\frac{1}{8\pi|q|}\left(a_{(q\cdot\tilde{p}_2)(n\cdot\tilde{p}_4)}J_2+b_{(q\cdot\tilde{p}_2)(n\cdot\tilde{p}_4)}J_1+c_{(q\cdot\tilde{p}_2)(n\cdot\tilde{p}_4)}J_0\right), \tag{B.56}$$

$$a_{(q\cdot\tilde{p}_2)(n\cdot\tilde{p}_4)}=\Delta U\left(q-\frac{q^0\tilde{q}^0}{q}\right), \tag{B.57}$$

$$b_{(q\cdot\tilde{p}_2)(n\cdot\tilde{p}_4)}=-\frac{1}{2}\left(\Delta^2+m_2^{*2}-m_4^{*2}\right)\left(q-\frac{q^0\tilde{q}^0}{q}\right)+\Delta U\left[-\frac{q^0}{2q}\left(\Delta^2+m_2^{*2}-m_4^{*2}\right)+q\left(\tilde{q}^0-q^0\right)\right], \tag{B.58}$$

$$c_{(q\cdot\tilde{p}_2)(n\cdot\tilde{p}_4)}=-\frac{1}{2}\left(\Delta^2+m_2^{*2}-m_4^{*2}\right)\left[-\frac{q^0}{2q}\left(\Delta^2+m_2^{*2}-m_4^{*2}\right)+q\left(\tilde{q}^0-q^0\right)\right], \tag{B.59}$$

$$\mathcal{I}_{(n\cdot\tilde{p}_2)(q\cdot\tilde{p}_4)}\left(q^0,q\right)=\frac{1}{8\pi|q|}\left(a_{(n\cdot\tilde{p}_2)(q\cdot\tilde{p}_4)}J_2+b_{(n\cdot\tilde{p}_2)(q\cdot\tilde{p}_4)}J_1+c_{(n\cdot\tilde{p}_2)(q\cdot\tilde{p}_4)}J_0\right), \tag{B.60}$$

$$a_{(n\cdot\tilde{p}_2)(q\cdot\tilde{p}_4)}=\Delta U\left(q-\frac{q^0\tilde{q}^0}{q}\right), \tag{B.61}$$

$$b_{(n\cdot\tilde{p}_2)(q\cdot\tilde{p}_4)}=-\frac{q^0}{2q}\left(\Delta^2+m_2^{*2}-m_4^{*2}\right)\Delta U+\left(q-\frac{q^0\tilde{q}^0}{q}\right)\left[-\frac{1}{2}\left(\Delta^2+m_2^{*2}-m_4^{*2}\right)+q^0\tilde{q}^0-q^2\right], \tag{B.62}$$

$$c_{(n\cdot\tilde{p}_2)(q\cdot\tilde{p}_4)}=-\frac{q^0}{2q}\left(\Delta^2+m_2^{*2}-m_4^{*2}\right)\left[-\frac{1}{2}\left(\Delta^2+m_2^{*2}-m_4^{*2}\right)+q^0\tilde{q}^0-q^2\right]. \tag{B.63}$$

The structure function is obtained in the following form:

$$\mathcal{S}^{\mu\nu}\left(q^0,q\right)=\bar{A}P_1^{\mu\nu}+\bar{B}P_2^{\mu\nu}+\bar{C}P_3^{\mu\nu}+\bar{D}P_4^{\mu\nu}+\bar{E}P_5^{\mu\nu}, \tag{B.64}$$

where the coefficients are written as

$$\bar{X}=\iint\frac{d^3\boldsymbol{p}_2}{(2\pi)^3 2E_2^*}\frac{d^3\boldsymbol{p}_4}{(2\pi)^3 2E_4^*}f_2\left(E_2^*\right)\left[1-f_4\left(E_4^*\right)\right]X\left(2\pi\right)^4\delta^{(4)}(p_1^\mu+p_2^\mu-p_3^\mu-p_4^\mu)\quad(X=A,B,C,D,E), \tag{B.65}$$

and are actually some linear combinations of $\mathcal{I}_i$ with $i=1,\left(\tilde{p}_2\cdot\tilde{p}_4\right),\ldots,\left(n\cdot\tilde{p}_2\right)\left(q\cdot\tilde{p}_4\right)$. Note that the case with $X=F$ (see Eq. (B.15)) is omitted because it vanishes as a result

of energy momentum conservation,

$$\begin{aligned} q_\mu n_\nu \tilde{p}_{2\alpha} \tilde{p}_{4\beta} \epsilon^{\mu\nu\alpha\beta} &= q_\mu n_\nu \tilde{p}_{2\alpha} \left(\tilde{p}_{2\beta} + q_\beta + U_\beta\right) \epsilon^{\mu\nu\alpha\beta} \\ &= (U_2 - U_4) q_\mu n_\nu \tilde{p}_{2\alpha} \epsilon^{\mu\nu\alpha 0} \qquad \left(U^\beta = (U_2 - U_4, 0, 0, 0)\right) \\ &= \Delta U q_i n_j \tilde{p}_{2k} \epsilon^{ijk} \\ &= 0. \qquad \left(\because \boldsymbol{q} = (0, 0, q), \boldsymbol{n} = (0, 0, q^0)\right) \end{aligned} \tag{B.66}$$

Finally the contraction of the projection tensors with the lepton tensor yields the following results:

$$L_{\mu\nu} P_1^{\mu\nu} = -16 \left[\frac{1}{q_\alpha^2} \left(p_1 \cdot q\right) \left(p_3 \cdot q\right) + \frac{1}{n^2} \left(p_1 \cdot n\right) \left(p_3 \cdot n\right) \right], \tag{B.67}$$

$$L_{\mu\nu} P_2^{\mu\nu} = 8 \left[\frac{2}{q_\alpha^2} \left(p_1 \cdot q\right) \left(p_3 \cdot q\right) - \left(p_1 \cdot p_3\right) \right], \tag{B.68}$$

$$L_{\mu\nu} P_3^{\mu\nu} = 8 \left[\frac{2}{n^2} \left(p_1 \cdot n\right) \left(p_3 \cdot n\right) - \left(p_1 \cdot p_3\right) \right], \tag{B.69}$$

$$L_{\mu\nu} P_4^{\mu\nu} = \frac{16}{q_\alpha^2} \left[\left(p_1 \cdot q\right) \left(p_3 \cdot n\right) + \left(p_1 \cdot n\right) \left(p_3 \cdot q\right) \right], \tag{B.70}$$

$$L_{\mu\nu} P_5^{\mu\nu} = \pm i \frac{16}{q_\alpha^2} \left[\left(p_1 \cdot n\right) \left(p_3 \cdot q\right) - \left(p_1 \cdot q\right) \left(p_3 \cdot n\right) \right]. \quad (+ : \text{neutrino}, - : \text{antineutrino}). \tag{B.71}$$

Acknowledgments

This study was accomplished thanks to a lot of supports of many people. I would like to express my gratitude.

First of all, I am grateful to my supervisor Prof. Shoichi Yamada for great support. He gave me a lot of valuable advises based on his deep insights when I got stuck in my research. The daily discussion was very exciting and I learned not only physics but also the attitude toward research and the fun of research.

I would also like to thank all my collaborators. I want to thank Kazuya Takahashi for his supports. The code of linear analysis used in chapter 2 is based on the code developed by him. I was able to improve the code and the research thanks to the discussion with him. I am also thank Ko Nakamura for providing the numerical data of CCSN simulation. The analysis of LESA could not be carried out without his help.

I greatly appreciate Shun Furusawa and Kohsuke Sumiyoshi for making the EoS including muon used in chapter 3. I also appreciate Ken'ichiro Nakazato and Hideyuki Suzuki for providing the numerical code of PNS cooling and teaching how to use and improve it. Discussions with them are always informative and helped to advance my research.

I would appreciate all members of Yamada labratory. Daily discussions and conversations with them have always inspired and encouraged me to continue my research.

Finally, I thank all my family and friends for supporting me in my daily life.

Bibliography

J Aasi et al. Advanced LIGO. *Class. Quantum Gravity*, 32(7):074001, apr 2015. ISSN 0264-9381. doi: 10.1088/0264-9381/32/7/074001. URL https://iopscience.iop.org/article/10.1088/0264-9381/32/7/074001.

R. Abbasi et al. IceCube sensitivity for low-energy neutrinos from nearby supernovae. *Astron. Astrophys.*, 535:1–17, 2011. ISSN 14320746. doi: 10.1051/0004-6361/201117810.

B P Abbott et al. Observation of Gravitational Waves from a Binary Black Hole Merger. *Phys. Rev. Lett.*, 116(6):061102, 2016. ISSN 1079-7114. doi: 10.1103/PhysRevLett.116.061102. URL http://www.ncbi.nlm.nih.gov/pubmed/26918975.

B. P. Abbott et al. GW170817: Observation of Gravitational Waves from a Binary Neutron Star Inspiral. *Phys. Rev. Lett.*, 119(16):30–33, 2017. ISSN 10797114. doi: 10.1103/PhysRevLett.119.161101.

K. Abe et al. Real-time supernova neutrino burst monitor at Super-Kamiokande. *Astropart. Phys.*, 81:39–48, aug 2016. ISSN 09276505. doi: 10.1016/j.astropartphys.2016.04.003. URL https://linkinghub.elsevier.com/retrieve/pii/S0927650516300457.

K. Abe et al. Hyper-kamiokande design report, 2018.

B. Abi et al. Deep underground neutrino experiment (dune), far detector technical design report, volume ii: Dune physics, 2020.

F Acernese et al. Advanced Virgo: a second-generation interferometric gravitational wave detector. *Class. Quantum Gravity*, 32(2):024001, jan 2015. ISSN 0264-9381. doi: 10.1088/0264-9381/32/2/024001. URL https://iopscience.iop.org/article/10.1088/0264-9381/32/2/024001.

M.A. Acero, P. Adamson, G. Agam, L. Aliaga, T. Alion, V. Allakhverdian, N. Anfimov, A. Antoshkin, E. Arrieta-Diaz, L. Asquith, and et al. Supernova neutrino detection in nova. *Journal of Cosmology and Astroparticle Physics*, 2020(10):014–014, Oct 2020. ISSN 1475-7516. doi: 10.1088/1475-7516/2020/10/014. URL http://dx.doi.org/10.1088/1475-7516/2020/10/014.

T Akutsu et al. Overview of KAGRA: Detector design and construction history. *Prog. Theor. Exp. Phys.*, 2021(5), may 2021. ISSN 2050-3911. doi: 10.1093/ptep/ptaa125. URL https://academic.oup.com/ptep/article/doi/10.1093/ptep/ptaa125/5893487.

E.N. Alexeyev, L.N. Alexeyeva, I.V. Krivosheina, and V.I. Volchenko. Detection of the neutrino signal from SN 1987A in the LMC using the INR Baksan underground

scintillation telescope. *Phys. Lett. B*, 205(2-3):209–214, apr 1988. ISSN 03702693. doi: 10.1016/0370-2693(88)91651-6. URL https://doi.org/10.1016/0370-2693(88)91651-6https://linkinghub.elsevier.com/retrieve/pii/0370269388916516.

Fengpeng An et al. Neutrino physics with JUNO. *J. Phys. G Nucl. Part. Phys.*, 43(3), 2016. ISSN 13616471. doi: 10.1088/0954-3899/43/3/030401.

Josep M. Aparicio. A Simple and Accurate Method for the Calculation of Generalized Fermi Functions. *Astrophys. J. Suppl. Ser.*, 117(2):627–632, aug 1998. ISSN 0067-0049. doi: 10.1086/313121. URL https://iopscience.iop.org/article/10.1086/313121.

H. A. Bethe. Supernova mechanisms. *Rev. Mod. Phys.*, 62(4):801–866, oct 1990. ISSN 0034-6861. doi: 10.1103/RevModPhys.62.801. URL https://link.aps.org/doi/10.1103/RevModPhys.62.801.

H. A. Bethe and J. R. Wilson. Revival of a stalled supernova shock by neutrino heating. *Astrophys. J.*, 295(2):14, aug 1985. ISSN 0004-637X. doi: 10.1086/163343. URL http://adsabs.harvard.edu/doi/10.1086/163343.

R. M. Bionta, G. Blewitt, C. B. Bratton, D. Casper, A. Ciocio, R. Claus, B. Cortez, M. Crouch, S. T. Dye, S. Errede, G. W. Foster, W. Gajewski, K. S. Ganezer, M. Goldhaber, T. J. Haines, T. W. Jones, D. Kielczewska, W. R. Kropp, J. G. Learned, J. M. LoSecco, J. Matthews, R. Miller, M. S. Mudan, H. S. Park, L. R. Price, F. Reines, J. Schultz, S. Seidel, E. Shumard, D. Sinclair, H. W. Sobel, J. L. Stone, L. R. Sulak, R. Svoboda, G. Thornton, J. C. Van Der Velde, and C. Wuest. Observation of a neutrino burst in coincidence with supernova 1987A in the large magellanic cloud. *Phys. Rev. Lett.*, 58(14):1494–1496, 1987. ISSN 00319007. doi: 10.1103/PhysRevLett.58.1494.

John M. Blondin and Anthony Mezzacappa. The Spherical Accretion Shock Instability in the Linear Regime. *Astrophys. J.*, 642(1):401–409, 2006. ISSN 0004-637X. doi: 10.1086/500817.

John M. Blondin, Anthony Mezzacappa, and Christine DeMarino. Stability of Standing Accretion Shocks, with an Eye toward Core - Collapse Supernovae. *Astrophys. J.*, 584 (2):971–980, 2003. ISSN 0004-637X. doi: 10.1086/345812.

R Bollig, H.-T Janka, A Lohs, G Martínez-Pinedo, C. J. Horowitz, and T Melson. Muon Creation in Supernova Matter Facilitates Neutrino-Driven Explosions. *Phys. Rev. Lett.*, 119(24):242702, dec 2017. ISSN 0031-9007. doi: 10.1103/PhysRevLett.119.242702. URL https://journals.aps.org/prl/pdf/10.1103/PhysRevLett.119.242702https://link.aps.org/doi/10.1103/PhysRevLett.119.242702.

S. W. Bruenn. Stellar core collapse - Numerical model and infall epoch. *Astrophys. J. Suppl. Ser.*, 58:771, 1985. ISSN 0067-0049. doi: 10.1086/191056. URL http://adsabs.harvard.edu/doi/10.1086/191056.

A. Burrows, E. Livne, L. Dessart, C. D. Ott, and J. Murphy. A New Mechanism for Core - Collapse Supernova Explosions. *Astrophys. J.*, 640(2):878–890, 2006. ISSN 0004-637X. doi: 10.1086/500174.

A. Burrows, E. Livne, L. Dessart, C. D. Ott, and J. Murphy. Features of the Acoustic Mechanism of Core - Collapse Supernova Explosions. *Astrophys. J.*, 655(1):416–433, 2007a. ISSN 0004-637X. doi: 10.1086/509773. URL http://arxiv.org/abs/0709.3876.

Adam Burrows. Colloquium: Perspectives on core-collapse supernova theory. *Rev. Mod. Phys.*, 85(1):245–261, 2013. ISSN 00346861. doi: 10.1103/RevModPhys.85.245.

Adam Burrows and James M Lattimer. The birth of neutron stars. *Astrophys. J.*, 307: 178, aug 1986. ISSN 0004-637X. doi: 10.1086/164405. URL http://adsabs.harvard.edu/doi/10.1086/164405.

Adam Burrows and R. F. Sawyer. Effects of correlations on neutrino opacities in nuclear matter. *Phys. Rev. C - Nucl. Phys.*, 58(1):554–571, 1998. ISSN 1089490X. doi: 10.1103/PhysRevC.58.554.

Adam Burrows, Luc Dessart, Christian D. Ott, and Eli Livne. Multi-dimensional explorations in supernova theory. *Phys. Rep.*, 442(1-6):23–37, 2007b. ISSN 03701573. doi: 10.1016/j.physrep.2007.02.001.

Giovanni Camelio, Alessandro Lovato, Leonardo Gualtieri, Omar Benhar, José A Pons, and Valeria Ferrari. Evolution of a proto-neutron star with a nuclear many-body equation of state: Neutrino luminosity and gravitational wave frequencies. *Phys. Rev. D*, 96(4):043015, aug 2017. ISSN 2470-0010. doi: 10.1103/PhysRevD.96.043015. URL https://arxiv.org/pdf/1704.01923.pdfhttps://link.aps.org/doi/10.1103/PhysRevD.96.043015.

Sean M. Couch and Christian D. Ott. The role of turbulence in neutrino-driven core-collapse supernova explosions. *Astrophys. J.*, 799(1), 2015. ISSN 15384357. doi: 10.1088/0004-637X/799/1/5.

Carolyn L. Doherty, Pilar Gil-Pons, Lionel Siess, and John C. Lattanzio. Super-AGB Stars and their Role as Electron Capture Supernova Progenitors. *Publ. Astron. Soc. Aust.*, 34(2017), 2017. ISSN 1323-3580. doi: 10.1017/pasa.2017.52.

Joshua C. Dolence, Adam Burrows, and Weiqun Zhang. Two-Dimensional core-collapse supernova models with multi-dimensional transport. *Astrophys. J. Lett.*, 800(1), 2015. ISSN 20418213. doi: 10.1088/0004-637X/800/1/10.

F. Douchin and P. Haensel. A unified equation of state of dense matter and neutron star structure. *Astron. Astrophys.*, 380(1):151–167, nov 2001. ISSN 00046361. doi: 10.1051/0004-6361:20011402. URL http://arxiv.org/abs/astro-ph/0111092http://dx.doi.org/10.1051/0004-6361:20011402.

Rodrigo Fernández. Three-dimensional simulations of SASI-and convection-dominated core-collapse supernovae. *Mon. Not. R. Astron. Soc.*, 452(2):2071–2086, 2015. ISSN 13652966. doi: 10.1093/mnras/stv1463.

T Fischer, S C Whitehouse, A Mezzacappa, F.-K Thielemann, and M Liebendörfer. Protoneutron star evolution and the neutrino-driven wind in general relativistic neutrino radiation hydrodynamics simulations. *Astron. Astrophys.*, 517:A80, jul 2010. ISSN 0004-6361. doi: 10.1051/0004-6361/200913106. URL https://www.aanda.org/articles/aa/pdf/2010/09/aa13106-09.pdfhttp://www.aanda.org/10.1051/0004-6361/200913106.

Tobias Fischer, Gang Guo, Gabriel Martínez-Pinedo, Matthias Liebendörfer, and Anthony Mezzacappa. Muonization of supernova matter. *Phys. Rev. D*, 102(12):123001, dec 2020. ISSN 2470-0010. doi: 10.1103/PhysRevD.102.123001. URL https://link.aps.org/doi/10.1103/PhysRevD.102.123001.

T. Foglizzo. A simple toy model of the advective-acoustic instability. I. Perturbative approach. *Astrophys. J.*, 694(2):820–832, 2009. ISSN 15384357. doi: 10.1088/0004-637X/694/2/820.

T. Foglizzo, L. Scheck, and H. - Th. Janka. Neutrino - driven Convection versus Advection in Core - Collapse Supernovae. *Astrophys. J.*, 652(2):1436–1450, 2006. ISSN 0004-637X. doi: 10.1086/508443.

Bryce Fore and Sanjay Reddy. Pions in hot dense matter and their astrophysical implications. *Phys. Rev. C*, 101(3):035809, mar 2020. ISSN 2469-9985. doi: 10.1103/PhysRevC.101.035809. URL http://arxiv.org/abs/1911.02632https://link.aps.org/doi/10.1103/PhysRevC.101.035809.

Shun Furusawa, Kohsuke Sumiyoshi, Shoichi Yamada, and Hideyuki Suzuki. New equations of state based on the liquid drop model of heavy nuclei and quantum approach to light nuclei for core-collapse supernova simulations. *Astrophys. J.*, 772(2), 2013. ISSN 15384357. doi: 10.1088/0004-637X/772/2/95.

Robert Glas, H. Thomas Janka, Tobias Melson, Georg Stockinger, and Oliver Just. Effects of LESA in Three-Dimensional Supernova Simulations with Multi-Dimensional and Ray-by-Ray-plus Neutrino Transport. (1), sep 2018. URL http://arxiv.org/abs/1809.10150.

Jérôme Guilet and Thierry Foglizzo. On the linear growth mechanism driving the standing accretion shock instability. *Mon. Not. R. Astron. Soc.*, 421(1):546–560, 2012. ISSN 00358711. doi: 10.1111/j.1365-2966.2012.20333.x.

Gang Guo, Gabriel Martínez-Pinedo, Andreas Lohs, and Tobias Fischer. Charged-current muonic reactions in core-collapse supernovae. *Phys. Rev. D*, 102(2):023037, jul 2020. ISSN 2470-0010. doi: 10.1103/PhysRevD.102.023037. URL http://arxiv.org/abs/2006.12051http://dx.doi.org/10.1103/PhysRevD.102.023037https://link.aps.org/doi/10.1103/PhysRevD.102.023037.

Florian Hanke, Bernhard Müller, Annop Wongwathanarat, Andreas Marek, and Hans Thomas Janka. Sasi activity in three-dimensional neutrino-hydrodynamics simulations of supernova cores. *Astrophys. J.*, 770(1), 2013. ISSN 15384357. doi: 10.1088/0004-637X/770/1/66.

A. Harada, H. Nagakura, W. Iwakami, and S. Yamada. A Parametric Study of the Acoustic Mechanism for Core-collapse Supernovae. *Astrophys. J.*, 839(1):28, 2017. doi: 10.3847/1538-4357/aa6896. URL http://arxiv.org/abs/1704.02984{%}0Ahttp://dx.doi.org/10.3847/1538-4357/aa6896.

M. Hempel, T. Fischer, J. Schaffner-Bielich, and M. Liebendörfer. NEW EQUATIONS OF STATE IN SIMULATIONS OF CORE-COLLAPSE SUPERNOVAE. *Astrophys. J.*, 748(1):70, mar 2012. ISSN 0004-637X. doi: 10.1088/0004-637X/748/1/70. URL https://iopscience.iop.org/article/10.1088/0004-637X/748/1/70.

Marc Herant, Willy Benz, W. Raphael Hix, Chris L. Fryer, and Stirling A. Colgate. Inside the supernova: A powerful convective engine. *Astrophys. J.*, 435:339, nov 1994. ISSN 0004-637X. doi: 10.1086/174817. URL http://adsabs.harvard.edu/doi/10.1086/174817.

K. Hirata, T. Kajita, M. Koshiba, M. Nakahata, Y. Oyama, N. Sato, A. Suzuki, M. Takita, Y. Totsuka, T. Kifune, T. Suda, K. Takahashi, T. Tanimori, K. Miyano, M. Yamada, E. W. Beier, L. R. Feldscher, S. B. Kim, A. K. Mann, F. M. Newcomer, R. Van, W. Zhang, and B. G. Cortez. Observation of a neutrino burst from the supernova SN1987A. *Phys. Rev. Lett.*, 58(14):1490–1493, apr 1987. ISSN 0031-9007. doi: 10.1103/PhysRevLett.58.1490. URL `https://link.aps.org/doi/10.1103/PhysRevLett.58.1490`.

C. J. Horowitz. Weak magnetism for antineutrinos in supernovae. *Phys. Rev. D - Part. Fields, Gravit. Cosmol.*, 65(4):12, 2002. ISSN 15502368. doi: 10.1103/PhysRevD.65.043001.

C.J. Horowitz and Gang Li. The mu and tau number of supernovae. *Phys. Lett. B*, 443(1-4):58–62, dec 1998. ISSN 03702693. doi: 10.1016/S0370-2693(98)01293-3. URL `https://linkinghub.elsevier.com/retrieve/pii/S0370269398012933`.

L. Hüdepohl, B. Müller, H. T. Janka, A. Marek, and G. G. Raffelt. Neutrino signal of electron-capture supernovae from core collapse to cooling. *Phys. Rev. Lett.*, 104(25):1–4, 2010. ISSN 10797114. doi: 10.1103/PhysRevLett.104.251101.

Wakana Iwakami, Hiroki Nagakura, and Shoichi Yamada. Parametric study of flow patterns behind the standing accretion shock wave for core-collapse supernovae. *Astrophys. J.*, 786(2), 2014. ISSN 15384357. doi: 10.1088/0004-637X/786/2/118.

Hans-Thomas Janka. Explosion Mechanisms of COre-Collapse Supernovae. *Annu. Rev. Nucl. Part. Sci.*, 62(1):407–451, 2012. doi: 10.1146/annurev-nucl-102711-094901.

Hans-Thomas Janka, Tobias Melson, and Alexander Summa. Physics of Core-Collapse Supernovae in Three Dimensions: A Sneak Preview. *Annu. Rev. Nucl. Part. Sci.*, 66(1):341–375, oct 2016. ISSN 0163-8998. doi: 10.1146/annurev-nucl-102115-044747. URL `http://arxiv.org/abs/1603.03905http://arxiv.org/abs/1602.05576http://dx.doi.org/10.1146/annurev-nucl-102115-044747http://www.annualreviews.org/doi/10.1146/annurev-nucl-102115-044747`.

Hajime Kawahara, Takami Kuroda, Tomoya Takiwaki, Kazuhiro Hayama, and Kei Kotake. A Linear and Quadratic Time-Frequency Analysis of Gravitational Waves from Core-Collapse Supernovae. *Astrophys. J.*, 867(2):126, nov 2018. ISSN 1538-4357. doi: 10.3847/1538-4357/aae57b. URL `http://arxiv.org/abs/1810.00334`.

Wolfgang Keil, H.-Thomas Janka, and Georg Raffelt. Reduced neutrino opacities and the SN 1987A signal. *Phys. Rev. D*, 51(12):6635–6646, jun 1995. ISSN 0556-2821. doi: 10.1103/PhysRevD.51.6635. URL `https://link.aps.org/doi/10.1103/PhysRevD.51.6635`.

F. S. Kitaura, H. Th Janka, and W. Hillebrandt. Explosions of O-Ne-Mg cores, the Crab supernova and subluminous type II-P supernovae. *Astron. Astrophys.*, 450(1):345–350, 2006. ISSN 00046361. doi: 10.1051/0004-6361:20054703.

Dong Lai and Peter Goldreich. Growth of Perturbations in Gravitational Collapse and Accretion. *Astrophys. J.*, 535(1):402–411, 2000. ISSN 0004-637X. doi: 10.1086/308821.

Tina J Leitner. Neutrino interactions with nucleons and nuclei. *Dipl. Justus-Liebig-Universität Gießen*, 2005.

A. Marek and H. Th Janka. Delayed neutrino-driven supernova explosions aided by the standing accretion-shock instability. *Astrophys. J.*, 694(1):664–696, 2009. ISSN 15384357. doi: 10.1088/0004-637X/694/1/664.

G. Martínez-Pinedo, T. Fischer, A. Lohs, and L. Huther. Charged-current weak interaction processes in hot and dense matter and its impact on the spectra of neutrinos emitted from protoneutron star cooling. *Phys. Rev. Lett.*, 109(25):1–5, 2012. ISSN 00319007. doi: 10.1103/PhysRevLett.109.251104.

Anthony Mezzacappa and Stephen W. Bruenn. Stellar core collapse - A Boltzmann treatment of neutrino-electron scattering. *Astrophys. J.*, 410:740, jun 1993. ISSN 0004-637X. doi: 10.1086/172791. URL `http://adsabs.harvard.edu/doi/10.1086/172791`.

B Müller. Neutrino Emission as Diagnostics of Core-Collapse Supernovae. *Annu. Rev. Nucl. Part. Sci.*, 69(1):253–278, oct 2019. ISSN 0163-8998. doi: 10.1146/annurev-nucl-101918-023434. URL `www.annualreviews.orghttp://arxiv.org/abs/1904.11067http://dx.doi.org/10.1146/annurev-nucl-101918-023434https://www.annualreviews.org/doi/10.1146/annurev-nucl-101918-023434`.

Bernhard Müller. Hydrodynamics of core-collapse supernovae and their progenitors. *Living Rev. Comput. Astrophys.*, 6(1):3, dec 2020. ISSN 2367-3621. doi: 10.1007/s41115-020-0008-5. URL `https://link.springer.com/10.1007/s41115-020-0008-5`.

Jeremiah W. Murphy, Joshua C. Dolence, and Adam Burrows. The dominance of neutrino-driven convection in core-collapse supernovae. *Astrophys. J.*, 771(1), 2013. ISSN 15384357. doi: 10.1088/0004-637X/771/1/52.

Hiroki Nagakura, Wakana Iwakami, Shun Furusawa, Hirotada Okawa, Akira Harada, Kohsuke Sumiyoshi, Shoichi Yamada, Hideo Matsufuru, and Akira Imakura. Simulations of Core-collapse Supernovae in Spatial Axisymmetry with Full Boltzmann Neutrino Transport. *Astrophys. J.*, 854(2):136, 2018. ISSN 1538-4357. doi: 10.3847/1538-4357/aaac29. URL `http://dx.doi.org/10.3847/1538-4357/aaac29`.

Ken'ichiro Nakazato and Hideyuki Suzuki. Cooling Timescale for Protoneutron Stars and Properties of Nuclear Matter: Effective Mass and Symmetry Energy at High Densities. *Astrophys. J.*, 878(1):25, jun 2019. ISSN 1538-4357. doi: 10.3847/1538-4357/ab1d4b. URL `http://dx.doi.org/10.3847/1538-4357/ab1d4bhttps://iopscience.iop.org/article/10.3847/1538-4357/ab1d4b`.

Kenichiro Nakazato and Hideyuki Suzuki. A New Approach to the Mass and Radius of Neutron Stars with Supernova Neutrinos. *Astrophys. J.*, 891(2):156, mar 2020. ISSN 1538-4357. doi: 10.3847/1538-4357/ab7456. URL `https://iopscience.iop.org/article/10.3847/1538-4357/ab7456`.

Ken'Ichiro Nakazato, Kohsuke Sumiyoshi, Hideyuki Suzuki, Tomonori Totani, Hideyuki Umeda, and Shoichi Yamada. Supernova neutrino light curves and spectra for various progenitor stars: From core collapse to proto-neutron star cooling. *Astrophys. Journal, Suppl. Ser.*, 205(1), 2013. ISSN 00670049. doi: 10.1088/0067-0049/205/1/2.

Ken'Ichiro Nakazato, Hideyuki Suzuki, and Hajime Togashi. Heavy nuclei as thermal insulation for protoneutron stars. *Phys. Rev. C*, 97(3):1–6, 2018. ISSN 24699993. doi: 10.1103/PhysRevC.97.035804.

Micaela Oertel, Aurélien Pascal, Marco Mancini, and Jérôme Novak. Improved neutrino-nucleon interactions in dense and hot matter for numerical simulations. *Phys. Rev. C*, 102(3):035802, sep 2020. ISSN 2469-9985. doi: 10.1103/PhysRevC.102.035802. URL http://arxiv.org/abs/2003.02152http://dx.doi.org/10.1103/PhysRevC.102.035802https://link.aps.org/doi/10.1103/PhysRevC.102.035802.

Naofumi Ohnishi, Kei Kotake, and Shoichi Yamada. Numerical Analysis of Standing Accretion Shock Instability with Neutrino Heating in Supernova Cores. *Astrophys. J.*, 641(2):1018–1028, 2006. ISSN 0004-637X. doi: 10.1086/500554.

Michael E. Peskin. *An Introduction To Quantum Field Theory*. CRC Press, may 2018. ISBN 9780429972102. doi: 10.1201/9780429503559. URL https://www.taylorfrancis.com/books/9780429972102.

J. A. Pons, S. Reddy, M. Prakash, J. M. Lattimer, and J. A. Miralles. Evolution of Proto–Neutron Stars. *Astrophys. J.*, 513(2):780–804, mar 1999. ISSN 0004-637X. doi: 10.1086/306889. URL https://www.worldscientific.com/doi/abs/10.1142/S0218271810017913https://iopscience.iop.org/article/10.1086/306889.

Jade Powell and Bernhard Müller. Gravitational wave emission from 3D explosion models of core-collapse supernovae with low and normal explosion energies. *Mon. Not. R. Astron. Soc.*, 487(1):1178–1190, jul 2019. ISSN 0035-8711. doi: 10.1093/mnras/stz1304. URL http://arxiv.org/abs/1812.05738https://academic.oup.com/mnras/article/487/1/1178/5489198.

Georg G. Raffelt. Mu - and Tau - Neutrino Spectra Formation in Supernovae. *Astrophys. J.*, 561(2):890–914, 2001. ISSN 0004-637X. doi: 10.1086/323379.

Sanjay Reddy, Madappa Prakash, James M. Lattimer, and Jose A. Pons. Effects of strong and electromagnetic correlations on neutrino interactions in dense matter. *Phys. Rev. C*, 59(5):2888–2918, may 1999. ISSN 0556-2813. doi: 10.1103/PhysRevC.59.2888. URL https://link.aps.org/doi/10.1103/PhysRevC.59.2888.

L. F. Roberts. A NEW CODE FOR PROTO-NEUTRON STAR EVOLUTION. *Astrophys. J.*, 755(2):126, aug 2012. ISSN 0004-637X. doi: 10.1088/0004-637X/755/2/126. URL https://iopscience.iop.org/article/10.1088/0004-637X/755/2/126.

Luke F. Roberts and Sanjay Reddy. Charged current neutrino interactions in hot and dense matter. *Phys. Rev. C*, 95(4):1–20, 2017a. ISSN 24699993. doi: 10.1103/PhysRevC.95.045807.

Luke F. Roberts and Sanjay Reddy. Neutrino Signatures from Young Neutron Stars. In *Handb. Supernovae*, pages 1605–1635. Springer International Publishing, Cham, dec 2017b. doi: 10.1007/978-3-319-21846-5_5. URL http://arxiv.org/abs/1612.03860http://dx.doi.org/10.1007/978-3-319-21846-5{_}5http://link.springer.com/10.1007/978-3-319-21846-5{_}5.

R. F. Sawyer. Reduction of Weak Interaction Rates in the Supernova Core. *Phys. Rev. Lett.*, 75(12):2260–2263, sep 1995. ISSN 0031-9007. doi: 10.1103/PhysRevLett.75.2260. URL https://link.aps.org/doi/10.1103/PhysRevLett.75.2260.

L. Scheck, K. Kifonidis, H.-Th. Janka, and E. Müller. Multidimensional supernova simulations with approximative neutrino transport. *Astron. Astrophys.*, 457(3):963–986, oct 2006. ISSN 0004-6361. doi: 10.1051/0004-6361:20064855. URL http://www.aanda.org/10.1051/0004-6361:20064855.

Kate Scholberg. Supernova neutrino detection. *Annu. Rev. Nucl. Part. Sci.*, 62:81–103, 2012. ISSN 01638998. doi: 10.1146/annurev-nucl-102711-095006.

H. Shen. Complete relativistic equation of state for neutron stars. *Phys. Rev. C*, 65(3): 035802, feb 2002. ISSN 0556-2813. doi: 10.1103/PhysRevC.65.035802. URL https://link.aps.org/doi/10.1103/PhysRevC.65.035802.

H. Shen, H. Toki, K. Oyamatsu, and K. Sumiyoshi. Relativistic equation of state for core-collapse supernova simulations. *Astrophys. Journal, Suppl. Ser.*, 197(2), 2011. ISSN 00670049. doi: 10.1088/0067-0049/197/2/20.

K. Sumiyoshi, H. Suzuki, and H. Toki. Influence of the symmetry energy on the birth of neutron stars and supernova neutrinos. *Astron. Astrophys. -Berlin-*, 303(2):475–475, 1995. ISSN 0004-6361.

K Sumiyoshi, S Yamada, H Suzuki, H Shen, S Chiba, and H Toki. Postbounce Evolution of Core - Collapse Supernovae: Long - Term Effects of the Equation of State. *Astrophys. J.*, 629(2):922–932, aug 2005. ISSN 0004-637X. doi: 10.1086/431788. URL https://arxiv.org/pdf/astro-ph/0506620.pdfhttps://iopscience.iop.org/article/10.1086/431788.

Yudai Suwa, Kohsuke Sumiyoshi, Ken'ichiro Nakazato, Yasufumi Takahira, Yusuke Koshio, Masamitsu Mori, and Roger A. Wendell. Observing Supernova Neutrino Light Curves with Super-Kamiokande: Expected Event Number over 10 s. *Astrophys. J.*, 881(2):139, aug 2019. ISSN 1538-4357. doi: 10.3847/1538-4357/ab2e05. URL http://arxiv.org/abs/1904.09996http://dx.doi.org/10.3847/1538-4357/ab2e05https://iopscience.iop.org/article/10.3847/1538-4357/ab2e05.

Hideyuki Suzuki. Supernova Neutrinos. In M. Fukugita and A. Suzuki, editors, *Phys. Astrophys. Neutrinos*, pages 763–847. Springer Japan, Tokyo, 1994. doi: 10.1007/978-4-431-67029-2_12. URL http://link.springer.com/10.1007/978-4-431-67029-2{_}12.

Kazuya Takahashi, Wakana Iwakami, Yu Yamamoto, and Shoichi Yamada. LINKS BETWEEN THE SHOCK INSTABILITY IN CORE-COLLAPSE SUPERNOVAE. *Astrophys. J.*, 831(1):1–30, 2016. ISSN 1538-4357. doi: 10.3847/0004-637X/831/1/75. URL http://dx.doi.org/10.3847/0004-637X/831/1/75.

Tomoya Takiwaki and Kei Kotake. Anisotropic emission of neutrino and gravitational-wave signals from rapidly rotating core-collapse supernovae. *Mon. Not. R. Astron. Soc. Lett.*, 475(1):L91–L95, mar 2018. ISSN 1745-3925. doi: 10.1093/mnrasl/sly008. URL https://academic.oup.com/mnrasl/article/475/1/L91/4803948.

Irene Tamborra, Florian Hanke, Hans Thomas Janka, Bernhard Müller, Georg G. Raffelt, and Andreas Marek. Self-sustained asymmetry of lepton-number emission: A new phenomenon during the supernova shock-accretion phase in three dimensions. *Astrophys. J.*, 792(2), 2014a. ISSN 15384357. doi: 10.1088/0004-637X/792/2/96.

Irene Tamborra, Georg Raffelt, Florian Hanke, Hans Thomas Janka, and Bernhard Müller. Neutrino emission characteristics and detection opportunities based on three-dimensional supernova simulations. *Phys. Rev. D - Part. Fields, Gravit. Cosmol.*, 90 (4):1–18, 2014b. ISSN 15502368. doi: 10.1103/PhysRevD.90.045032.

The LIGO Scientific Collaboration, the Virgo Collaboration, B. P. Abbott, et al. GW190425: Observation of a Compact Binary Coalescence with Total Mass - 3.4 M. jan 2020. URL http://arxiv.org/abs/2001.01761.

S. E. Woosley and Thomas A. Weaver. The Evolution and Explosion of Massive Stars. II. Explosive Hydrodynamics and Nucleosynthesis. *Astrophys. J. Suppl. Ser.*, 101(8):181, nov 1995. ISSN 0067-0049. doi: 10.1086/192237. URL http://adsabs.harvard.edu/doi/10.1086/192237.

Shoichi Yamada and Hiroshi Toki. Neutrino-nucleon reaction rates in the supernova core in the relativistic random phase approximation. *Phys. Rev. C*, 61(1):015803, dec 1999. ISSN 0556-2813. doi: 10.1103/PhysRevC.61.015803. URL https://journals.aps.org/prc/abstract/10.1103/PhysRevC.61.015803https://link.aps.org/doi/10.1103/PhysRevC.61.015803.

T. Yamasaki and S. Yamada. Stability of the accretion flows with stalled shocks in core-collapse supernovae. *AIP Conf. Proc.*, 937:344–348, 2007. ISSN 0094243X. doi: 10.1063/1.2803589.

Shijun Yoshida, Naofumi Ohnishi, and Shoichi Yamada. EXCITATION OF g -MODES IN A PROTO Y NEUTRON STAR BY THE STANDING. *Astrophys. J.*, pages 1268–1276, 2007.

W. R. Yueh and J. R. Buchler. Neutrino transport in supernova models - S[SUB]N[/SUB] method. *Astrophys. J.*, 217:565, oct 1977. ISSN 0004-637X. doi: 10.1086/155605. URL http://adsabs.harvard.edu/doi/10.1086/155605.

William R. Yueh and J. Robert Buchler. Neutrino processes in dense matter. *Astrophys. Space Sci.*, 41(1):221–251, may 1976. ISSN 0004-640X. doi: 10.1007/BF00684583. URL http://link.springer.com/10.1007/BF00684583.

Nai-Bo Zhang and Bao-An Li. Constraints on the Muon Fraction and Density Profile in Neutron Stars. *Astrophys. J.*, 893(1):61, 2020. ISSN 1538-4357. doi: 10.3847/1538-4357/ab7dbc. URL http://dx.doi.org/10.3847/1538-4357/ab7dbc.

List of research achievements for application of Doctor of Science, Waseda University

Full Name： 杉浦　健一　seal or signature

Date Submitted(yyyy/mm/dd): 2022/9/12

種類別 (By Type)	題名、 発表・発行掲載誌名、 発表・発行年月、 連名者（申請者含む） (theme, journal name, date & year of publication, name of authors inc. yourself)
Academic papers	◯Title: Muon-related neutrino interactions and their relevance for proto-neutron star cooling Journal: Progress of Theoretical and Experimental Physics Publication date: September 2022 Authors: Ken'ichi Sugiura, Shun Furusawa, Kohsuke Sumiyoshi, Shoichi Yamada ◯ Title: Linear Analysis of the Shock Instability in Core-collapse Supernovae: Influences of Acoustic Power and Fluctuations of Neutrino Luminosity Journal: The Astrophysical Journal, Volume 874, Number 1, Page 28 Publication date: March 2019 Authors: Ken'ichi Sugiura, Kazuya Takahashi, Shoichi Yamada
Lectures	Title: 原始中性子星におけるミューオンとそのニュートリノシグナルへの影響 Conference: 日本天文学会　2021年春季年会 Place: オンライン，Date: 2021年3月 Authors: 杉浦健一, 山田章一，古澤峻，中里健一郎，鈴木英之，住吉光介 Title: 超新星爆発におけるミューオン生成とニュートリノシグナルへの影響 Conference: 第7回超新星ニュートリノ 研究会 Place: オンライン, Date: 2021年1月 Authors: 杉浦健一，山田章一，古澤峻，中里健一郎，鈴木英之 Title: Muon creation in proto-neutron stars and its implication for neutrino signal in cooling phase Conference: The Evolution of Massive Stars and Formation of Compact Stars: from the Cradle to the Grave Place: Tokyo Japan，Date: Fenruary 2020 Authors: Ken'ichi Sugiura, Hideyuki Suzuki, Ken'ichiro Nakazato, Shoichi Yamada Title: Corrections of charged current neutrino reaction rates and its effects on PNS cooling Conference: Multi-dimensional Modeling and Multi-Messenger observation from Core-Collapse Supernovae Place: Fukuoka, Japan，Date: October 2020 Authors: Ken'ichi Sugiura, Ken'ichiro Nakazato, Shoichi Yamada

List of research achievements for application of Doctor of Science, Waseda University

Full Name： 杉浦　健一　seal or signature

Date Submitted(yyyy/mm/dd): 2022/9/12

種類別 (By Type)	題名、 発表・発行掲載誌名、 発表・発行年月、 連名者（申請者含む） (theme, journal name, date & year of publication, name of authors inc. yourself)
	Title: 原始中性子星冷却におけるニュートリノシグナルへのweak-magnetismの影響 Conference: 日本天文学会 2019年秋季年会 Place: 熊本， Date: 2019年9月 Authors: 杉浦健一，中里健一郎，山田章一 Title: Linear Analysis of Shock Instability in CCSNe ~ Effects of Acoustic Injection and LESA~ Conference: FOE19 Fifty-one Erg Place: Raleigh, North Carolina, USA， Date: May 2019 Authors: Ken'ichi Sugiura, Kazuya Takahashi, Shoichi Yamada Title: Linear Analysisi of Shock Instability in Core-collapse Supernovae: Effects of fluctuations from inside Conference: RIKEN - RESCEU Joint Seminar 2019 Place: Tokyo Japan， Date: March 2019 Authors: Ken'ichi Sugiura, Kazuya Takahashi, Shoichi Yamada Title: Linear Analysis of Shock Dynamics in CCSNe ~Effects of Acoustic Injection and LESA~ Conference: 第31回理論懇シンポジウム Place: 京都， Date: 2018年12月 Authors: Ken'ichi Sugiura, Kazuya Takahashi, Shoichi Yamada Title: Linear Analysis of Shock Dynamics in CCSNe ~Effects of Acoustic Injection and LESA~ Conference: Deciphering multi-Dimensional nature of core-collapse SuperNovae via Gravitational-Wave and neutrino signatures (SNeGWv2018) Place: 富山， Date: 2018年12月 Authors: Ken'ichi Sugiura, Kazuya Takahashi, Shoichi Yamada Title: 原始中性子星におけるニュートリノシグナル Conference: 第48回天文・天体物理若手夏の学校 Place: 愛知， Date: 2018年7月 Authors: 杉浦健一，高橋和也，山田章一

List of research achievements for application of Doctor of Science, Waseda University

Full Name： 杉浦　健一　seal or signature

Date Submitted(yyyy/mm/dd): 2022/9/12

種類別 (By Type)	題名、 発表・発行掲載誌名、 発表・発行年月、 連名者（申請者含む） (theme, journal name, date & year of publication, name of authors inc. yourself)
	Title: Linear Analysis of Shock Dynamics in CCSNe ~Effects of Acoustic Injection and LESA~ Conference: Physics of Core-Collapse Supernovae and Compact Star Formations Place: Tokyo, Japan， Date: March 2018 Authors: Ken'ichi Sugiura, Kazuya Takahashi, Shoichi Yamada Title: 超新星コアにおける流体力学的不安定星の線形解析 Conference: 第47回天文・天体物理若手夏の学校 Place: 長野， Date: 2017年7月 Authors: 杉浦健一，高橋和也，山田章一